ABSTRACT

Title of dissertation: OPTICAL WIRELESS COMMUNICATION FOR MOBILE PLATFORMS

Thomas Shen, Doctor of Philosophy, 2016

Dissertation directed by: Professor Christopher C. Davis
Department of Electrical and Computer Engineering

The past few decades have witnessed the widespread adaptation of wireless devices such as cellular phones and Wifi-connected laptops, and demand for wireless communication is expected to continue to increase. Though radio frequency (RF) communication has traditionally dominated in this application space, recent decades have seen an increasing interest in the use of optical wireless (OW) communication to supplement RF communications. In contrast to RF communication technology, OW systems offer the use of largely unregulated electromagnetic spectrum and large bandwidths for communication. They also offer the potential to be highly secure against jamming and eavesdropping. Interest in OW has become especially keen in light of the maturation of light-emitting diode (LED) technology. This maturation, and the consequent emerging ubiquity of LED technology in lighting systems, has motivated the exploration of LEDs for wireless communication purposes in a wide variety of applications. Recent interest in this field has largely focused on the potential for indoor local area networks (LANs) to be realized with increasingly

common LED-based lighting systems. We envision the use of LED-based OW to serve as a supplement to RF technology in communication between mobile platforms, which may include automobiles, robots, or unmanned aerial vehicles (UAVs). OW technology may be especially useful in what are known as RF-denied environments, in which RF communication may be prohibited or undesirable.

The use of OW in these settings presents major challenges. In contrast to many RF systems, OW systems that operate at ranges beyond a few meters typically require relatively precise alignment. For example, some laser-based optical wireless communication systems require alignment precision to within small fractions of a degree. This level of alignment precision can be difficult to maintain between mobile platforms. Additionally, the use of OW systems in outdoor settings presents the challenge of interference from ambient light, which can be much brighter than any LED transmitter.

This thesis addresses these challenges to the use of LED-based communication between mobile platforms. We propose and analyze a dual-link LED-based system that uses one link with a wide transmission beam and relaxed alignment constraints to support a more narrow, precisely aligned, higher-data-rate link. The use of an optical link with relaxed alignment constraints to support the alignment of a more precisely aligned link motivates our exploration of a panoramic imaging receiver for estimating the range and bearing of neighboring nodes. The precision of such a system is analyzed and an experimental system is realized. Finally, we present an experimental prototype of a self-aligning LED-based link.

OPTICAL WIRELESS COMMUNICATION FOR MOBILE PLATFORMS

by

Thomas C. Shen

Dissertation submitted to the Faculty of the Graduate School of the
University of Maryland, College Park in partial fulfillment
of the requirements for the degree of
Doctor of Philosophy
2016

Advisory Committee:
Professor Christopher Davis, Chair/Advisor
Professor Thomas Murphy, Co-Advisor
Professor Julius Goldhar
Dr. Robert Drost
Professor Douglas Currie, Dean's Representative

Publications

Journal Papers

- Thomas C. Shen, Robert J. Drost, Brian M. Sadler , John R. Rzasa, and Christopher C. Davis, "Omnidirectional Beacon-Localization Using a Catadioptric System," Optics Express, 24(7), 6931(2016).

- Thomas C. Shen, Robert J. Drost, Christopher C. Davis, and Brian M. Sadler, "Design of dual-link (wide-and narrow-beam) LED communication systems," Optics Express, 22(9), 11107(2014).

- Hyochul Kim, Thomas C. Shen, Kaushik Roy-Choudhury, Glenn S. Solomon, and Edo Waks, "Resonant interactions between a mollow triplet sideband and a strongly coupled cavity," Physical Review Letters, 113(2), 027403(2014).

- Hyochul Kim, Ranojoy Bose, Thomas C. Shen, Glenn S. Solomon, and Edo Waks, "A quantum logic gate between a solid-state quantum bit and a photon," Nature Photonics, 7(5), 373(2013).

- Hyochul Kim, Thomas C. Shen, Deepak Sridharan, Glenn S. Solomon, and Edo Waks, "Magnetic field tuning of a quantum dot strongly coupled to a photonic crystal cavity," Applied Physics Letters, 98(9), 091102(2011).

- Hyochul Kim, Deepak Sridharan, Thomas C. Shen, Glenn S. Solomon, and Edo Waks, "Strong coupling between two quantum dots and a photonic crystal cavity using magnetic field tuning," Optics Express, 19(3), 2589(2011).

- Thomas C. Shen, Yong-Sung Kim, James A. Bur, Shawn-Yu Lin, "Optical Characterization of Bending Efficiency in On-Chip Hollow-Core Bragg Waveguides at λ=1.5 μm," IEEE Journal of Lightwave Technology, 28 (11), 1714-1719(2010).

- Mei-ling Kuo, Ya-Ju Lee, Thomas C. Shen, Shawn-Yu Lin, "Large enhancement of light-extraction efficiency from optically pumped, nanorod light-emitting diodes," Optics Letters, 34 (13), 2078-2080(2009).

Conference Papers

- Thomas C. Shen, Robert J. Drost, John Rzasa, Brian M. Sadler, and Christopher C. Davis, "Panoramic alignment system for optical wireless communication systems," Free-Space Laser Communication and Atmospheric Propagation XXVII, Proc. SPIE, 93540M(2015).

- Hyochul Kim, Thomas C. Shen, Deepak Sridharan, Glenn Solomon, and Edo Waks, "Selective coupling of quantum dot exciton spin states to a photonic crystal cavity using magnetic field tuning," International Semiconductor Device Research Symposium 2011.

- Hyochul Kim, Thomas C. Shen, Deepak Sridharan, Glenn Solomon, and Edo Waks, "Strong interaction between quantum dot exciton spin states and a photonic crystal cavity," Quantum Electronics and Laser Science Conference 2011.

- Edo Waks, Deepak Sridharan, Ranojoy Bose, Hyochul Kim, Thomas Shen, Glenn Solomon, "Nonlinear optics near the single photon level with quantum dots coupled to photonic crystals," SPIE NanoScience+ Engineering 2011.

Dedication

To my family – they have given me so much. To my mother – I hope she would feel proud.

Acknowledgments

I owe a great deal to all of the people who have helped make this dissertation a reality, and feel a need to bring attention to their generous assistance. I certainly could not have done this alone.

I am very grateful to my advisor, Professor Christopher Davis. Professor Davis provided me with a great opportunity to study an interesting topic that I hope will make a real and practical impact. This work would not have been possible without his assistance and guidance. I am lucky to have to had such a positive, knowledgeable, and encouraging influence.

I am very grateful to Dr. Brian Sadler and Dr. Robert Drost, who have helped to mentor me through this process. They have very generously lent their time and energy at every stage of my development as a researcher, and interacting with them has made me a stronger, more confident researcher. I am lucky to have had these two mentors to learn from throughout this growth process.

I would also like to recognize the help and support I've received from my labmates, Jonathan Ko, Chensheng Wu, William Nelson, and Dr. John Rzasa. John has been especially generous with his considerable expertise in electronics and optical experiments.

There is a need to recognize my family as well. They have provided invaluable moral support, a steadying influence in times of difficulty, and the firm foundation needed to pursue the challenges of research. Though my mother will not be there for graduation, I hope that this accomplishment would make her proud.

I would like to acknowledge financial support from the Army Research Office (ARO), for all the projects discussed herein.

Table of Contents

Chapter 1: Introduction

1.1 Motivation and Challenges of OW

The past few decades have witnessed the widespread adaptation of wireless devices such as cellular phones and Wifi-connected laptops, and demand for wireless communication is expected to further expand significantly as interest in robot-to-robot and vehicle-to-vehicle communication increases. To date, these wireless connections have typically utilized radio frequency (RF) technology. Though the robust and versatile capabilities of RF likely ensure that it will continue to play a significant role in this application space, increasingly there is interest in the use of wireless optical communications to supplement RF capabilities.

The maturation of LED technology and its growing ubiquity as a means of efficient illumination has generated much interest in exploiting LEDs for optical wireless communication (sometimes referred to as "Lifi"). Many envision using LEDs for communication in indoor local area networks (see Figure 1.1) [1–3], in airplane cabins, [4] (see Figure 1.2), in space [5], through signboards [6], between cars [7–9] (see Figure 1.3), in intelligent transportation systems [10, 11] and between robots [12, 13]. In many of these applications, LEDs are preferred to laser diodes (LDs), despite LDs' typically higher modulation bandwidths [14]. LEDs tend to

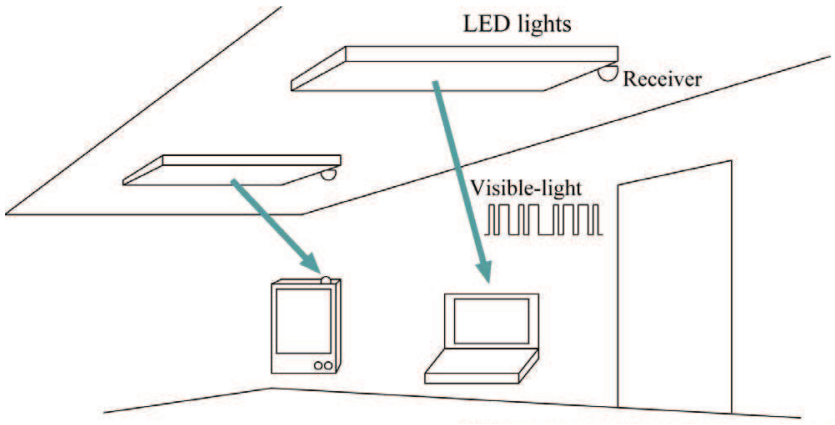

Figure 1.1: Illustration of OW technology indoors, from [1]. As LEDs are widely expected to eventually provide more indoor lighting, there is much interest in the exploitation of such devices for dual purposes; that is, use of LEDs for both illumination and communication.

have lower cost, higher reliability, may be used for illumination purposes, require less implementation complexity, and their larger emission areas allow for relaxed eye safety consideration and larger transmission powers [4, 7, 15].

Whether implemented using LDs or LEDs, OW technology is viewed as a potential supplement to RF technology due to advantages that include:

- OW technology utilizes a broad range of spectrum that is unregulated and unlicensed [14, 16, 17]. In contrast, traditional RF-based systems often face spectrum crowding and restrictions. The spectrum utilized by OW is practically unlimited in bandwidth and can support very high data rates [17]. For instance, air-to-ground optical links with data rates of 80 Gb/s have been demonstrated [18]. Access to this unrestricted spectrum could be especially important in military applications, as military demands for network capacity

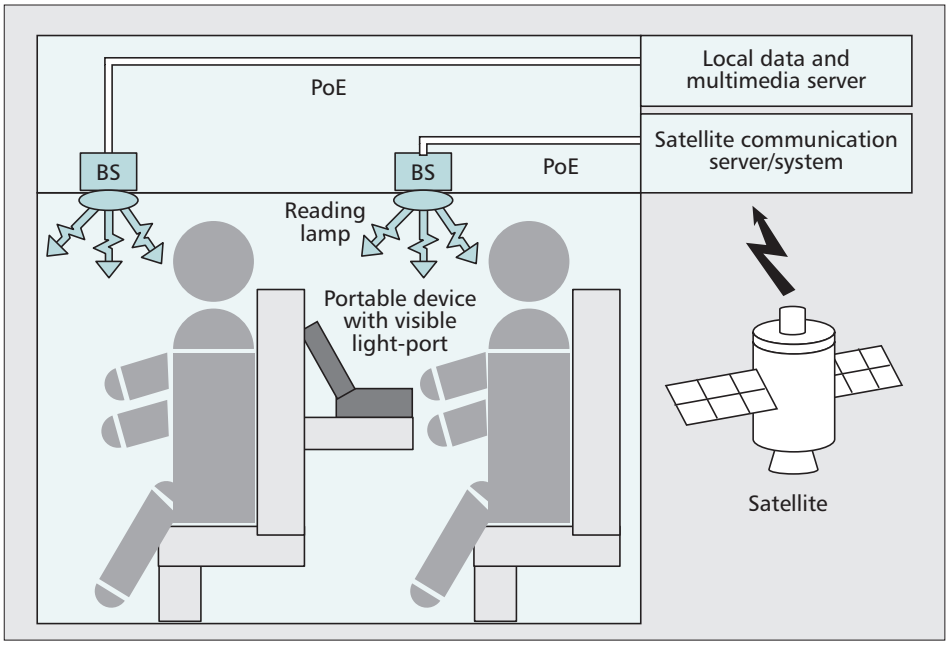

Figure 1.2: Illustration of OW technology in airplane cabin, [4]. This is one of many potential application spaces in which LEDs could be used for both illumination and communication.

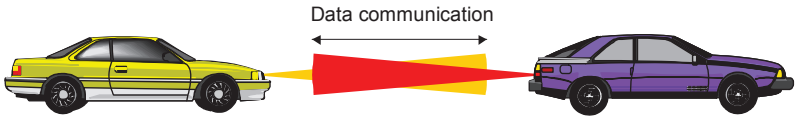

Figure 1.3: Car-to-car communication through LED-based headlights and tail lights, from [7].

are increasing, while spectrum available to it is decreasing [19].

- Communication at optical wavelengths can provide enhanced security from eavesdropping. In indoor settings, transmitted light cannot penetrate walls, making eavesdropping on a transmitter in a neighboring room very difficult [14]. In contrast, RF can often penetrate walls and other optically opaque obstacles. Outdoors, transmitted OW beams are often directional, utilizing beamwidths that can be small fractions of a degree. This spatial confinement enhances security by requiring any third party to place a receiver within the transmitted beam path in order to eavesdrop [19]. In contrast, achieving similar beamwidths in the RF spectrum would be impractical as it would require inordinately large antennas, due to the larger wavelength of RF frequencies [20].

- Unlike some RF devices, OW generally does not generate electromagnetic interference (EMI) that affects nearby sensitive electronic devices. And, OW systems can be virtually immune to crowding and interference from other users, including the jamming that often plagues RF communication in adversarial environments [19]. Due to this freedom from issues that arise from EMI, OW technology may be especially useful as an alternative means of communication in "RF-denied" environments, that is, environments in which RF communication may be prohibited or difficult due to EMI concerns. This may include some tactical military environments that suffer from enemy jamming, or healthcare settings in which there are sensitive electronics. For example,

traditional WiFi may interfere with medical devices such as cardiac pacemakers and infusion pumps, while OW-based LANs may provide a safe alternative [21].

However, OW also presents its own constraints and challenges. OW technology typically utilizes direction detection of intensity-modulated light (IM/DD), in contrast to the coherent detection traditionally used by RF communication systems. The conversion at the receiver of intensity-modulated light to an electrical signal is fundamentally different from the conversion of an RF signal and can require a higher concentration of power incident on the receiver [16,17]; in effect, optical receivers are typically orders of magnitude less sensitive than their RF counterparts [17]. Additionally, OW links that operate outdoors can face interference from intense ambient light and atmospheric effects, further increasing the received signal power required for communication [16]. Thus, establishing optical links beyond very short ranges often requires the transmitted energy to be directed towards the receiver with some precision, so that the concentration of received power is sufficient [16]. The consequent alignment demands present a major challenge for OW links [22–24] and have severely limited the adoption of OW for most mobile applications [19].

1.2 Prior and current work in OW

Much recent interest in OW communication has been motivated by applications relevant to indoor local area networks (LANs). The use of OW technology for implementation of indoor LANs was first proposed several decades ago [25], propos-

ing the use of infrared (IR) communication devices to implement local networks within fixed structures environments such as homes and office buildings. Recent interest in OW-based indoor LANs ("LiFi") has shifted from the utilization of IR spectrum to visible light; many see such LEDs as the lighting source of the future [26], and consider room-illuminating LEDs to be a potential low-cost, power-efficient, broadband means of indoor communication [16]. In such systems, it is envisioned that users in the room may receive information via light from an array of fixed overhead LEDs. Such illuminating LEDs in general should provide nearly uniform illumination of relatively high optical powers over wide area for lighting purposes, thus naturally providing a wide coverage area for indoor LANs. In addition, such systems based on visible light LEDs may realize much higher signal-to-noise ratios than IR-based systems, as they need not suffer interference from other interior lighting sources [16, 27].

Due to the short range of these links, the users can receive intensities of LED light sufficient for reasonably high data rates, even without employing precise means of directing transmitted LED light. Typically, the transmitted light is emitted in a wide radiation pattern and covers a wide area, in accordance with the LEDs' role as illuminating devices. The receiver may not even need to have a line-of-sight (LOS) to the transmitter, as reflections from walls can often direct sufficient signal power to the receiver. This wide area of user coverage and insensitivity to alignment or blockages can provide good user mobility within the indoor setting. Such OW links with broad emission patterns and multiple reflections from walls are known as diffuse links.

One challenge that arises in such links is that the reflections within such enclosed spaces also create multiple versions of the signal which are incident on the receiver; each version has its own time delay. This phenomenon, known as multipath dispersion, creates intersymbol interference (ISI) and may limit the bandwidth of such systems. Additionally, the wide receiver fields-of-view utilized in these pointing-insensitive systems allows high levels of interfering ambient light to reach the receiver. To mitigate these effects, some have proposed the utilization of systems which direct the light more precisely than diffuse links do. This includes, for example, the use of multiple "hotspots" [28], or the use of high-speed tracking systems [29]. While these systems may increase the achievable data rates, they may limit mobility of users, increase the complexity of implementation and/or conflict with the demand for illuminating LEDs to provide wide areas of roughly uniform illumination.

Often in such LED-based communication systems, the frequency response of the communication channel is limited most by the modulation bandwidth of the LED. In general, the modulation bandwidths of LEDs depend strongly on the specific device construction. Some have explored μLEDs that have modulation bandwidths that extend into the hundreds of MHz [30–33]. However, much of the interest in using LEDs for communication seeks to exploit large-area LEDs that are lower in cost and thus more practical as sources of lighting, and often such devices can be more limited in their modulation bandwidths. Much of the LED-based OW research explores the use of white LEDs (WLEDs), which are composed of blue LEDs which excite a re-emitting yellow phosphor coating, resulting in spectrally broad emission.

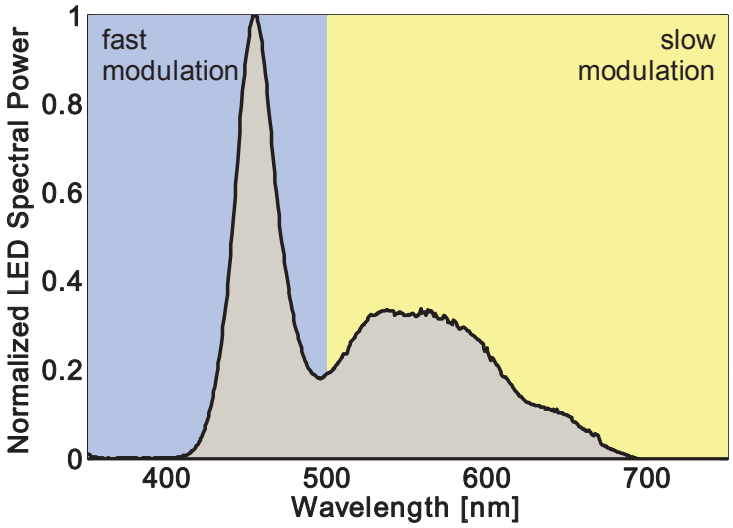

Figure 1.4: Emission spectrum of commercially available phosphor-coated white LEDs, as in [7]. The peak at roughly 450 nm corresponds to emission from the blue LED used to excite the phosphor, which emits broadly across many longer wavelengths. The blue LED typically has a faster modulation response than the broadly-emitting phosphor coating. While white light could also be generated by the use of multiple LEDs, using such phosphor-coated LEDs is generally considered to be a less-expensive means of generating white light.

A typical emission spectrum is shown in Figure 1.4 [7]. As the excitation-reemission process is relatively slow, the use of phosphor-based LEDs can present a challenge to high-data-rate communication applications; they typically have bandwidths limited to a few megahertz. Figure 1.5 shows the normalized gain of such WLEDs and the blue LED used to excite the phosphor [34]. The white LED's 3 dB bandwidth is roughly 3 MHz, while the response of the blue LED is about 10 MHz. [35]. Though white light can also be generated by the combination multiple LEDs (e.g., red, green, and blue), phosphor-based devices are viewed as more practical for lighting purposes due to their simplicity and lower cost.

As this frequency response of white LEDs can create distortion that hinders

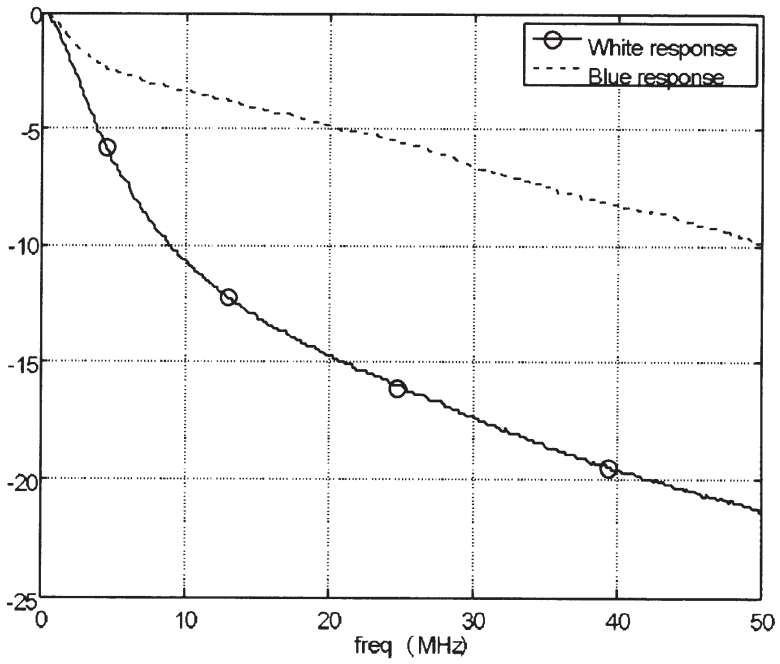

Figure 1.5: Plot of the normalized small-signal frequency response of a white phosphor-based LED, and the blue LED used to excite the phosphor. Generally, the overall white emission is significantly slower in its response than the blue LED's emission. This is due to the long decay time of the phosphor. Plot is as shown in [34].

the creation of high-speed links, attempts to achieve high data rates with LEDs have often sought to address this phenomenon. Such methods include applying a blue filter at the transmitter [36] or receiver [35], though the effectiveness of such methods may depend on the modulation scheme [37]. This blue filter approach attempts to increase the modulation bandwidth of the channel by maintaining the white LED's yellow phosphor emission for lighting purposes, while using only the blue LED's emission for communication purposes.

Beyond simply applying a blue filter, much work has sought to extend the bandwidth of the communication channel using equalization techniques that increase the 3 dB bandwidth of LEDs (whether phosphor-coated or not) [35, 38–40]. In an example of preequalization (equalization implemented in the transmitter), [41] implements OOK modulation using a 16-LED transmitter in which different LEDs are driven with different resonant modulation circuits, each designed to produce peak LED output power at different modulation frequencies. The ensemble of such "tuned" LEDs combine to produce a transmitter that has a significantly increased 3 dB bandwidth, shown in Figure 1.6. Similarly, other work has explored postequalization to increase data rates in which the equalization is performed in the receiver [35, 42]. In addition to equalization techniques, modulation types more sophisticated and bandwidth-efficient than OOK have been used to increase achievable data rates [40,43,44]. These include orthogonal frequency division multiplexing (OFDM), in which the available bandwidth is partitioned into a large number of subchannels [43,44]. In addition to increasing spectral efficiency, such schemes may alleviate limitations to data rates that arise from intersymbol interference (ISI) from

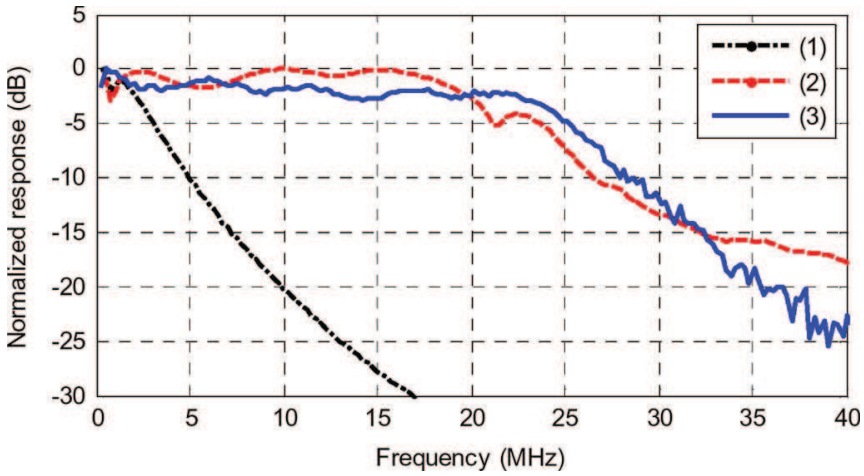

Figure 1.6: To increase the data rates achievable with LED-based communication, techniques such as equalization are used to improve the frequency response of LEDs. Among these techniques is multiple-resonant equalization, which utilizes an ensemble of individual LEDs that are "tuned" to different modulation frequencies to achieve an aggregate frequency response that extends to higher frequencies. This plot illustrates the improvement in such frequency response with three curves showing: (1) normalized gain response of an unequalized LED, (2) the calculated frequency response of an ensemble of LEDs based on measurements of each LED, and (3) the measured frequency response of the ensemble. From [41].

reflection [44–46].

Outside of fixed, enclosed, short-range settings such as indoor LANs, OW is typically manifested as what are known as point-to-point links. These systems require LOS between transmitter and receiver, and point the transmitter and receiver at each other with some degree of precision. Precise alignment allows the use of narrow emission beams (which allow a high concentration of energy to reach the receiver), and narrow receiver fields-of-view (which allow the rejection of most ambient light). And when operated in outdoor environments, these links typically do not suffer much from the limitations of multipath dispersion that arise from reflecting walls.

To date, much of the research in point-to-point OW links has focused on the use of laser-based systems that can span long ranges and achieve very high data rates [18, 47]. With transmission beamwidths on the order of milliradians, these systems enable these rates and ranges by achieving a high concentration of transmitted energy on the incident on the receiver, and also enjoy the spatial reuse and security benefits (protection against eavesdropping and jamming) inherent to directional links [19]. Development of these links has been motivated by applications such as satellite communication [19], airborne communication [48], and building-top metro-area communications [16]. Commercially available laser-based OW systems can achieve data rates on the order of 10 Gb/s at ranges on the order of kilometers [16], and are often considered a less costly alternative to installation of fiber-optic links.

In these long range OW systems, sometimes known as free-space optics (FSO) systems, propagation through the atmosphere can degrade the performance of a system, and limit the achievable data rate. Obscuration due to rain, fog, snow, and haze attenuate the transmitted signal as it propagates [16]. Even in clear conditions, an optical beam can be attenuated by free space loss and clear air absorption [15]. In addition, the transmitted beam is subject to atmospheric turbulence, the randomly varying spatial variations in the index of refraction along the path of propagation [16]. This causes variations on the millisecond timescale [49] of up to 40 dB in the received power level through beam wandering, spreading, and breakup [15]. Such effects, known as scintillation, can become significant for links as short as 500 m [15, 16].

While these atmospheric conditions affect all long-range OW links, the main challenge to adapting such narrow-beam links for mobile applications at any range is the difficulty in achieving the alignment precision required to operate such links. To address these alignment challenges, long-range links are often supported by laser-based beacons that are somewhat wider than the primary data laser. Such links may transmit positioning information or provide alignment feedback, but the beams utilized are still relatively narrow (on the order of one milliradian to tens of milliradians) and assume knowledge of coarse positioning information [50, 51]. Independent RF links are often used for robust support of OW links, sometimes helping to align the optical link [48, 51–57]. In such schemes, RF technology may serve as a beacon for neighbor discovery or the control channel that provides the position information for alignment, as depicted Figure 1.7, taken from [19]. Thus, RF/OW hybrids combine the robustness of RF with the security and access to broad unrestricted spectrum of OW. RF and OW links also complement each other in other ways, as described in Figure 1.8 [48]. However, despite such efforts, OW has still failed to be widely adapted for mobile applications. This lack of penetration into the mobile application space is illustrated in Figure 1.9, which shows that high levels of link performance have only been achieved for links operating under static, favorable conditions.

Some systems to address the alignment concerns of OW systems without the need for RF have been proposed. In one such proposal, nodes are composed of collections of transceivers arrange in a "soccer ball" configuration [47, 58, 59]. The configuration is illustrated in Figure 1.10. Each face of the configuration is an individual transceiver, consisting of a transmitter (LED or LD) and a receiver photodiode

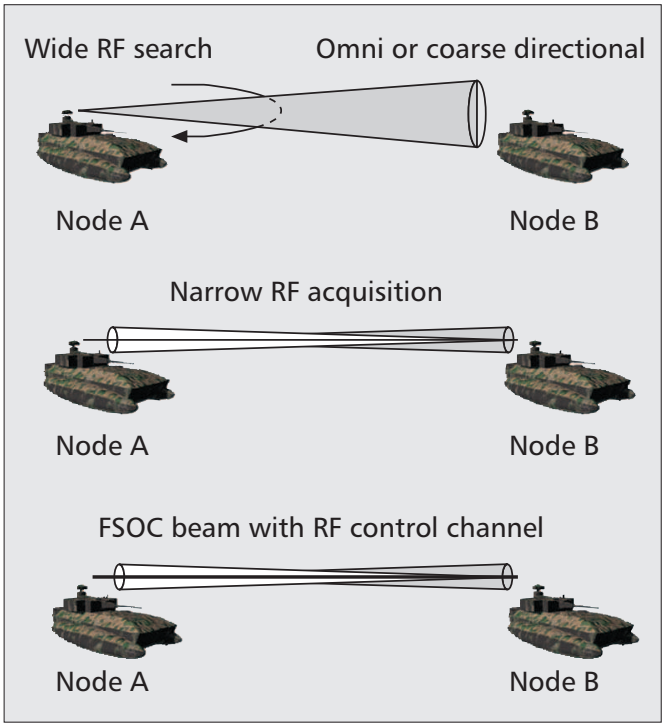

Figure 1.7: Illustration of pointing and tracking with RF/OW hybrid systems, taken from [19]. In general, the difficulty in aligning optical links has motivated the use of more robust RF links as a means of support for optical links. This approach combines the robustness of RF links with the benefits optical links, such as the utilization of unrestricted spectrum. Long range optical links are sometimes referred to as free-space optical (FSO) systems, or free-space optical communication (FSOC) systems. The top two illustrations of the figure depict how RF systems can be used to help align FSOC links. In the absence of prior knowledge of a neighboring node, utilizing omnidirectional or scanning coarse directional RF systems can help to provide the initial acquisition necessary for alignment. With some prior knowledge of the neighboring node, a narrower beam may be used for acquisition; such directional RF beams are in practice much wider than optical beams. Upon acquisition an RF link may be used as a control channel for an FSOC link, as shown in the bottom illustration.

	RF	FSO	RF and FSO
Data Rate	Low data rate	High data rate	Enables High Data Rate Free Space Optical (FSO) communications with High reliability
Channel Stability and QoS	Stable channel	Bursty channel	Improves network availability Quality of Service (QoS)
Impact of Weather	**Impact of Clouds**		
	Relatively immune blocking	Must have clear/haze conditions	RF Operations in Clouds
	Impact of Rain		
	Sometimes affected by rain	Less degradation than RF	FSO Operation in Rain
Ancillary Benefits			Physical Layer diversity improves jam resistance
			Size, Weight, and Power (SwaP) Focus • Leverages common power, stabilization, etc. • Economical use of platform volume

Figure 1.8: From [48], this table compares the characteristics of RF, Free Space Optics (FSO), and hybrid RF/FSO systems. The complementary features of RF and FSO have motivated the use of hybrid systems.

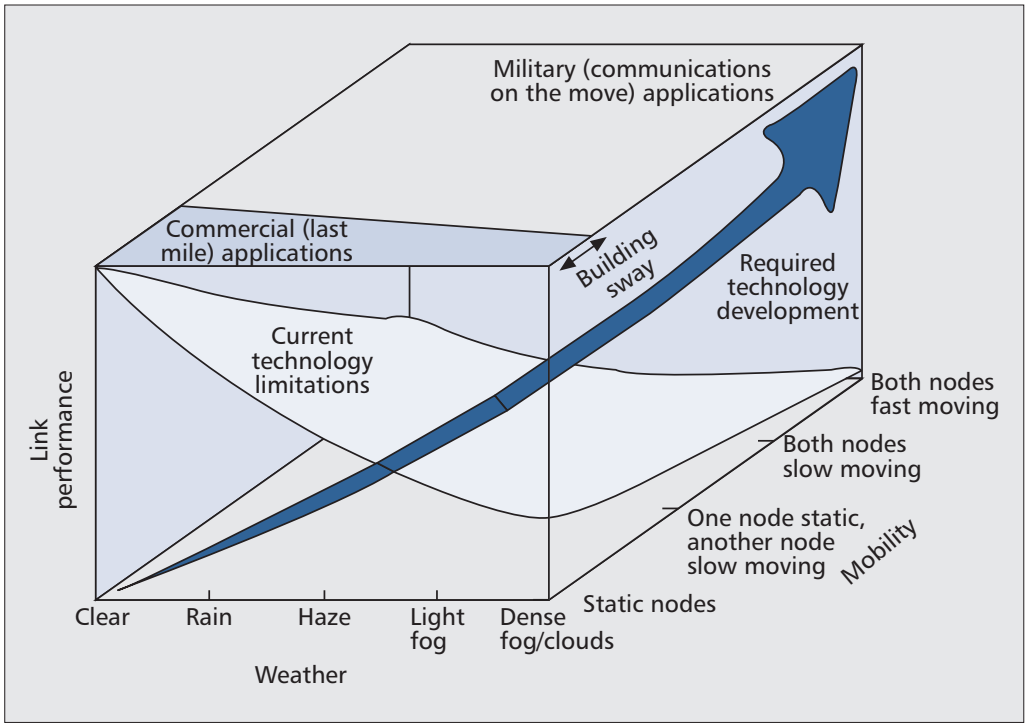

Figure 1.9: State of optical wireless communications, from [19]. Some of the primary obstacles to the widespread implementation of FSO are the difficulty in aligning optical links, and the detrimental effects of some weather conditions on long-range links. To date, practical use of FSO is largely confined to applications that involve static nodes.

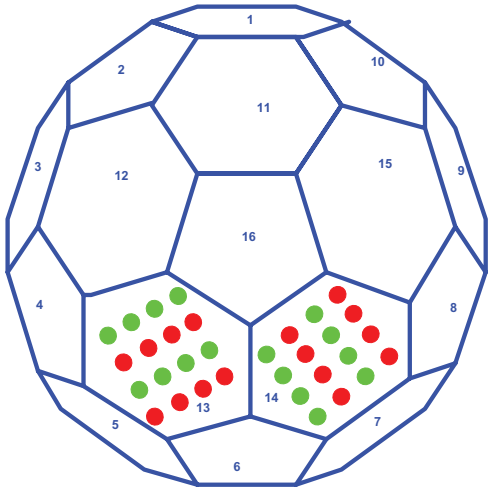

Figure 1.10: "Soccer ball" geometry, as shown in [47]. Each face of the configuration is an individual transceiver, consisting of a transmitter (LED or LD) and a receiver (PD), establishes a connection to a similar transceiver-face on a neighboring node. This form of "electronic steering" allows for multiple connections with similar nodes simultaneously.

(PD), which establishes a connection to a similar transceiver-face on a neighboring node. In the event that a node's link to another node becomes misaligned, the link may shift transceiver-faces to utilize the face that allows for the best alignment. This form of "electronic steering" allows for multiple connections with similar nodes simultaneously. However, it comes at the cost of increased complexity at each node. In addition, the granularity of the electronic steering is limited by the number of faces, making such a system difficult to use for long-range systems.

1.3 Dissertation Contributions

Wireless communication between mobile platforms has traditionally been dominated by RF technology, which has demonstrated the robustness, range, and data

rates necessary for many high-mobility applications. This has included applications such as communication between robots, vehicles, and UAVs. However, the relative immunity from jamming and eavesdropping, lack of interference with other devices, access to unrestricted spectrum, and high bandwidths available to OW systems may make them an attractive supplement to RF technology in some of these mobile applications. OW technology could be especially useful in RF-denied environments, such as some tactical military environments or hospitals with sensitive electronics.

LEDs have emerged as a low-cost, energy-efficient, compact, relatively eye-safe, reliable means of implementing OW communication that could supplement RF in mobile settings. The biggest challenge in this application space is the maintenance of alignment between mobile nodes. While OW has demonstrated the very high rates and long ranges that can be achieved with precise alignment, this thesis will show that LED-based OW links with widened transmission beams and significantly relaxed alignment constraints could provide the robustness necessary for mobile applications while still maintaining useful data rates and ranges. OW technology operating in this regime may be useful as a short- to medium-range means of communication between mobile platforms such as vehicles or robots, especially where RF communication is prohibited or undesirable.

This thesis begins by constructing a channel model for point-to-point LED-based OW communication. This model incorporates design parameters such as noise, alignment error, LED power, beam divergence, receiver size and receiver field-of-view to calculate achievable rates and ranges using on-off-keying (OOK) modulation. The calculations show that even in the presence of outdoor ambient

light, low to medium data rates (kb/s to Mb/s) are achievable over 10s to 100s of meters with a single LED emitter. In addition to providing estimates of the capabilities of OW, the analysis quantifies the tradeoffs embedded in the design of such OW systems.

Following the construction of the OW link model, this thesis uses the model to explore the use of a dual link system as a means of addressing the alignment challenges inherent to point-to-point systems. In the proposed system, a lower-data-rate wide-beam link is used to provide support to a higher-data-rate narrow-beam link. Such a configuration exploits the robustness of the wide-beam link, while the narrow-beam link provides the energy concentration at the receiver necessary to realize sufficient range and data rate. This section of the thesis builds on the general model constructed in Chapter 2 to outline a design framework for the consideration of the proposed dual-link system. The proposed OW system realizes the robustness that accompanies a pointing-insensitive alignment link without relying on the support of an RF link. This all-optical quality may make such a system suitable for RF-denied environments, where OW technology may be of heightened interest.

Expanding upon the use of all-optical means to address the alignment demands of OW systems, Chapter 4 discusses the application of an imaging optical system [19, 20] to provide optical wireless nodes with location information of neighboring nodes. In this system, a curved mirror and a camera constitute an imaging receiver used to estimate the angle-of-arrival of light-emitting sources (beacons) placed on neighboring nodes. Such a system maintains a 360-degree field of view in azimuth without the need for mechanical scanning [60, 61]. Equipped with such a system, a

given node can estimate the angular bearings of nearby nodes, enabling the alignment of OW links. The ranges to nearby nodes can also be estimated with such a system. This information could be used, for example, to estimate the data rate achievable in an optical link [62]. This section of the thesis describes the geometry and operating principles of this beacon localization system and analyzes sources of error in the system. We develop a general analytical model for propagation of Gaussian error in the system and the effect on angle-of-arrival estimation. While the type of errors present in any given implementation may vary considerably, this analytical model may serve as a useful first-order approximation for system modeling and performance prediction. We then present an experimental realization of a catadioptric system and analyze sources of noise in the system.

In Chapter 5 we expand upon the experimental realization discussed in Chapter 4, and discuss the the realization of a self-aligning optical link. This prototype utilizes the catadioptric system's estimates of a nearby beacon to control a gimbal and direct an LED transmitter toward a receiver, thus creating an aligned link.

Chapter 2: Rate and Ranges Achievable with LED-based OW Systems

We begin by considering a general link model of a line-of-sight (LOS) IM/DD OW system that employs on-off keying modulation (OOK) [14]. OOK is frequently used in OW systems due to its reasonable bandwidth efficiency and ease of implementation [4,63]. In this analysis, we consider a distortionless channel, i.e. a channel in which gain is uniform at all frequencies of interest.

In this analysis, we assume that the transmitter has one or a few LEDs that emit light into a hemisphere and that the pattern of emission can be described by an irradiance function $I_{\mathrm{s}}(d,\phi)$ [W/m^2] given by [14] as

$$I_{\mathrm{s}}(d,\phi) = P\frac{m+1}{2\pi}\cos^m(\phi)/d^2. \tag{2.1}$$

Here, d is the distance from the transmitter and ϕ is the pointing angle of the transmitter, as shown in Fig. 2.1. The case of $\phi = 0$ corresponds to a transmitter that is perfectly pointed at the receiver, and thus we will sometimes refer to ϕ as the "pointing error." The average transmitted optical power is P [W], and m is a parameter defining the beamwidth of emission. The half-power half-beamwidth

$\Phi_{1/2}$, which we will refer to as the "beamwidth," is related to m by

$$m = -(\ln 2)/\ln[\cos(\Phi_{1/2})]. \tag{2.2}$$

For a receiver placed at a location defined by (d, ϕ), the received optical signal power P_{Rx} is given by

$$P_{\mathrm{Rx}} = I_{\mathrm{s}} A_{\mathrm{eff}}, \tag{2.3}$$

and the corresponding excited photocurrent is

$$I_{\mathrm{p}} = R P_{\mathrm{Rx}}. \tag{2.4}$$

Here, R [A/W] is the responsivity of the photodiode and A_{eff} [m^2] is the effective area of the receiver. In general, A_{eff} is a function of the angle-of-incidence of the transmitted light at the receiver, which we define as ψ (see Fig. 2.1). The case of $\psi = 0$ corresponds to a receiver that is perfectly pointed at the transmitter. For a receiver that is composed of a photodiode of active area A, an optical filter described by the parameter $T_{\mathrm{s}}(\psi)$, and an optical concentrator of gain $g(\psi)$, the effective area is

$$A_{\mathrm{eff}}(\psi) = g(\psi) T_{\mathrm{s}}(\psi) A \cos(\psi). \tag{2.5}$$

For a given spectrum of LED emission incident on the receiver at an angle ψ, $T_{\mathrm{s}}(\psi)$ is the fraction of incident optical signal power allowed through the filter. If we

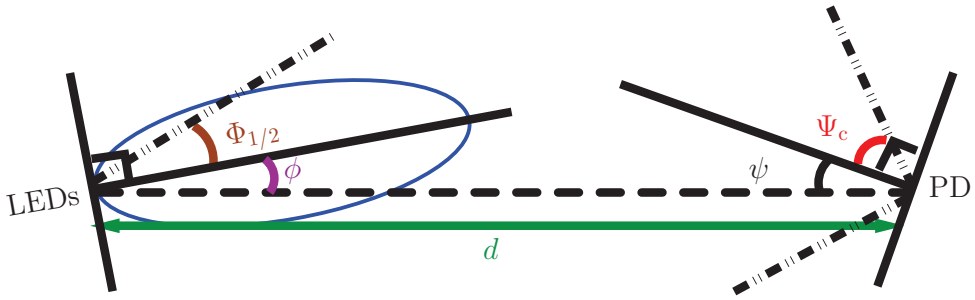

Figure 2.1: Diagram of an optical link with an LED transmitter and photodiode (PD) receiver. The transmitter beam is described by its half-power half-beamwidth $\Phi_{1/2}$ and its pointing error ϕ. A distance d separates the transmitter and receiver. In this model, the field of view of the receiver is defined by the concentrator half-angle Ψ_c. The receiver pointing error is ψ. In this diagram, the angles described by ϕ and ψ are coplanar, but the derived link model is generally valid.

assume that the concentrator is ideal, then its gain g is [64]

$$g(\psi) = \begin{cases} n^2/\sin^2(\Psi_c), & \text{if } |\psi| \leq \Psi_c \\ 0, & \text{if } |\psi| > \Psi_c. \end{cases} \tag{2.6}$$

Here, the concentrator index of refraction is n and its half-angle field-of-view is Ψ_c. Practical concentrators often approach this ideal gain relation [14]. The case of no optical concentrator corresponds to a case of a concentrator with $n = 1$ (free space) and $\Psi_c = 90°$, yielding a gain of $g = 1$.

In OW systems, often the two largest sources of noise are thermal noise [65,66] and shot noise [67], both of which can be modeled as zero-mean white Gaussian noise that is added to the photocurrent I_p. The variance to the signal added by thermal noise is generally modeled as

$$\sigma_{th}^2 = 4kTB/R_{th}, \tag{2.7}$$

where k is Boltzmann's constant, T is the temperature of the detector's load resistor, and B is the receiver bandwidth. We assume that this receiver bandwidth is matched to the bandwidth required to process the modulated signal; for OOK signals, this bandwidth is well-approximated as the bit rate [14]. Thus, in the following discussion we may use "bit rate" and "bandwidth" interchangeably. In general, any resistive element of resistance R_{th} generates fluctuations in current of variance σ_{th}^2 [14]. In a practical receiver, there are often many resistor and non-resistive elements. Sometimes, it is convenient to define R_{th} such that it is an effective resistance to describe the intrinsic noise of a receiver. However, in general the intrinsic noise of a receiver may not necessarily be white, and more complex models may be used [67].

Shot noise is induced by any light that excites photocurrent in the receiver, including ambient light. To reduce the ambient optical power P_{n} [W] that is received by the photodiode, an optical passband filter can be placed on the receiver. In calculating the effect of this filter on the noise level, we model it as a an ideal "boxcar" passband filter of spectral width $\Delta\lambda$ [nm]. With respect to ambient light, the filter has a transmittance T_{n} within the passband and zero outside the passband. A practical filter may have an angularly-dependent transmittance, but in the regime of isotropic ambient light it can be approximately modeled as a boxcar filter of effective passband width $\Delta\lambda$. We also assume that the ambient background noise incident on the receiver is "white" (constant within the passband), and define its spectral irradiance (power per unit photodetector area per unit spectrum) as p_{bg} [W/nm-cm^2]. With an ideal optical concentrator of index of refraction n, the

ambient optical power incident on the photodiode is [14]

$$P_{\mathrm{n}} = p_{\mathrm{bg}} \Delta\lambda T_{\mathrm{n}} A n^2. \tag{2.8}$$

Along with the received signal of power P_{Rx}, this ambient light of power P_{n} creates shot noise in the receiver, which is typically modeled as additive zero-mean white Gaussian noise (AWGN) that is added to the received photocurrent, where the variance σ^2_{shot} [A^2] of the AWGN can be approximated by [67]

$$\sigma^2_{\mathrm{shot}} = 2qRB(P_{\mathrm{n}} + P_{\mathrm{Rx}}). \tag{2.9}$$

Here, $-q$ [C] is the charge of an electron, B [bits/s] is the bit rate of the signal, and R [A/W] is the responsivity of the photodiode. In practical OW systems, and especially for outdoor systems, the power of received ambient light is much greater than that of transmitted signal power. That is, $P_{\mathrm{Rx}} \ll P_{\mathrm{n}}$ [14, 17, 66, 68, 69]. The combination of thermal and shot noise yields a total induced noise

$$\sigma^2 = \sigma^2_{\mathrm{th}} + \sigma^2_{\mathrm{shot}}. \tag{2.10}$$

We use these model of thermal and shot noise to to define a signal-to-noise ratio (SNR) at the receiver,

$$\mathrm{SNR} \equiv \frac{I^2_{\mathrm{p}}}{\sigma^2} \tag{2.11}$$

Within this framework defined by additive white Gaussian noise, SNR is related to

bit-error rate (BER) by

$$\mathrm{BER} = Q(\sqrt{\mathrm{SNR}}), \tag{2.12}$$

where $Q(\cdot)$ is the tail probability of the standard normal distribution [14].

In outdoor systems, ambient-light-induced shot noise often dominates all other noise sources, allowing Equation (2.11) to be reexpressed as

$$\mathrm{SNR} = \frac{I_{\mathrm{p}}^2}{2qRBP_{\mathrm{n}}} \tag{2.13}$$

Thus, we can relate the bit rate B, ambient shot noise level, average transmitted power, range, beamwidth, and BER. Combining Eq. (2.9)–(2.12) and solving for B yields the rate

$$B = \frac{R^2 P_{\mathrm{Rx}}^2}{2qRP_{\mathrm{n}}[Q^{-1}(\mathrm{BER})]^2}. \tag{2.14}$$

To solve for the range, we substitute Eqs. (2.1) and (2.3) into Eq. (2.14), yielding

$$d = \left(\frac{1}{2qRP_{\mathrm{n}}B}\right)^{1/4} \left[\frac{RA_{\mathrm{eff}}P(m+1)\cos^m(\phi)}{2\pi Q^{-1}(\mathrm{BER})}\right]^{1/2}. \tag{2.15}$$

In general, the total achievable bit rate can be increased by operating such optical links in parallel, though this may be undesirable in terms of power consumed, cost, footprint and other parameters. Brightness may be constrained, for example, for LEDs that are being used as illumination devices. In the absence of considerations such as brightness, a system in which a single LED channel has a bit rate of B can be simply scaled, such that if N of these LED channels operate simultaneously and independently, then the total bit rate is simply $N \times B$. This of course requires

increasing the total received optical power by a factor of N. However, if instead the optical power is constrained while increasing the number of channels from 1 to N, then each channel is allocated P/N transmitted power, and each channel receives P_{Rx}/N power. If we define k_{r} as $k_{\mathrm{r}} = R^2/2qRP_{\mathrm{n}}$, each channel has an achievable bit rate of

$$B_n = k_{\mathrm{r}} \frac{(P_{\mathrm{Rx}}/N)^2}{[Q^{-1}(BER)]^2} \tag{2.16}$$

And the aggregate bit rate across all N of the OOK channels is

$$B_N = N \times B_n = N k_{\mathrm{r}} \frac{(P_{\mathrm{Rx}}/N)^2}{[Q^{-1}(BER)]^2} = \frac{1}{N} B \tag{2.17}$$

The aggregate bit rate decreases as $1/N$, for a fixed total optical power. Thus, within this framework of independent channels, a system constrained by optical power is optimized by concentrating its optical power in a single channel.

In the OOK modulation scheme that such an analysis assumes, in each bit interval, only a 0 (off) or 1 (full intensity) is allowed to be transmitted. If instead we allow for L levels of intensity to be transmitted, we are utilizing what is known as L-level Pulse-Amplitude Modulation (L-PAM). In this scheme the intensity of a given interval can encode more than one bit of information. Each of the L levels can be thought of as a symbol in an alphabet of L symbols. A set of L levels means that each symbol is a represntation of $\log_2 L$ bits of information. The $L = 2$ case is equivalent to the OOK case. For L-PAM, the bit error rate for a given bit rate

B_{PAM} is [67]

$$BER = Q(\frac{\sqrt{\log_2 L}}{L-1}\sqrt{\text{SNR}}). \tag{2.18}$$

Solving for the bit rate B_{PAM} and relating it to the OOK bit rate B, we have

$$B_{\text{PAM}} = \frac{\log_2 L}{(L-1)^2}\frac{P^2}{[Q^{-1}(BER)]^2} = \frac{\log_2 L}{(L-1)^2}B \tag{2.19}$$

The bit rate B for OOK and B_{PAM} only differ by the factor $\frac{\log_2 L}{(L-1)^2}$. Thus, as the number of LED channels increases to N while optical power is fixed, L-PAM's aggregate bit rate experiences the same $1/N$ dependence shown in Eq. 2.17.

2.1 Optical Filter Design

One way to implement more than one parallel channel is wavelength division, i.e., the use of different colors. The optical spectra of red, green, and blue LED emission are shown in Figure 2.2. There is clear overlap between some of the spectra, particularly between the blue and green channels. This section addresses a channel's performance as a function of the corresponding receiver's optical filter width, given the potential for overlapping interference between channels.

Specifically, we address filter design for the blue channel, which involves considerations of the interference from the green LED. For simplicity we assume a "boxcar" shaped optical filter, meaning that the filter does not attenuate anything in its passband and completely rejects energy outside its passband. We also assume this filter is centered at 460 nm, which is roughly the center of the blue LED's emis-

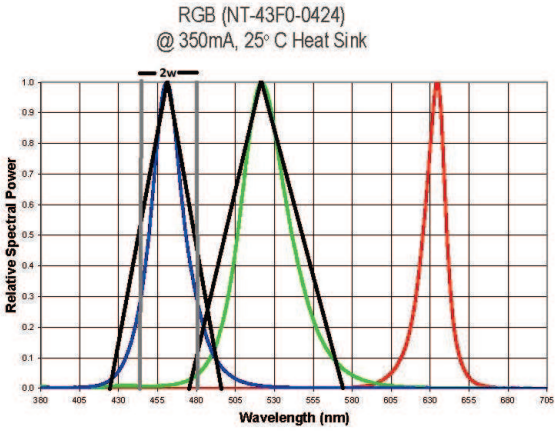

Figure 2.2: Normalized optical spectra of commercially available red, green, and blue (RGB) LEDs. The two black triangles imposed over the blue and green spectra illustrate the triangular approximation of the spectra that is used in this section to consider optical filter design. The two grey lines spaced $2w$ apart define the filter width assumed in this analysis. NT-43F0-0424 is the model of the commercial LED considered, while 350 mA is the assumed driving current of each LED.

sion. The filter's width is defined as $2w$, and we examine how the blue channel's bit error rate varies as a function of w.

In this analytical approach, we approximate the spectra of the LEDs to be isosceles triangles. The blue LED emission is approximated as an isosceles triangle that peaks at 460 nm, and has a base that extends from 425 nm to 495 nm (35nm to the left and right of the 460nm center). The green LED emission is modeled as an isosceles triangle centered at 525nm, with a base extending from 475 nm to 575 nm (50nm to the left and right of center). In this approximation, the blue LED emission and green LED emission overlap between 475 nm and 495 nm.

Because we have approximated the blue LED's emission as extending from (425=460-35) nm to (495=460+35) nm, we analyze the link's performance for optical filter half-widths (w) between 0 nm and 35 nm. Generally there is a tradeoff in filter

design: increasing w will increase the received blue LED signal power, but also invite more interference from the green LED. Intuitively, we can expect that increasing w beyond 35 nm would only degrade performance, as no blue LED light exists beyond 35nm away from the blue center wavelength (460nm). It is also clear that for any w less than 15nm, there is no interference from the green LED; the filter is simply not wide enough to capture any of the green LED's emission.

We assume that ambient-induced shot noise is the dominant source of noise, and adds a zero-mean additive Gaussian noise of $\sigma^2 = 2q(2w)RP_{bg}B$ [A^2] to the induced current. Here, $-q$ is the charge on an electron, $2w$ is the optical filter width, R is the responsivity of the blue channel's photodetector, P_{bg} is the level of ambient noise, and B is the modulation bandwidth. Thus, σ increases with the square root of w. The ambient noise level P_{bg} is assumed to be 10 μW/nm.

The type of modulation we analyze here is on-off-keying, with the blue and green channels, operating independently, but synchronized and operating at the same bit rate. We assume each channel has a total average optical power P_{Rx} incident on the receiver (prior to interacting with the optical filter); that is, the area of each of the triangles in Figure 2.2 are equal to each other and proportional to P_{Rx}. Using simple geometrical considerations of triangles, we can find the filtered optical power that is allowed to reach the blue channel's photodetector, as a function of w. The blue LED's filtered average signal power is $P_{\mathrm{Rx}} - \frac{P_{\mathrm{Rx}}}{35^2}(35-w)^2$, while the green LED's filtered average interfering power is $\frac{P_{\mathrm{Rx}}}{2\times 50^2}(w-15)^2$. In general, the average

optical power P_{Rx} incident on the receiver is :

$$P_{\mathrm{Rx}} = A_{eff} P \frac{m+1}{2\pi} \cos^m(\phi)/d^2 \tag{2.20}$$

Here, A_{eff} is the effective area of the photodetector, R is the photodetector responsivity,$m = \ln(1/2)/\ln(\cos(\Phi_{1/2}))$ where Φ_{12} is the half-power beamwidth, ϕ is the transmitter pointing angle, P is each channel's transmitted optical power, and d is the distance between transmitter and receiver.

Each LED can be either on or off, and we will assume that each is on 50% of the time and off 50% of the time, that the probabilities of the two channels are uncorrelated. For the cases where the green LED is off, the error analysis of the blue channel is the same as it would be normally, without the green LED. There are two types of errors: reading a 1 given that a 0 was transmitted (probability $P(1:0;\mathrm{GreenOff})$, and reading a 0 given that a 1 was transmitted ($P(0:1;\mathrm{GreenOff})$). The probabilities can be be stated as:

$$P(1:0;\mathrm{GreenOff}) = \int_{i_s/2}^{\infty} \frac{1}{\sigma\sqrt{2\pi}} \exp\left(-\frac{x^2}{2\sigma^2}\right) dx. \tag{2.21}$$

$$P(0:1;\mathrm{GreenOff}) = \int_{-\infty}^{i_s/2} \frac{1}{\sigma\sqrt{2\pi}} \exp\left[-\frac{(x-i_s)^2}{2\sigma^2}\right] dx. \tag{2.22}$$

Here, i_s is the current that should be induced by the blue LED in the presence of a "1" transmitted ($i_s = 2R(P - \frac{P}{35^2}(35-w)^2)$, where R is the responsivity [A/W]). The shot noise is represented by σ [A]. The two probabilities of these

errors should be equal with the decision threshold set to $i_s/2$, given symmetry considerations. We limit our analysis to this this threshold value, though a blue-LED-receiver with knowledge of the green LED's probability of interference may incorporate this knowledge to optimize the threshold for link performance. In effect, the threshold chosen here for the blue LED receiver is optimized for the case of the green LED being off.

If the green LED is on, the same two kinds of errors can be made, but the expressions in the presence of green LED light are altered. Specifically, the green LED's light induces a photocurrent that adds to the blue LED's photocurrent, thus shifting that Gaussian distribution used to calculate the probability of errors. This is shown in the following equations:

$$P(1:0;\text{GreenOn}) = \int_{i_s/2}^{\infty} \frac{1}{\sigma\sqrt{2\pi}} \exp\left[-\frac{(x-i_G)^2}{2\sigma^2}\right] dx. \tag{2.23}$$

$$P(0:1;\text{GreenOn}) = \int_{-\infty}^{i_s/2} \frac{1}{\sigma\sqrt{2\pi}} \exp\left\{-\frac{[x-(i_s+i_G)]^2}{2\sigma^2}\right\} dx. \tag{2.24}$$

Here, i_G is the current induced by the green LED when it is on ($i_G = 2R(\frac{P}{2\times 50^2}(w-15)^2)$). For all four cases, σ is the same. We consider it to depend only on the ambient light, and not on any of the signals, as the incident ambient light is assumed to be much greater than that from any of the LEDs.

Given that each of these four errors should be equally probable for two uncor-

related channels (blue and green), the overall error rate is the average:

$$P_{error} = (1/4)[P(1:0;\text{GreenOff})+P(0:1;\text{GreenOff})+P(1:0;\text{GreenOn})+P(0:1;\text{GreenOn})] \tag{2.25}$$

Figure 2.3 plots the logarithm of P_{error} as a function of w for several different distances d. The bit error rate reaches a minimum; for the distances shown, this occurs at around w of 20-25 nm. These curves behave qualitatively similarly at distances beyond 42m, except with higher error rates. This figure assumes $A_{eff} =$ 1cm^2, $R = 0.7$A/W, $P_{bg} = 10\mu$W/nm, $B = 1$ Mbit/s, $\Phi_{1/2} = 45°$, and $\phi = 0°$.

Figure 2.4 is similar, except that it plots the probabilities of each of the four types of errors, for a single distance ($d = 12$m). For $w < 15$nm, all four types of errors are equally probable. This is because the σ is the same for all cases, there is no green LED interference in this regime, and the decision threshold is half of i_s .

Increasing w beyond 15 nm brings green LED light into the passband, and the "green on" cases diverge from the "green off" cases. The "green off" cases split from each other as well. Adding a green LED-induced current to the signal-induced current increases the probability of reading a "1" when a "0" was transmitted, while decreasing the probability of reading a "0" when a "1" was transmitted.

Note that even in the "green off" cases, which behave as though there were no green LED at all, reach a BER minimum at a w less than 35 nm (i.e., where the filter width is still completely contained in the blue LED spectrum). That is, increasing the filter width beyond about $w = 24$nm only serves to worsen performance. This can be solely attributed to the increase of shot noise with filter width, as the green

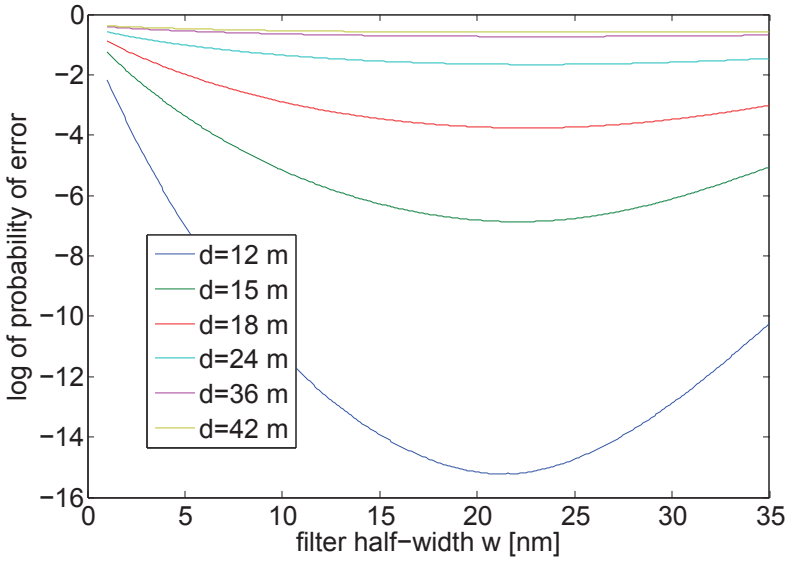

Figure 2.3: Probability of error as a function of filter half-width w, for several distances d. The green LED is assumed to be temporally aligned with the blue LED.

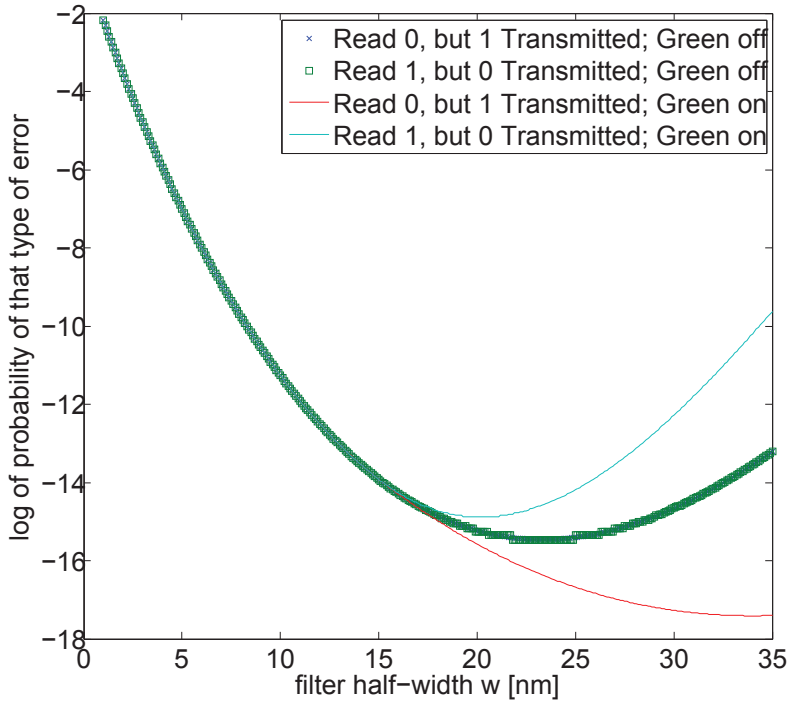

Figure 2.4: Probabilities of the four types of errors as a function of filter half-width w, for $d = 12$m. The green LED is assumed to be synchronized and temporally aligned with the blue LED.

LED plays no role here. While it is true that increasing the filter width beyond $w =$ 24nm increases the total blue LED signal power received, at this point the marginal benefit of increasing the signal power received is outweighed by the marginal cost of increased shot noise.

Up to this point, the analysis has assumed that the blue and the green LEDs are transmitting at the same bit rate, with the bit periods perfectly aligned. If the green LED's timing and bit rate are unknown, these calculations change. If we know nothing about the green LED's timing, then we can model its effect using a probability density function. The interfering photocurrent from the blue LED can be modeled as being anywhere between 0 and $i_G = 2R(\frac{P}{2\times 50^2}(w-15)^2)$, where i_G corresponds to "green on" case (i.e., the green LED channel transmitting a "1"). Given the assumption of ignorance about the green LED's timing, we take the probability density function to be uniform between these two bounds.

With each photocurrent between 0 and i_G, there is an associated probability of falsely reading a 0, and also of falsely reading a 1. Thus each of the two types of errors has an associated probability distribution of probabilities. An estimate for each of the two types of errors can be made by taking the average or expectation values of each probability distribution. As the green LED interfering current is always additive, it increases the probability of reading a 1 when the signal was a 0, while decreasing the probability of reading a 0 when the signal was a 1. The overall probability of error for the blue LED link is taken as the average of these two error probabilities.

Figure 2.5 plots the probability of error in the blue LED link for this case of

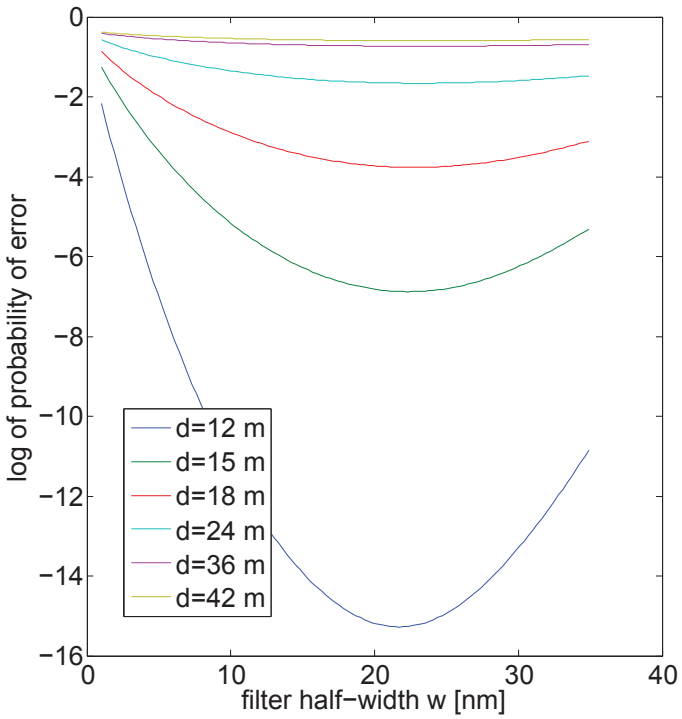

Figure 2.5: Probability of error as a function of filter half-width w, for several distances d. Here we assume the blue and the green LEDs are unsynchronized.

an "unsynchronized" green LED, as a function of w, for several distances. It is quite similar to Figure 2.3 despite the different assumptions made about the green LED's interference.

Figure 2.6 examines probability of error for a few different types of cases, for a given distance d. The first cases, corresponding to the diamonds and asterisks, are the probabilities of reading false 0's and false 1's assuming an unsynchronized green

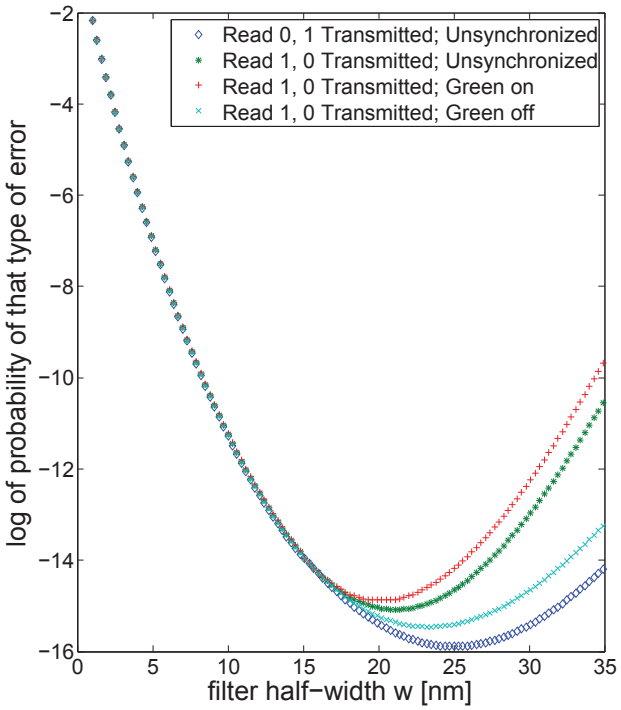

Figure 2.6: Probabilities of the four types of errors as a function of filter half-width w, for $d = 12$m. The green LED is assumed to be unsynchronized for the first two cases.

LED channel. The probability of reading a false 1 in the presence of green LED light can be much higher than the other probabilities at large w, as it is in Figure 2.4. As this probability of a false 1 in the presence of green LED light can be considerably higher than that of a false 0, it dominates the calculation of the total average bit error rate, and any consequent filter design considerations. We see that operating the blue channel in the presence of the green LED, whether synchronized or not, significantly increases the probability of reading a false 1 for large filter widths.

2.2 Calculations of Achievable Rates and Ranges

Using the link model developed in the previous section, we calculate achievable rates and ranges as a function of realistic parameters such as a beamwidth and pointing errors. In making these calculations, we assume reasonable parameter values for detector active area A, ambient noise level p_{bg}, concentrator index of refraction n, receiver filter transmissivity T, filter width $\Delta\lambda$, transmitted optical power P and photodiode responsivity R. Commercially available LEDs vary in their spectra and power, but we consider an LED that consumes approximately 1 Watt in electrical power and emits $P = 0.3$ W as a reasonable representation of commercially available devices. Though ambient noise levels certainly vary greatly with environmental conditions, $p_{\text{bg}} = 5.8$ $\mu\text{W/cm}^2\text{/nm}$ is commonly accepted in previous work as representative of bright outdoor ambient light [67]. The optimal filter width $\Delta\lambda$ may depend on factors such as ambient noise levels and the spectral width of LED emission. We assume $\Delta\lambda = 50$ nm, as filter widths are of the same

order as the LED spectral widths, and similar filter widths are often assumed in the literature [67]. Note that $\Delta\lambda$ as defined here is not necessarily equivalent to the half-power full-bandwidth that can commonly be extracted from commercially available filters' datasheets. Such transmission spectra (see Figure 2.8) [70] typically describe filter behavior at normal incidence only. In the model used in this thesis, $\Delta\lambda$ is defined as an effective bandwidth for acceptance of isotropic radiation that impinges on the filter from many angles, not merely normal incidence. In practice, this distinction may be relatively inconsequential [71]. Figure 2.2 shows emission normalized emission spectra for commercially available red, green, and blue LEDs, which have spectral widths on the order of our chosen filter width. The radiation patterns of commercially available LEDs are shown in Figure 2.10. The responsivity R is defined as the photocurrent excited per unit optical power received by the receiver's photodiode. In general, this varies as a function of wavelength. For the silicon photodiodes frequently used in OW systems, the responsivity as a function of wavelength is plotted in Figure 2.7, as measured by Thorlabs [70]. We assume that $R = 0.6$ A/W in our calculations here. The transmissivity T is fraction of the LED light that is let through by the filter, and is dependent on the overlap of the filter transmission spectrum and the emitting LED spectrum. In our calculations, we assume that 80% of the emitted LED light incident on the receiver is able to reach the photodiode, i.e., $T = 0.8$. The assumed parameter values are shown in Table 2.2.

Using these parameter assumptions and Equation (2.14), we generate contour maps of the achievable bit rates B as a function of receiver position relative to an

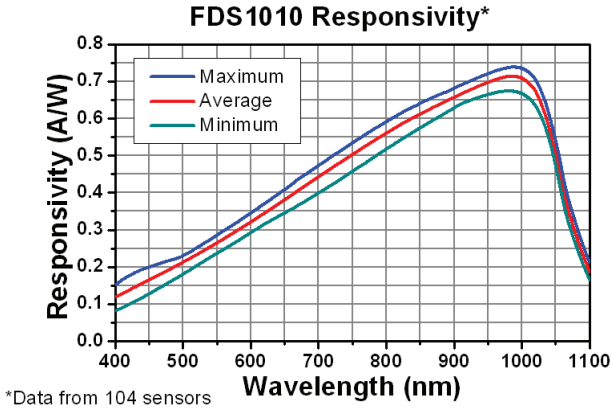

Figure 2.7: Responsivity of silicon photodetectors, from [70].As the exact responsivity can vary from unit to unit due to manufacturing considerations, three curves the maximum, average, and minimum responsivities from a survey of Thorlabs FD1010 units.

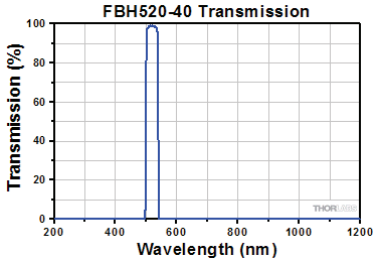

Figure 2.8: Sample of transmission spectrum of commercially available filter [70].

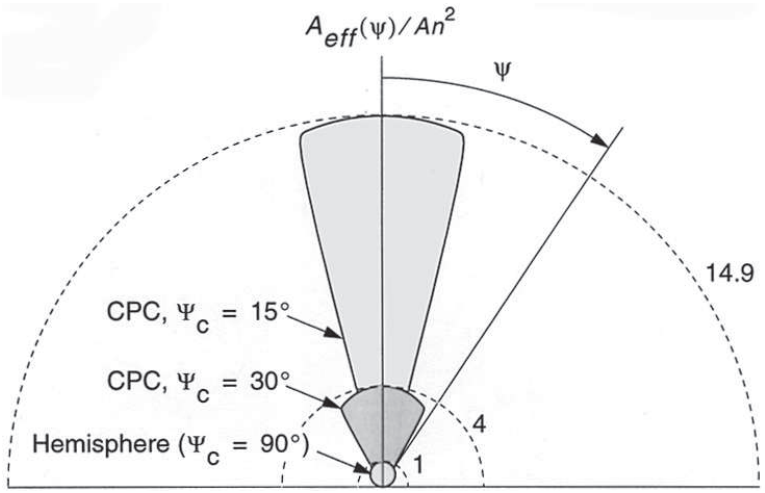

Figure 2.9: Plots of gain achieved by ideal concentrators assuming lossless filters, as a function of incident angle ψ, as shown in [14]. Compound parabolic concentrators (CPC) are commercially available devices [72] which can nearly achieve the ideal gains plotted here. For the case of the widest FOV, $\Psi_c = 90°$, the nonimaging concentrator takes the form of a hemisphere.

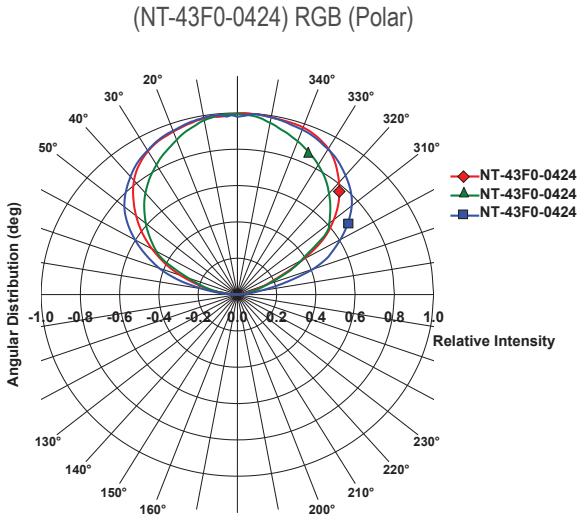

Figure 2.10: Polar plots of radiation patterns of commercial red, green and blue LEDs.

A	0.1 cm^2
p_{bg}	5.8 $\mu\text{W/cm}^2\text{/nm}$
$\Phi_{1/2}$	8.4°
BER	10^{-4}
P_{Tx}	0.3 W
Ψ_{c}	10°
$\Delta\lambda$	50 nm

Table 2.1: Assumed parameters in the calculations in this section.

LED transmitter. Figure 2.11 shows a contour map of these calculations. In this plot, the LED transmitter is placed at $(x, y) = (0,0)$ and oriented to emit light in the positive y-direction. The contours are a logarithmic representation of the achievable bit rate, where, for example, $B = 10^3$ bits/second is represented by a contour of "3." At any given point in the plot, the corresponding bit rate B is the bit rate achievable using a photodetector that is pointed directly at the transmitting LED ($\psi = 0°$). Such plots give rough estimates of the achievable rates and ranges, and also show the sensitivity of achievable rates to transmitter pointing angle ϕ. In this contour plot, we see that megabit-per-second data rates are achievable at ranges of hundreds of meters, with a single LED.

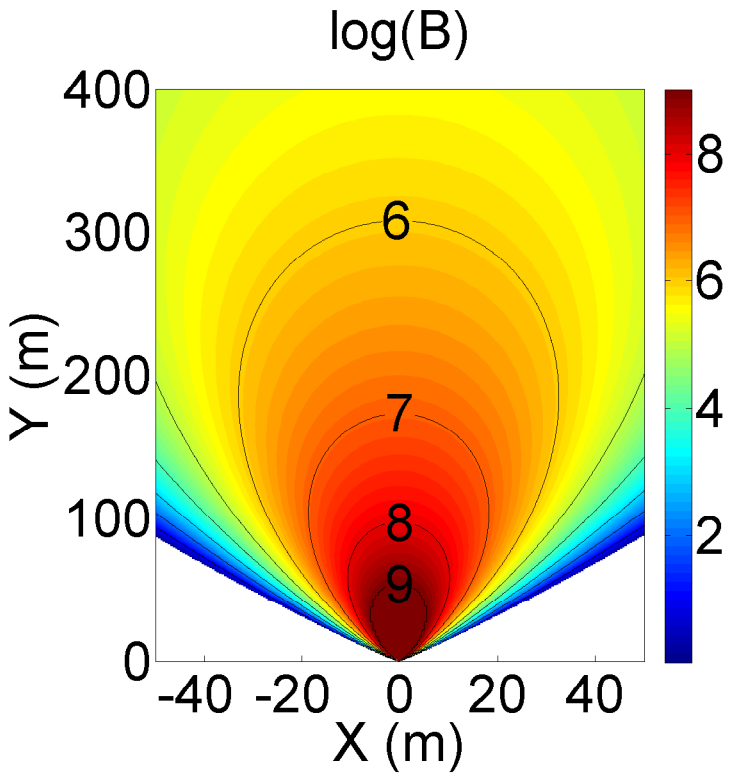

Figure 2.11: In this plot, the LED transmitter is placed at $(x, y) = (0,0)$ and oriented to emit light in the positive y-direction. The contours are a logarithmic representation of the achievable bit rate, where, for example, $B = 10^3$ bits/second is represented by a contour of "3." At any given point in the plot, the corresponding bit rate B is the bit rate achievable using a photodetector that is pointed directly at the transmitting LED ($\psi = 0°$). Such plots give rough estimates of the achievable rates and ranges, and also show the sensitivity of achievable rates to transmitter pointing angle ϕ. In this contour plot, we see that megabit-per-second data rates are achievable at ranges of hundreds of meters, with a single LED.

Chapter 3: Design of Dual-Link System

3.1 Design of wide beam/narrow-beam dual link system

Using the link model developed in the previous chapter, we explore the use of a wide-beamwidth LED-based link acting as a support link for a more focused, narrow-beam link. The structure of such a system is illustrated in Figure 3.1.

3.1.1 Defining the role of the beacon link

We refer to the wide-beam link as the beacon link, and the narrow-beam link as the primary link. Throughout this discussion, subscripts b and p will be used to denote parameters relevant to the beacon link and primary link, respectively. For instance, we define $\Psi_{c,b}$ as the concentrator field of view for the beacon link receiver and $\Psi_{c,p}$ as that for the primary link receiver. The pointing angles of the beacon and primary transmitters are ϕ_b and ϕ_p, respectively, and the pointing angles of the beacon and primary receivers are ψ_b and ψ_p, respectively. To avoid interference between the two links, there is a need to ensure orthogonality between them; this could be achieved, for instance, by using LEDs of different wavelengths for the two links or time-division multiplexing their communication.

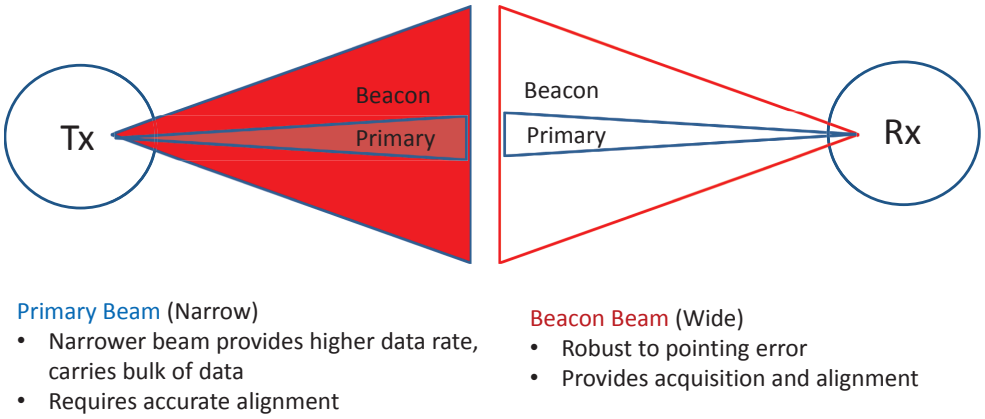

Figure 3.1: A dual-link system utilizes the advantages of a relatively alignment-insensitive beacon link, while providing the higher throughput of a narrower beam.

The primary link has a more focused beam than the beacon link and is expected to support a much higher data throughput than the beacon link. Operating such a relatively directional link, however, can introduce alignment challenges, especially in mobile scenarios. To address this, we propose the joint use of the supporting beacon link. The beacon link need not provide a high data rate; rather, its purpose is to provide low-data-rate connectivity for a wide range of beacon transmitter pointing angles ϕ_{b} and beacon receiver pointing angles ψ_{b}. This low rate connectivity could be used, for example, to provide positioning and alignment information for the primary link. There are many different ways this supporting link could help align the primary link; among the demonstrated uses of supporting links in FSO systems have been the transmission of GPS coordinates, inertial orientation information, and received signal strength (RSS) [73]. Regardless of the specific role chosen for the beacon link, the beamwidths we examine for both links are on the order of tens

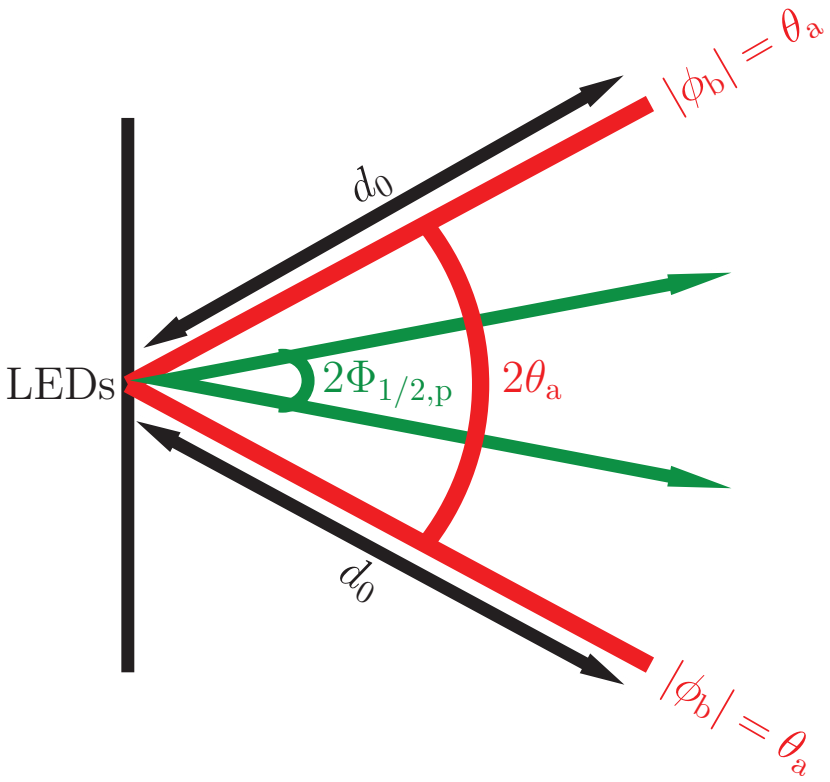

Figure 3.2: Diagram of beacon-link coverage range and the primary link beamwidth. A receiver positioned in the angular range $|\phi_b| \leq \theta_a$ is guaranteed a beacon connection ($B_b \geq B_{b0}$) if its range is less than or equal to d_0. The beacon beamwidth is $\Phi_{1/2,\,b}$ (not shown), while the primary link beamwidth is $\Phi_{1/2,\,p}$.

of degrees, which significantly relaxes alignment constraints relative to that of many FSO systems. By utilizing both links, the dual-link system exploits the robustness of the beacon link while maintaining the high throughput of a relatively focused primary link. This robustness makes it suitable for LED-based outdoor mobile applications, a regime that has been studied significantly less than the indoor local area network application space [1, 2, 27, 40, 68].

The beacon link provides robustness by virtue of its relatively large beamwidth $\Phi_{1/2,b}$, which relaxes the beacon pointing demands. In designing the exact beamwidth of the beacon transmitter, there is a tradeoff between this robustness in pointing

and the transmitter-to-receiver distances (d) that allow for connectivity; narrower beams can allow for longer-distance links but demand that the beacon transmitter be pointed with relative precision, whereas links with wider beams are more limited in their range but allow for more relaxed pointing demands.

We approach the design of the beacon link beamwidth $\Phi_{1/2,\mathrm{b}}$ by specifying a constraint on the pointing precision of the beacon transmitter. Specifically, we demand that the greatest pointing error allowed is $|\phi_\mathrm{b}| = \theta_\mathrm{a}$; in some sense, this defines an "angular range" of operation for the beacon link. In addition, we demand that for each ϕ_b within this permitted angular range ($-\theta_\mathrm{a} \leq \phi_\mathrm{b} \leq \theta_\mathrm{a}$), the beacon link supports a minimum data rate $B_{\mathrm{b}0}$ (i.e., $B_\mathrm{b} \geq B_{\mathrm{b}0}$). Note that this minimum rate is achievable at a different range d for each of the angles ϕ_b within this angular span.

The shortest of these distances d corresponds to $|\phi_\mathrm{b}| = \theta_\mathrm{a}$, the worst case of pointing within the stated constraints. We design the beacon link beamwidth $\Phi_{1/2,\mathrm{b}}$ to maximize this worst case range, because we are interested in optimizing the robustness of the beacon link over a wide range of pointing angles ϕ_b, rather than optimizing the performance of the link for cases of perfect pointing ($\phi_\mathrm{b} = 0$). To do this, we set $\phi_\mathrm{b} = \theta_\mathrm{a}$ and differentiate Eq. (2.15) with respect to m. The parameter m defines the beamwidth via Eq. (2.2). The optimal m that results is

$$m_\mathrm{b} = -1 - 1/\ln[\cos(\theta_\mathrm{a})], \tag{3.1}$$

with a corresponding optimal beacon beamwidth defined by

$$\Phi_{1/2,\mathrm{b}} = \cos^{-1}\left[\exp\left(-\frac{\ln 2}{m_{\mathrm{b}}}\right)\right]. \tag{3.2}$$

$$\Omega_{1/2,\mathrm{b}} = \cos^{-1}\left[\exp\left(-\frac{\ln 2}{m_{\mathrm{b}}}\right)\right]. \tag{3.3}$$

Substituting this optimal $m = m_{\mathrm{b}}$ and $\phi_{\mathrm{b}} = \theta_{\mathrm{a}}$ back into Eq. (2.15) yields the maximized range for this worst case of pointing, and we define this range as d_0.

With this optimal beamwidth, beacon connectivity ($B_{\mathrm{b}} \geq B_{\mathrm{b0}}$) is guaranteed to any receiver that lies d_0 or less away from the transmitter, within the angular range $-\theta_{\mathrm{a}} \leq \phi_{\mathrm{b}} \leq \theta_{\mathrm{a}}$. Note that connectivity at ranges greater than d_0 can be established for $|\phi_{\mathrm{b}}| < \theta_{\mathrm{a}}$, as well as for ranges less than d_0 for $|\phi_{\mathrm{b}}| > \theta_{\mathrm{a}}$. A diagram that illustrates the geometry of the angular range $|\phi_{\mathrm{b}}| \leq \theta_{\mathrm{a}}$ and distance d_0 is shown in Fig. 3.2. In practice, a single node can employ several beacons to "cover" a wider range of azimuthal and/or elevation angle, building on angle-diversity schemes that have been explored [47, 59]. However, the analysis in this work will focus on the use of a single beacon per node.

In general, the value of d_0 depends on many parameters [see Eq. (2.15)], including the required beacon rate B_{b0}; very low values of B_{b0} may be attainable at long distances, whereas higher rates may correspond to more limited ranges. The value of B_{b0} itself depends on the desired used of the beacon link. Using the beacon link for acquisition and feedback control, for example, may require $B_{\mathrm{b0}} \approx 1$

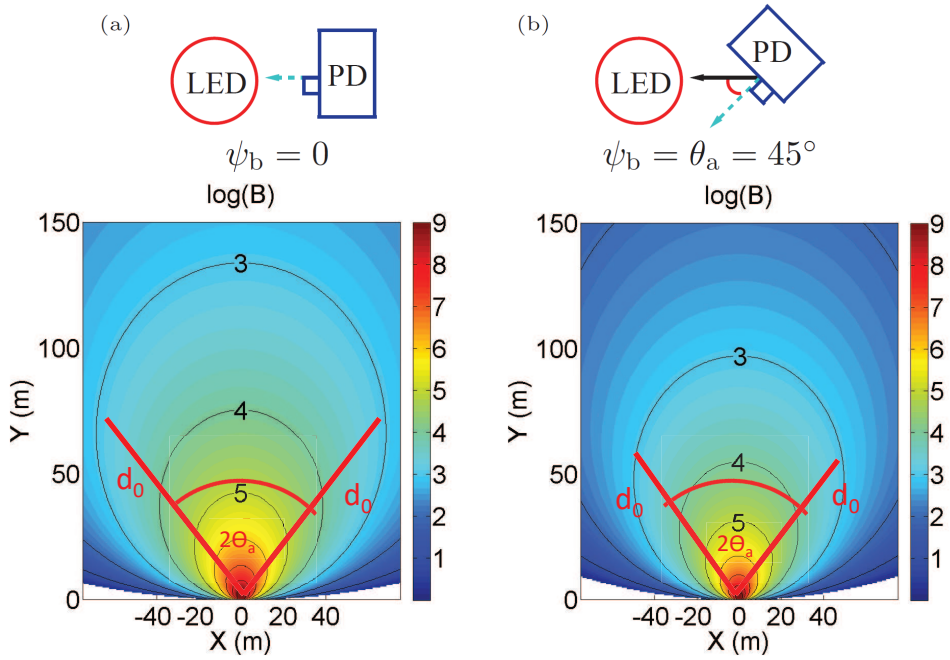

Figure 3.3: Spatial maps of beacon-link bit rates, with diagrams of receiver geometries for (a) perfect receiver alignment ($\psi_b = 0$) and (b) poor receiver alignment ($\psi_b = 45°$). In both cases, θ_a is chosen to be 45°, and the concentrator field of view $\Psi_{c,b}$ is chosen to match θ_a (i.e., $\Psi_{c,b} = \theta_a = 45°$). The LED transmitter is assumed to be at (X,Y)=(0,0) and pointing in the positive Y-direction. The contours represent the logarithm of the bit rate in bits/s. For example, "3" represents $B_b = 1$ kb/s. The calculations assume $P_b = 0.3$ W, $2\theta_a = 90°$, $p_{bg} = 5.8$ μW/nm/cm^2, $\Delta\lambda_b = 100$ nm, $R = 0.6$ A/W, $n = 1.5$, $A_b = 1$ cm^2, $T_{s,b} = T_{n,b} = 0.8$, and BER = 10^{-4}.

kb/s. Other uses of the beacon beam, such as allowing a receiver node to detect the presence of a beacon and perhaps calculate its bearing, might require lower rates. However, while the value of d_0 depends on B_{b0}, ψ_b, and many other parameters, the optimal beamwidth $\Phi_{1/2,b}$ depends only on the maximum allowed pointing error θ_a.

3.1.2 Exploring reasonable beacon rates and ranges

To calculate reasonable ranges and rates, we can use Eq. (2.14) to plot the beacon link rate as a function of the receiver position relative to the LED transmitter. Figure 3.3(a) shows a contour plot of the logarithm of the rates B_{b} over space, assuming that the receiver is pointed perfectly at the beacon transmitter (i.e., $\psi_{\mathrm{b}} = 0$). Here, we choose to assume that the maximum allowed pointing error for the beacon is $\theta_{\mathrm{a}} = 45°$, and the beamwidth is optimized according to Eqs. (3.1) and (3.3) for this θ_a. The beacon transmitter is located at (X,Y) = (0,0) and is pointed in the positive Y-direction. In these calculations, we assume that the link uses a single high-power LED (beacon transmitting power $P_{\mathrm{b}} = 0.3$ W) in bright daytime skylight noise ($p_{\mathrm{bg}} = 5.8\mu$ W/nm/cm^2 [14]). We also assume the receiver is composed of a colored glass filter of passband width $\Delta\lambda_{\mathrm{b}} = 100$ nm and $T_{\mathrm{s,b}} = T_{\mathrm{n,b}} = 0.8$, a silicon p-i-n photodiode of responsivity $R = 0.6$ A/W and active area $A_{\mathrm{b}} = 1$ cm^2, and a glass optical concentrator ($n = 1.5$). Figure 3.3(b) assumes identical parameters, except that here the receiver is assumed to be poorly aligned. Specifically, it is misaligned by an amount equal to the transmitter maximum pointing error ($\psi_{\mathrm{b}} = \theta_{\mathrm{a}} = 45°$). In both figures, we have a chosen receiver (and concentrator) field of view equal to the transmitter maximum pointing error ($\Psi_{\mathrm{c,b}} = \theta_{\mathrm{a}} = 45°$). In practice, field of view varies among receivers, and there is no absolutely optimal field of view; rather, there is a tradeoff between field of view and gain, as seen in Eq. (2.6).

For the purposes of acquisition and feedback control, assuming a minimum beacon rate of $B_{\mathrm{b0}} = 1$ kb/s is reasonable. The calculations in Fig. 3.3(a) show

that for an aligned receiver ($\psi_{\mathrm{b}} = 0$), this required rate is achievable at $d_0 \approx 85$ m. If both the the transmitter and receiver are pointed perfectly (i.e., the receiver lies along the line X = 0, where $\phi_{\mathrm{b}} = 0$), then $B_{\mathrm{b}} = 1$ kb/s is achievable at $d \approx 133$ m. In the case of poor receiver alignment ($\psi_{\mathrm{b}} = \theta_{\mathrm{a}} = 45°$), shown in Fig. 3.3(b), d_0 is roughly 71 m.

In general, the sensitivity of d_0 to the receiver pointing angle ψ_{b} depends on the optical concentrator gain [$g_{\mathrm{b}}(\psi_{\mathrm{b}})$], optical filter [$T_{\mathrm{s,b}}(\psi_{\mathrm{b}})$], and a geometrical factor $\cos(\psi_{\mathrm{b}})$ [see Eqs. (2.5) and (2.15)]. Specifically, d_0 is proportional to the square root of these factors. In the calculations presented in Fig. 3.3, the concentrator gain g is considered constant within its field of view defined by $\psi_{\mathrm{b}} < \Psi_{\mathrm{c,b}} = \theta_{\mathrm{a}}$. We also assume that $T_{\mathrm{s,b}}(\psi_{\mathrm{b}})$ is invariant in ψ_{b} for the beacon link, which is consistent with the behavior of an absorptive colored filter. Thus, in these calculations, the only dependence of d_0 on the receiver misalignment ψ_{b} is the geometrical factor $(\cos\psi_{\mathrm{b}})^{1/2}$. For the two receiver alignments examined here, $[\cos(\psi_{\mathrm{b}})]^{1/2} = 1$ for the well-aligned receiver [Fig. 3.3(a)], and $[\cos(\psi_{\mathrm{b}})]^{1/2} \approx 0.84$ for the poorly aligned case [Fig. 3.3(b)]. Thus the ratio of the values of d_0 in Fig. 3.3(a) and Fig. 3.3(b) is (71 m)/(85 m)≈ 0.84.

3.1.3 Jointly designing the beacon and primary link

In designing a system that utilizes a beacon link to support a more focused link, we require that both links achieve the same range. Although the primary link may achieve useful data rates beyond the range at which the beacon link can achieve

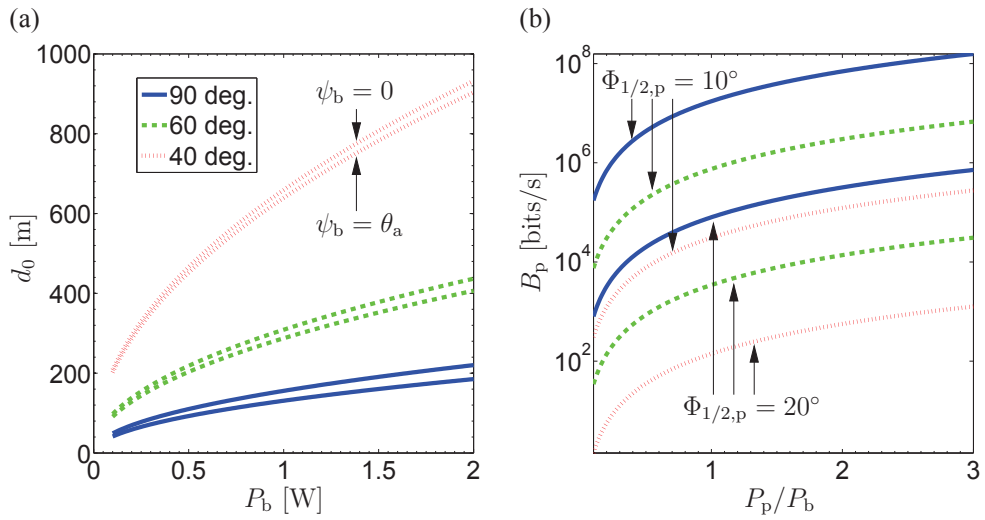

Figure 3.4: (a) Plot of the range d_0 of the beacon link as a function of beacon transmitter power P_b for several values of $2\theta_a$, and for receiver orientations $\psi_b = 0$ and $\psi_b = \theta_a$. The three colors correspond to three values of $2\theta_a$: blue ($2\theta_a = 90°$), green ($2\theta_a = 60°$) and red ($2\theta_a = 40°$). Unless stated otherwise, other parameter values are the same as those used in Fig. 3.3. (b) Plot of data rates B_p of the primary link as a function of P_p/P_b, assuming perfect primary-transmitter pointing ($\phi_p = 0$) and perfect primary-receiver alignment ($\psi_p = 0$). The color-coding used here is the same as in (a). Three curves (one of each pair) correspond to to a narrow beamwidth of $\Phi_{1/2,p} = 10°$, and three curves correspond to $\Phi_{1/2,p} = 20°$. In this plot we assume that the primary link detector area is $A_p = 1$ mm^2 and that the primary link concentrator field-of-view half-angle is 5° for all curves.

$B_b = B_{b0}$, we assume use of the primary link is contingent on successful operation of the beacon link. To meet this requirement of joint operation, it is necessary to consider the design space of the two links together. Figure 3.4 illustrates a representative example of this joint design space, where Fig. 3.4(a) describes the beacon link and Fig. 3.4(b) describes the primary link. The parameters assumed are the same as those of Fig. 3, except for θ_a and the beacon power P_b, parameters that are varied in Fig. 3.4(a).

Figure 3.4(a) defines a pair of curves for d_0 as a function of beacon power P_b, one for $\psi_b = 0$ (well-aligned receiver, greater d_0) and one for $\psi_b = \theta_a$ (misaligned

receiver, shorter d_0); this pair of curves is presented for three values of $2\theta_a$. Thus, for a given power P_b, θ_a, and receiver alignment ψ_b, the plot defines a range d_0. This is the distance from the transmitter at which a data rate of $B_b = 1$ kb/s can be guaranteed within the angular range $-\theta_a \leq \phi_b \leq \theta_a$. Taken alone, Fig. 3.4(a) is a design space only for the beacon link.

The ranges in Fig. 3.4(a) are strongly dependent on $2\theta_a$, but relatively weakly dependent on the receiver alignment. At all three ranges of $2\theta_a$, the $\psi_b = 0$ (well-aligned receiver) case corresponds to only a slightly greater range d_0 than the poorly aligned case of $\psi_b = \theta_a$. This weak dependence on ψ_b is a consequence of the choice of an incident-angle-insensitive filter and concentrator at the beacon receiver, as discussed at the end of the previous subsection. Note that this assumed misalignment θ_a changes for each value of $2\theta_a$ examined; for $2\theta_a = 40°$, the misalignment considered is only $\psi_b = 20°$. Thus for this narrowest allowed angular range examined, the separation between the curves is small compared to that of the other two pairs.

For the beacon parameters chosen in Fig. 3.4(a), and for the calculated "worst-case" ranges d_0, we next examine the data rates for the primary link with the assumption that its alignment is established and maintained by exploiting a beacon link of minimum data rate $B_b = 1$ kb/s. Thus we assume precise pointing for the primary link ($\phi_p = \psi_p = 0$), even though for the primary beamwidths we examine ($10° < \Phi_{1/2,p} < 20°$), the primary link is not nearly as sensitive to pointing errors as typical long-range laser-based systems. To calculate the primary link data rate

B_p, consider the ratio of B_p to B_b using Eq. (2.14). This yields

$$\frac{B_\mathrm{p}}{B_\mathrm{b}} = \left(\frac{T_{\mathrm{s,p}}(\psi_p)}{T_{\mathrm{s,b}}(\psi_b)}\right)^2 \left(\frac{P_\mathrm{p}}{P_\mathrm{b}}\right)^2 \left(\frac{m_\mathrm{p}+1}{m_\mathrm{b}+1}\right)^2 \left(\frac{A_\mathrm{p}}{A_\mathrm{b}}\right)^2 \left[\frac{\cos^{m_\mathrm{p}}(\phi_\mathrm{p})}{\cos^{m_\mathrm{b}}(\phi_\mathrm{b})}\right]^2 \left[\frac{\cos(\psi_\mathrm{p})}{\cos(\psi_\mathrm{b})}\right]^2 \left(\frac{\Delta\lambda_\mathrm{b}}{\Delta\lambda_\mathrm{p}}\right) \left[\frac{\sin(\psi_{\mathrm{b,c}})}{\sin(\psi_{\mathrm{p,c}})}\right]^2. \tag{3.4}$$

In this relation, we have assumed that the primary and beacon links share the same responsivities R, filter properties ($T_\mathrm{n} = T_{\mathrm{n,b}} = T_{\mathrm{n,p}}$), concentrator indices of refraction n, bit-error rates, and ambient noise level p_bg.

Figure 3.4(b) plots B_p as a function of $P_\mathrm{p}/P_\mathrm{b}$. For each of the values of θ_a examined in Fig. 3.4(a), Fig. 3.4(b) plots a pair of curves of primary-link data rates corresponding to two primary-link beamwidths ($\Phi_{1/2,\mathrm{p}} = 10^\circ$ and $\Phi_{1/2,\mathrm{p}} = 20^\circ$), where rates corresponding to intermediate beamwidths lie between the paired curves. A common color-coding scheme is applied to Fig. 3.4(a) and Fig. 3.4(b), so that, for example, the two blue solid-line curves in Fig. 3.4(b) correspond to the case of $2\theta_\mathrm{a} = 90^\circ$ in Fig. 3.4(a).

To calculate reasonable values of B_p, we assume different parameters for the primary link from those of the beacon link, including a smaller detector suited for higher modulation rates ($A_\mathrm{p} = 1$ mm^2 vs. $A_\mathrm{b} = 1$ cm^2) and a narrower bandpass filter ($\Delta\lambda_\mathrm{p} = 30$ nm vs. $\Delta\lambda_\mathrm{b} = 100$ nm) that can more effectively filter ambient noise. The other parameters in Eq. (3.4) assume values determined by Fig. 3.4(a), as the two plots are linked. For example, the transmitter pointing angle ψ_b and receiver field-of-view $\Psi_{\mathrm{b,c}}$ are dictated by the value of $2\theta_\mathrm{a}$ chosen in Fig. 3.4(a) and the previous assumptions that $\psi_\mathrm{b} = \theta_\mathrm{a}$ and $\Psi_{\mathrm{b,c}} = \theta_\mathrm{a}$. The beamwidth parameter

m_b is determined by θ_a and Eq. (3.1). The beacon receiver is assumed to be either perfectly aligned ($\psi_\mathrm{b} = 0$) or misaligned ($\psi_\mathrm{b} = \theta_\mathrm{a}$) depending on the choice assumed in Fig. 3.4(a). We also assume that $T_\mathrm{s,b}(\psi_\mathrm{b}) = T_\mathrm{s,p}(\psi_\mathrm{b}) = 0.8$ and $\Psi_\mathrm{p,c} = 5°$.

As a design example, we see that a beacon transmitter of $2\theta_\mathrm{a} = 90°$ with a range $d_0 = 117$ m can be achieved at a power $P_\mathrm{b} = 0.57$ W (roughly 1–2 high-power LEDs) for a misaligned receiver ($\psi_\mathrm{b} = \theta_\mathrm{a} = 45°$). At this point in the design space, and at this range d_0, Fig. 3.4(b) shows that a primary link of beamwidth $\Phi_{1/2,\mathrm{p}} = 10°$ using 0.24 times the beacon transmitter power ($P_\mathrm{p}/P_\mathrm{b} = 0.24$, $P_\mathrm{p} = 0.14$W) can achieve a data rate of about 1 Mb/s. Note the sensitivity of the data rate to beamwidth, as increasing $\Phi_{1/2,\mathrm{p}}$ to 20° drops B_p to about 4.5 kb/s. To instead increase the primary-link data rate B_p by a factor k_p, one could increase the power P_p by a factor of $k_\mathrm{p}^{1/2}$ [see Eq. (2.14)]. For example, to achieve 10 Mb/s, one could boost the primary-link power such that $P_\mathrm{p}/P_\mathrm{b}$ increases by a factor of [(10 Mb/s)/(1 Mb/s)]$^{1/2}$, so that $P_\mathrm{p}/P_\mathrm{b} = 0.77$ and $P_\mathrm{p} = 0.44$ W.

Maintaining the primary-link bit rate ($B_\mathrm{p} = 1$ Mb/s) but instead extending the range (d_0) of the dual-link system from 117 m to 500 m would require adjustments to both the beacon and primary links. At a beacon power of $P_\mathrm{b} = 0.57$ W, a range of $d_0 = 500$ m could be achieved by narrowing $2\theta_\mathrm{a}$ from 90° to 40°, as seen in Fig. 3.4(a). This adjustment would demand greater pointing precision for the beacon transmitter and receiver. Alternatively, this greater range could be reached by maintaining $2\theta_\mathrm{a} = 90°$ and increasing the power P_b by a factor of [(500m)/(117m)]^2, as computed from Eq. (2.14). This power increase would require $P_\mathrm{b} = 10.4$ W, a significant increase in the number of necessary LEDs. For reference, in the visi-

ble regime this might be on the order of two car headlights in terms of perceived brightness.

To extend the range to 500 m while maintaining the same data rate $B_{\mathrm{p}} = 1$ Mb/s, the primary link would also have to be adjusted. One way to extend the primary-link range is to similarly increase the primary link power by a factor of $[(500\text{ m})/(117\text{ m})]^2$. An alternative is to narrow the beamwidth $\Phi_{1/2,\mathrm{p}}$ [and thus increase the corresponding m_{p}, defined by Eq. (2.2), according to Eq. (2.15)]. Specifically, adjusting the beamwidth from $\Phi_{1/2,\mathrm{p}} = 10^\circ$ ($m_{\mathrm{p}} = 45.28$) to a narrower $\Phi'_{1/2,\mathrm{p}}$(and larger m'_{p}) requires following the relation $m'_{\mathrm{p}} + 1 = k_{\mathrm{b}}^2(m_{\mathrm{p}} + 1)$, where $k_{\mathrm{b}} = (500\text{ m})/(117\text{ m})$ in this example. Thus the beamwidth would be narrowed to $\Phi'_{1/2,\mathrm{p}} = 3^\circ$ ($m'_{\mathrm{p}} = 478.77$) to support a rate of 1 Mb/s at a range of 500m.

We have demonstrated how Fig. 3.4 can be used to find reasonable ranges and rates in a dual-link system given desired power levels, beamwidths, and receiver alignments. The joint consideration of two links, primary and beacon, allows for specialization in the design of each link. Because the beacon link is to be robust, its transmission beam can be wider, its optical concentrator on the receiver has lower gain and a wider field of view, its optical bandpass filter is wider but incident-angle insensitive, and its detector area can be larger (to boost signal strength) due to lower data rates. The primary link is assumed to be more precisely aligned than the beacon link, even though its pointing demands are relaxed considerably relative to those of many laser-based systems. As the more focused, higher-throughput link, its receiver is designed to have a narrower-FOV/high-gain optical concentrator, a narrower interference-based bandpass filter (for enhanced noise rejection), and a smaller

detector compatible with higher data rates. The use of these two complementary links can provide an all-optical LED-based system that is low power, compact, and robust to pointing and tracking error. This robustness may make this system a suitable adjunct to RF technology in short- to medium- range mobile networks. Inexpensive gimbals, such as those available on hobby websites [74], may serve as a means of means of steering transmitters and receivers in the establishment of such optical links.

Chapter 4: Hyperboloidal Mirrors for Situational Awareness

4.1 Introduction

Expanding upon this interest in using all-optical means to address the alignment demands of OW systems, we study the application of an imaging optical system [75,76] to provide optical wireless nodes with location information of neighboring nodes. In this system, a curved mirror and a camera constitute an imaging receiver used to estimate the angle-of-arrival of light-emitting sources (beacons) placed on neighboring nodes. Such a system maintains a 360° field of view in azimuth and more than 90° in elevation without the need for mechanical scanning [60, 61, 77]. Equipped with such a system, a given node can estimate the angular bearings of nearby cooperative nodes, enabling the alignment of OW links. The ranges to nearby nodes can also be estimated with such a system; this could be achieved, for example, by estimating the received signal strength from beacons placed on nearby nodes. This information could be used, for example, to estimate the data rate achievable in an optical link [62]. Applications may include the use of such a system to align OW links between robots [12,13], vehicles [7], and other platforms. And in addition to utilization in the alignment of point-to-point optical links, such a device could be used in LED-based indoor positioning systems [78, 79]. An illustration of how a

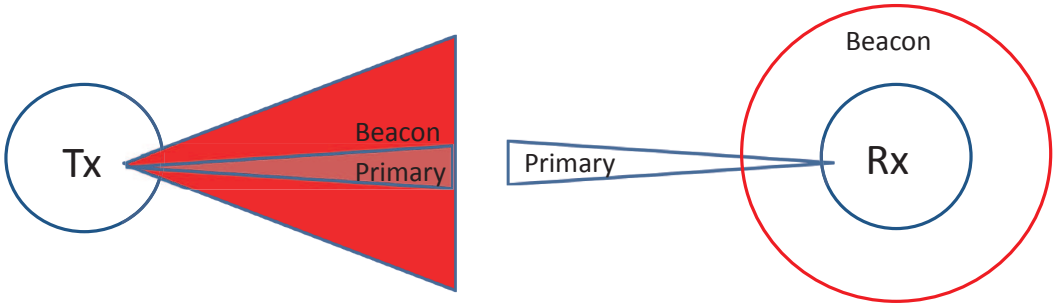

Figure 4.1: In the dual-link systems proposed in Chapter 3, a hyperboloidal mirror system could be used as a beacon receiver. Such a catadioptric system enjoys of 360 degree field of view, thus as acting as a beacon receiver which imposes minimal alignment demands.

hyperboloidal may be used as 360-degree-field-of-view beacon receiver in a dual-link system is shown in Figure 4.1. In using a beacon as a means of aligning links between robots, we assume that the elements being aligned (e.g., primary link transmitters or receivers) have positions that can be well-approximated by the beacons used to mark their positions.

4.2 System Geometry

We propose the use of a rotationally symmetric curved mirror and a camera to act as a means of providing OW links with the omnidirectional awareness necessary for localization of nearby nodes. Systems that combine the use of refractive and reflective components are known as catadioptric systems, and their use to provide expanded fields of view is analyzed in [80]. While a wide field of view can be provided by many types of curved mirrors, we focus specifically on hyperboloidal mirrors. Such mirrors can provide geometrically correct perspective images from a single

viewpoint [80], and have been used in previous research to provide mobile robots with knowledge of obstacles, rolling, and swaying by optical flow analysis [75,81–83]. Within a Cartesian coordinate system (x, y, z), the surface of a hyperboloid mirror is described by

$$\frac{x^2+y^2}{a^2} - \frac{z^2}{b^2} = -1, \; z > 0. \tag{4.1}$$

The parameters a and b parameterize the shape of the mirror. One of the foci of the hyperboloid, denoted F_{m}, lies on the z axis at (0,0,c), where $c = \sqrt{a^2+b^2}$. The point F_{c} at (0,0,-c) is the opposite focal point of the "other half" of the hyperboloid, which is not manifested as a mirror surface. A schematic of this geometry is shown in Figure 4.2, which defines azimuth ϕ and elevation θ.

In this system, a ray originating from a source at point S directed towards F_{m} is reflected by the mirror and directed towards F_{c}, intersecting the image plane at (x, y). To find the value of ϕ that corresponds to the source that appears on the image plane at (x, y), we use the relation [75]

$$\phi = \begin{cases} \tan^{-1}(y/x), & \text{if } x \geq 0 \\ \pi + \tan^{-1}(y/x), & \text{if } x < 0. \end{cases} \tag{4.2}$$

The image plane coordinates of the source can also be used to calculate the elevation angle θ, defined in Figure 4.2. In particular,

$$\theta = \tan^{-1} \frac{(b^2+c^2)\sin\gamma_{\mathrm{c}} - 2bc}{(b^2-c^2)\cos\gamma_{\mathrm{c}}}, \tag{4.3}$$

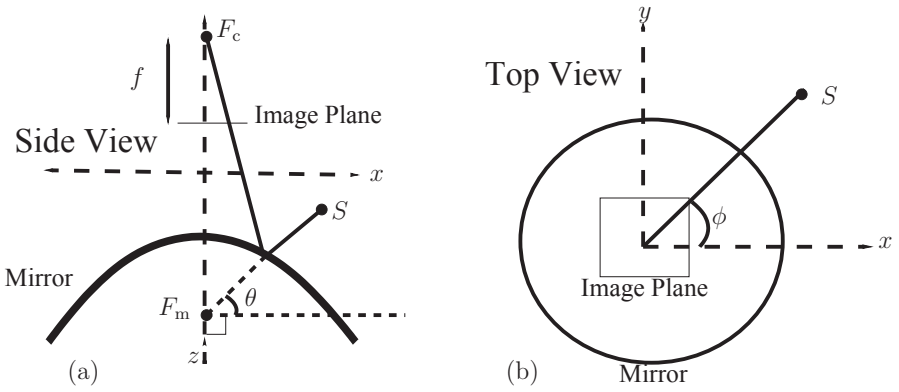

Figure 4.2: The hyperboloidal-mirror-camera system: (a) side view, defining the elevation angle θ, and (b) top view, defining the azimuth angle ϕ. The beacon is located at the point S, while the foci F_m and F_c are located at $(0, 0, c)$ and $(0, 0, -c)$, respectively. The camera center of the camera lense is assumed to be placed at the focus F_c.

where

$$\gamma_c = \tan^{-1} \frac{f}{\sqrt{x^2 + y^2}} \tag{4.4}$$

and the focal length of the camera lens is denoted by f. In Figure 4.3, we plot the dependence of elevation angle θ on the radius $r \equiv \sqrt{x^2 + y^2}$ assuming $a = 23.4125$ mm, $b = 28.095$ mm, and $f = 8$ mm.

4.3 Propagation of Gaussian Error in Angle Estimation

Given the geometry of this catadioptric system, knowledge of the location (x, y) of a feature of interest (e.g., the beacon of a neighboring node) in the image plane can be used to calculate its angular bearing (θ, ϕ). In practice, the methods of estimating x and y are quite varied and the appropriate model for the noise in this estimation depends strongly on the estimation algorithm and the properties

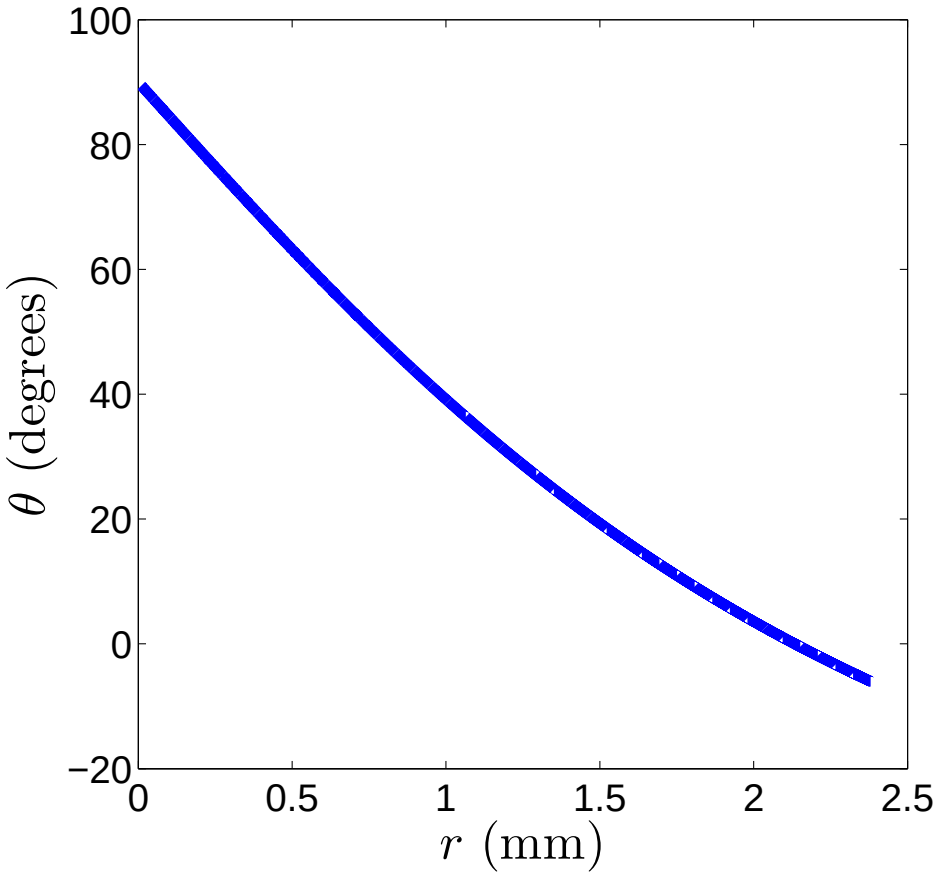

Figure 4.3: Elevation angle θ as a function of r, as given by Eq. (4.3). In this figure, we assume $a = 23.4125$ mm, $b = 28.095$ mm, and $f = 8$ mm, where these values are consistent with the experimental system that presented later in this chapter. An elevation angle of 0° corresponds to a horizontal vector pointing radially outward from F_m (see Figure 4.2), while an elevation angle of 90° corresponds to a vector pointed towards F_c from F_m. The lower limit of observable elevation angle using this particular mirror is $\theta = -16^\circ$.

of the particular hardware implementation. We construct an analytical model for the case of Gaussian noise in the estimation of x and y coordinates, as this noise model is commonly used in computer vision research and may serve as a first-order approximation for other forms of noise [84]. In our model, we assume that measurements of x and y follow independent Gaussian distribution functions $f_X(x)$ and $f_Y(y)$, respectively:

$$f_X(x) = \frac{1}{\sigma\sqrt{2\pi}} e^{\frac{-(x-\mu_{\mathrm{x}})^2}{2\sigma^2}} \tag{4.5}$$

and

$$f_Y(y) = \frac{1}{\sigma\sqrt{2\pi}} e^{\frac{-(y-\mu_{\mathrm{y}})^2}{2\sigma^2}}. \tag{4.6}$$

Here, $(x, y) = (\mu_{\mathrm{x}}, \mu_{\mathrm{y}})$ is defined as the location of the beacon image, while σ is a measure of the noise in the measurement of the beacon image location. To describe the noise in the estimation of ϕ and θ that results from noise in the measurements of x and y, we define random variables Φ and Θ and corresponding probability distributions $f_\Phi(\phi)$ and $f_\Theta(\theta)$. In our model, we assume that $f_{XY}(x, y) = f_X(x) f_Y(y)$.

Eqs. (4.2) and (4.3) show that ϕ can be expressed as a function of $w \equiv y/x$, and θ can be expressed as a function of r. We define random variables W and R with corresponding probability distributions $f_W(w)$ and $f_R(r)$, respectively. We can use the general relation between two random variables [85] to relate W and R to Θ

and Φ:

$$f_{\Phi}(\phi) = f_W(w)\frac{dw}{d\phi} \tag{4.7}$$

and

$$f_{\Theta}(\theta) = f_R(r)\frac{dr}{d\theta}. \tag{4.8}$$

Given Eqs. (4.5) and (4.6), the probability density function $f_W(w)$ is given by [86]:

$$f_W(w) = \frac{b(w)c(w)}{a^3(w)}\frac{1}{\sqrt{2\pi}\sigma^2}\left[2\Phi\left(\frac{a(w)}{b(w)}\right) - 1\right] + \frac{1}{a^2(w)\pi\sigma^2}\exp\left[-\frac{1}{2}\left(\frac{\mu_{\mathrm{x}}^2 + \mu_{\mathrm{y}}^2}{\sigma^2}\right)\right] \tag{4.9}$$

where

$$a(w) = \sqrt{\frac{w^2+1}{\sigma^2}} \tag{4.10}$$

$$b(w) = \frac{\mu_{\mathrm{y}}w + \mu_{\mathrm{x}}}{\sigma^2} \tag{4.11}$$

$$c(w) = \exp\left\{\frac{1}{2}\left[\frac{b^2(w)}{a^2(w)} - \left(\frac{\mu_{\mathrm{x}}^2 + \mu_{\mathrm{y}}^2}{\sigma^2}\right)\right]\right\} \tag{4.12}$$

$$\Phi(w) = \int_{-\infty}^{w}\frac{1}{\sqrt{2\pi}}\exp\left(-\frac{1}{2}u^2\right)\,\mathrm{d}u. \tag{4.13}$$

As ϕ depends exclusively on w, $f_W(w)$ can be used to solve for $f_\Phi(\phi)$:

$$f_\Phi(\phi) = f_W(w) \left| \frac{\mathrm{d}w}{\mathrm{d}\phi} \right|. \tag{4.14}$$

Following Eq. (4.2), $w = y/x$ or $w = \tan(\phi)$ and $\mathrm{d}w/\mathrm{d}\phi = \sec^2(\phi)$. Thus, we can compute $f_\Phi(\phi)$ given values of μ_x, μ_y, and σ.

The estimation of the elevation angle θ can be analyzed similarly. Eqs. (4.3) and (4.4) show that the dependence of the elevation angle on x and y can be expressed as a dependence on r, the radius in the image plane. This allows Eqs. (4.3) and (4.4) to be expressed in terms of only one variable, r, with a corresponding random variable R. Given our model for X and Y, the distribution for R is given by [87]:

$$f_R(r) = \frac{r}{\sigma^2} \exp\left(-\frac{\mu_\mathrm{x}^2 + \mu_\mathrm{y}^2 + r^2}{2\sigma^2} \right) I_0\left(r\frac{\sqrt{\mu_\mathrm{x}^2 + \mu_\mathrm{y}^2}}{\sigma^2} \right) \tag{4.15}$$

where I_0 is the 0th-order modified Bessel function of the first kind.

Thus $f_R(r)$ can be used to solve for the distribution of the elevation angle $f_\Theta(\theta)$ using the relation

$$f_\Theta(\theta) = f_R(r) \left| \frac{\mathrm{d}r}{\mathrm{d}\theta} \right|, \tag{4.16}$$

which can be reexpressed as

$$f_\Theta(\theta) = f_R(r) \left| \frac{\mathrm{d}\theta}{\mathrm{d}r} \right|^{-1}. \tag{4.17}$$

It follows that Eq. (4.15) and differentiation of Eq. (4.3) with respect to r can be

used to solve for $f_\Theta(\theta)$. Differentiation yields:

$$\frac{\mathrm{d}\theta}{\mathrm{d}r} = \frac{\frac{\sqrt{1+\frac{f^2}{r^2}}\left(\frac{\left(b^2+c^2\right)f^3}{\left(1+\frac{f^2}{r^2}\right)^{3/2}r^4}-\frac{\left(b^2+c^2\right)f}{\sqrt{1+\frac{f^2}{r^2}}r^2}\right)}{b^2-c^2} - \frac{f^2\left(-2bc+\frac{\left(b^2+c^2\right)f}{\sqrt{1+\frac{f^2}{r^2}}r}\right)}{(b^2-c^2)\sqrt{1+\frac{f^2}{r^2}}r^3}}{1+\frac{\left(1+\frac{f^2}{r^2}\right)\left(-2bc+\frac{(b^2+c^2)f}{\sqrt{1+\frac{f^2}{r^2}}r}\right)^2}{(b^2-c^2)^2}}. \tag{4.18}$$

While the performance of experimental systems will be impacted by various error sources and depends strongly on the angle-of-arrival estimation algorithm, this analytical understanding of the propagation of Gaussian error may serve as a useful first-order approximation for modeling the cumulative error effects in general.

4.4 Numerical Simulations

To test the accuracy of this solution for $f_\phi(\phi)$, we can simulate randomly "measuring" a large number of pairs of x and y, for a given μ_x, μ_y, σ^2, $f_x(x)$, and $f_y(y)$. Each of the pairs measured corresponds to a value of ϕ via Eq. (4.2). The relative frequencies of these estimated values of θ in a histogram should be consistent with the relative frequencies predicted by $f_\phi(\phi)$.

For one million ($n = 10^6$) simulated pairs, assuming $\mu_x = 0.707$ mm, $\mu_y = 0.707$ mm, $\sigma = 0.05$ mm, the histogram of the corresponding values of ϕ are shown in Figure 4.4. For the assumed values of μ_x, μ_y, and σ, we also plot the frequencies predicted by $f_\phi(\phi)$ with a solid red line. The model $f_\phi(\phi)$ agrees well with the simulated data. We also see that $\sigma_\phi = 8.25°$ for parameters assumed.

Simulating random measurements can be used to verify this solution for $f_\theta(\theta)$,

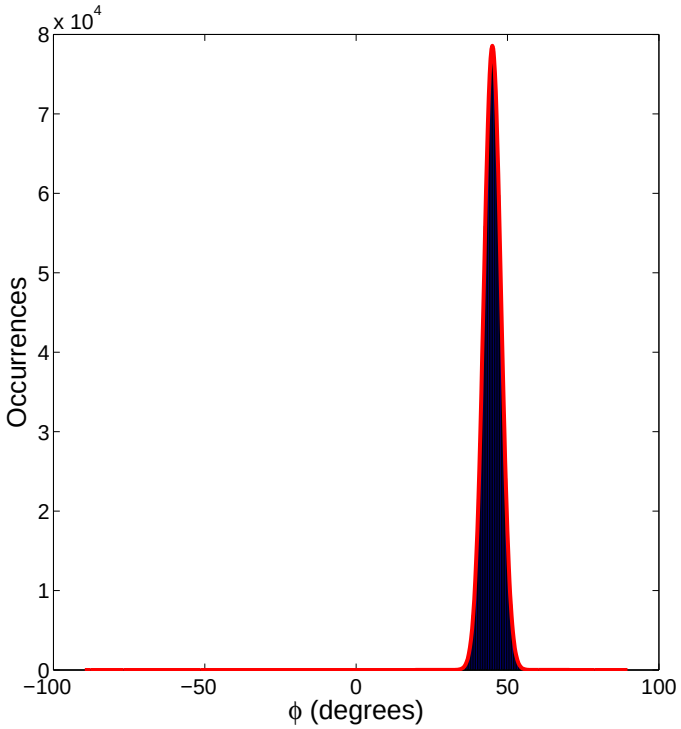

Figure 4.4: Blue bars represent a histogram of ϕ values, $n = 10^6$ values shown here. The red solid line represents theoretical prediction of occurrences according to $f_\phi(\phi)$. Histogram data is based on simulated random "measurements" of X and Y, which assume $\mu_x = \mu_y = 0.707$ mm, $\sigma = 0.05$ mm. Standard deviation in ϕ for these parameter assumptions is $\sigma_\phi = 8.25°$

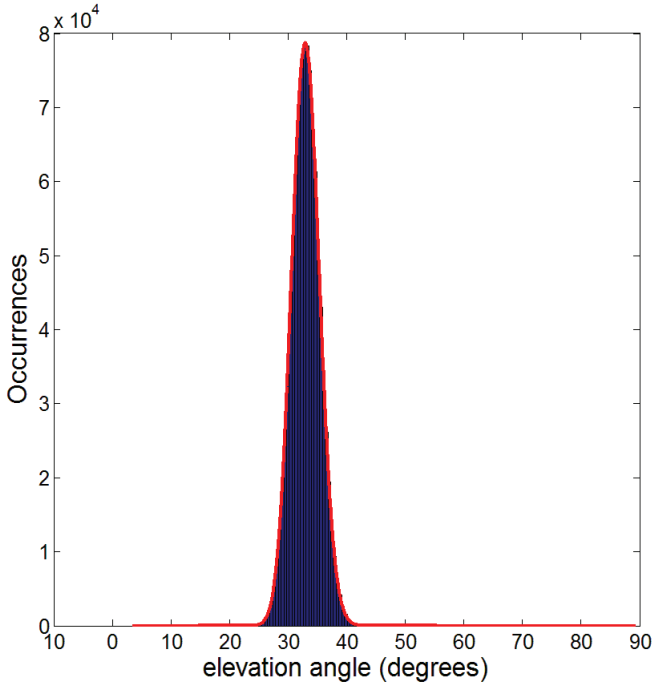

Figure 4.5: Blue bars represent a histogram of θ values, $n = 10^6$ values shown here. The red solid line represents theoretical prediction of occurrences according to $f_\theta(\theta)$. Histogram data is based on simulated random "measurements" of X and Y, which assume $\mu_x = \mu_y = 0.707$ mm, $\sigma = 0.05$ mm. Standard deviation in elevation angle θ is $\sigma_\theta = 6.85°$

as was done in Figure 4.4 for $f_\theta(\theta)$. For one million ($n = 10^6$) simulated pairs, assuming $\mu_x = 0.707$ mm, $\mu_y = 0.707$ mm, and $\sigma = 0.05$ mm, the histogram of the corresponding values of θ are shown in Figure 4.5. For the assumed values of μ_x, μ_y, and σ^2, we also plot the relative frequencies predicted by $f_\theta(\theta)$. We see that for the stated parameter assumptions, $\sigma_\theta = 6.85°$, where σ_θ is the standard deviation of the distribution $f_\theta(\theta)$.

4.5 Relating uncertainty in measuring x and y to uncertainty in angle estimations

With the analysis shown above, we can further explore how uncertainty in the measurements of x and y translate into uncertainty in the estimation of the azimuth and elevation angles. In general, this relation depends on the estimated coordinates (x, y) within the image plane. Given the rotational symmetry of the system, this relation does not depend on the azimuthal angle, i.e., the relations between σ and the uncertainties in the angle estimations depend exclusively on the distance from the center of the image plane, and not at all on ϕ.

In Figure 4.6 we plot the standard deviations of the $f_\phi(\phi)$ as a function σ for several different values of r_μ, which we define as $r_\mu \equiv (\mu_x^2 + \mu_y^2)^{\frac{1}{2}}$. For any given σ, we see that the estimation of ϕ becomes more precise as r_μ increases, i.e., as the elevation angle θ of the source increases. The information in Figure 4.6 can be replotted in a way that normalizes σ with respect to r_μ, as shown in Figure 4.7. When plotted this way, all the data shown in Figure 4.6 overlays each other. In other

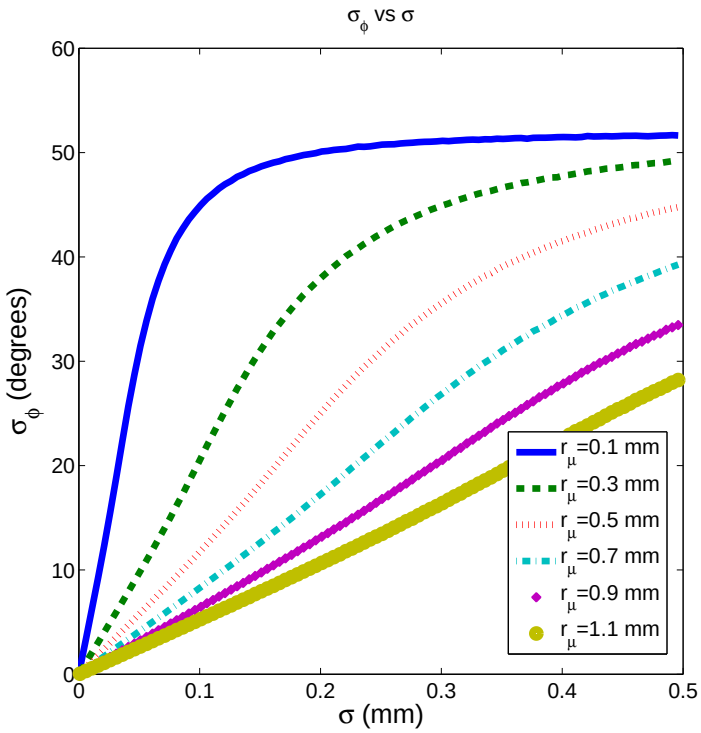

Figure 4.6: σ_ϕ vs. σ, for several values of $r_\mu = \sqrt{\mu_x^2 + \mu_y^2}$. r is the distance of the blob from the center of the image plane. ϕ is the azimuthal angle. σ is the uncertainty in estimation of centroid coordinates in x and y. The curves are plotted for several different radii.

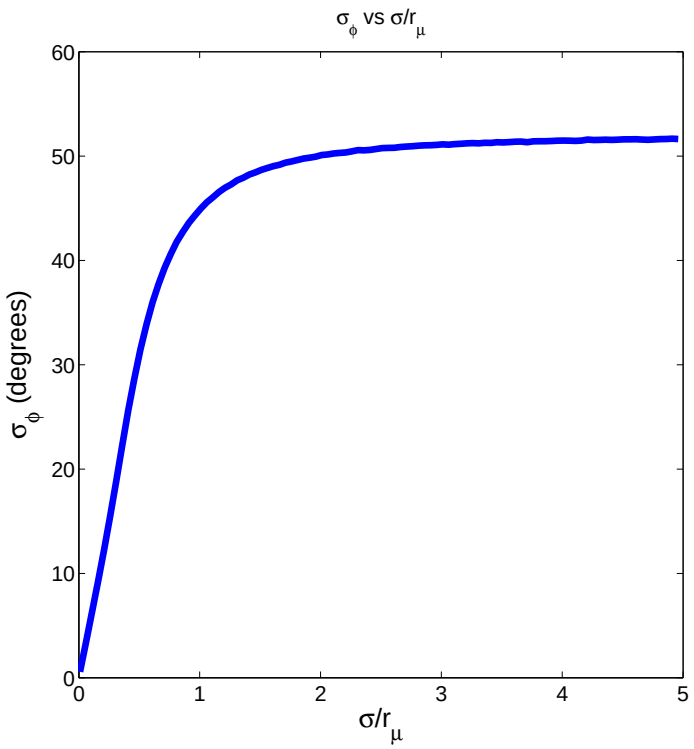

Figure 4.7: σ_ϕ vs. σ/r_μ. ϕ is the azimuthal angle, while σ is the uncertainty of estimation in x and y. σ_ϕ depends only on the ratio of σ to r_μ, the radius of the position of the blob on the image plane.

words, in calculating σ_ϕ, the specific values of σ and r_μ need not be known; only the ratio of σ to r_μ is relevant. In the regime of small σ/r_μ, the curve is approximately linear, with a slope of roughly 60 degrees per unit increase in σ/r_μ.

To see how precise the elevation angle estimation is as a function of σ, in Figure 4.8 we plot σ_θ as a function of σ for the same values of r_μ in Figure 4.6. We see that σ_θ increases with σ, for all values of r_μ, that is, at all elevation angles θ. However, the dependence of σ_θ on r_μ seems to be weaker, and less clear, than that of σ_θ on r_μ; increasing r_μ does not always increase σ_θ.

To further explore this dependence of σ_θ on elevation angle (and r_μ), we plot

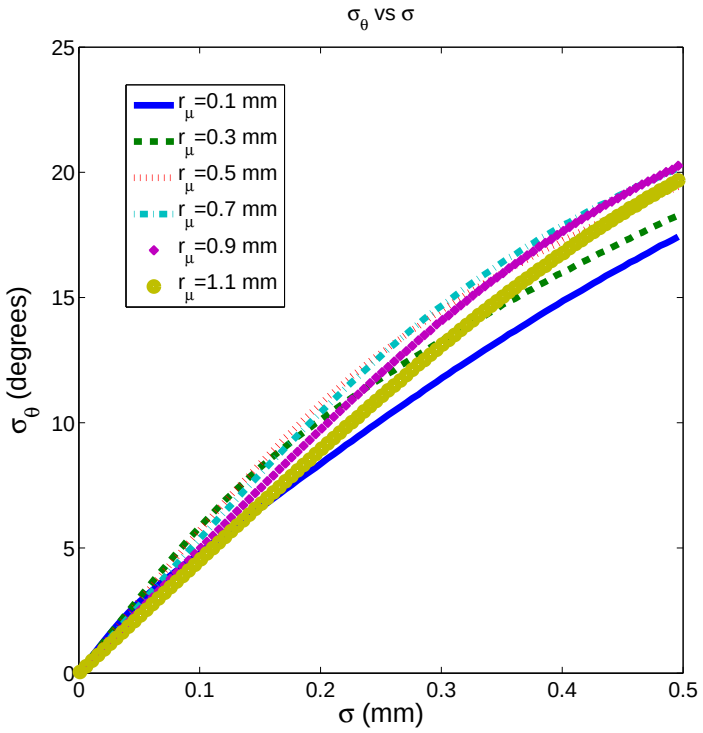

Figure 4.8: σ_θ vs. σ, for several different radii(elevation angles θ). σ is the uncertainty in estimation of x and y coordinates on the image plane.

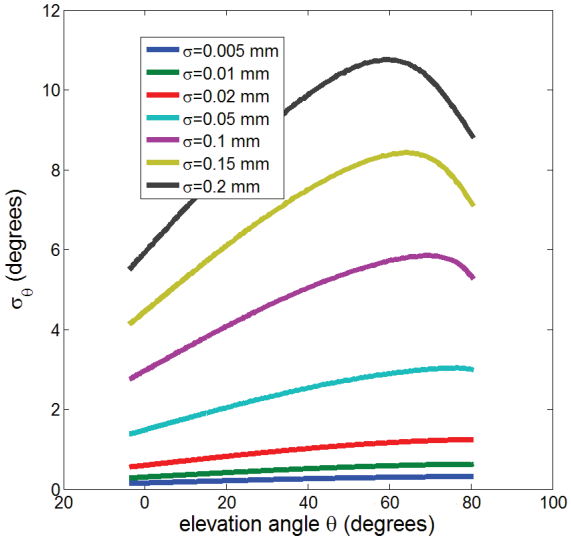

Figure 4.9: σ_θ vs. θ. θ is the elevation angle. The curves are plotted for various values of σ, the uncertainty in estimation of x and y coordinates on the image plane.

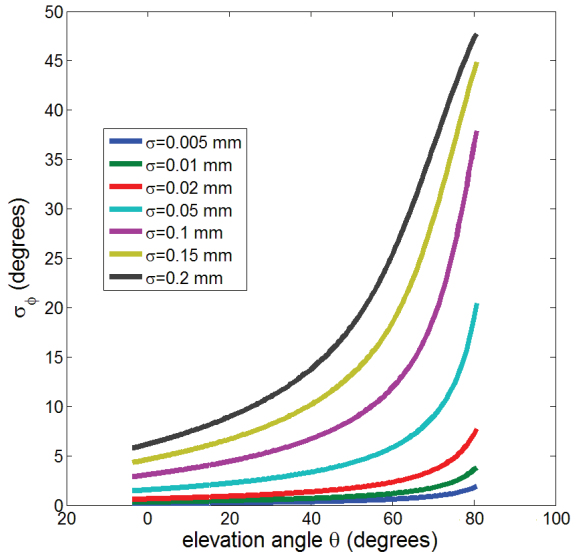

Figure 4.10: σ_ϕ vs. θ. ϕ is the azimuthal angle, while θ is the elevation angle. The curves are plotted for various values of σ, the uncertainty in estimation of x and y coordinates on the image plane.

σ_θ as a function of elevation angle, assuming several different values of σ. This is shown in Figure 4.9. Consistent with the preceding plots and intuition, precision of the angle estimation becomes poor with increasing σ, for any given elevation angle. The concavity of all the curves is downward, and for some values of σ, there seems to be a peak; increasing elevation angle decreases σ_θ in some regimes, and increases it in others.

Figure 4.10 is similar to Figure 4.9 except that it plots σ_ϕ instead of σ_θ. Note as well that the scale of the vertical axis is quite different, with σ_θ becoming very large for low elevation angles at some σ. Estimations of θ seem to be most precise away from the center of the image plane, i.e., at high elevation angles.

4.6 Experimental Implementation

To study the use of this catadioptric system for localization of beacons, we constructed an experimental system, shown in Figure 4.13 with a commercially available hyperboloidal mirror [88] and camera [89]. The camera (Prosilica GC1600H) has 1620x1220 resolution, and its lens has an 8 mm focal length. The base of the mirror is 6 cm in diameter. As shown in Figure 4.13, the distance from the base of the mirror to the top of camera is approximately 16 cm. The relatively compact size of the system allows for mounting onto mobile platforms such as robots, and such catadioptric systems have been studied for robot navigation in [75, 81–83]. To calibrate and align the system, we mounted it onto a gimbal capable of precisely rotating in azimuth and elevation. This camera-mirror system was used to receive signals from a red LED beacon (Luxeon Rebel - Endor Star) [90]. The camera sensor is fitted with a Bayer filter for color image processing. The filter pattern is such that 1/4 of the pixels are dedicated to detecting blue light, 1/4 of the pixels are dedicated to detecting red light, and 1/2 of the pixels are dedicated to detecting green light. Each pixel reports an 8-bit intensity value. Thus the system only observes the beacon using the 1/4 of the total pixels that are designed to detect red light. Despite this reduction in resolution, color-specific detection could be one of many ways to identify multiple beacons simultaneously. All experiments performed using this system were performed in an indoor hallway approximately 70 m in length, with the beacon pointed directly at the mirror. The beacon was at an elevation angle of 0° relative to the mirror. Figure 4.12 shows a side view on the commercially avaiable mirror.

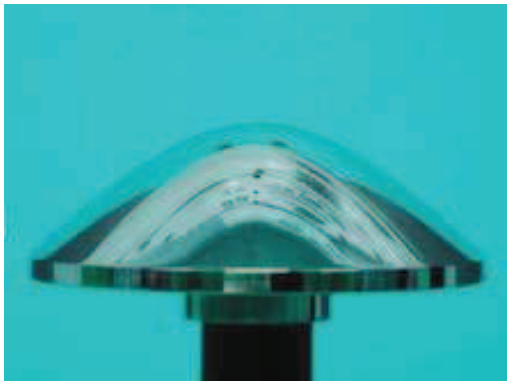

Figure 4.11: Commercial off-the-shelf hyperboloidal mirror used for the beacon system.

Figure 4.12 shows an image captured by the experimental prototype.

While there are many methods for isolating a beacon against the background, in our experiments we implement a simple on-off modulation to drive the LED beacon and subtract consecutive "on" and "off" frames to create a difference image [91]. The difference image is mostly dark, except for the pixels illuminated by the beacon. The LED is driven with a 350 mA current during "on" frames, and no current is applied during the "off" frames.

An example of a difference image is shown in Figure 4.14. In the figure, the spot corresponds to a beacon at approximately 40° azimuth and 0° elevation. The inset shows a mesh plot of the pixels illuminated by the beacon. In our setup, the images captured by the camera and the modulation of the LED were synchronized via coaxial cable, enabling controlled experimental study of angle estimation accuracy. We use this synchronized algorithm to study the behavior of the system in static scenarios, in which neither the beacon nor the catadioptric system is moving. However, in general, asynchronous techniques could be implemented [92]. In moving

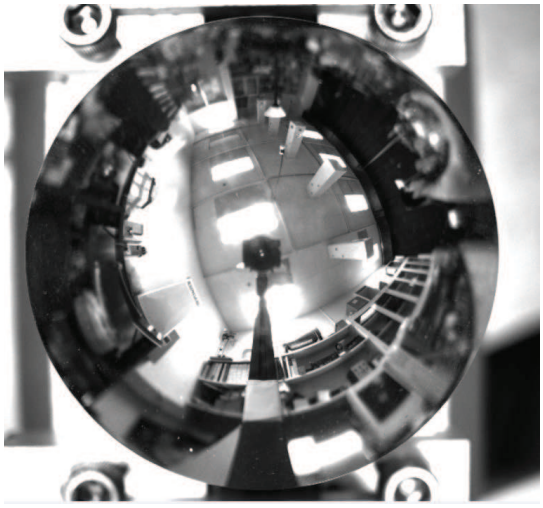

Figure 4.12: Sample image taken with experimental prototype.

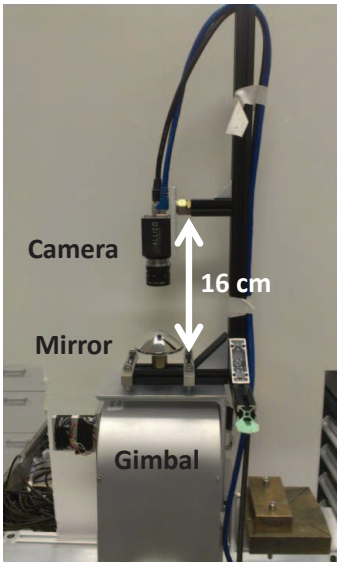

Figure 4.13: Experimental system, mounted onto a gimbal.

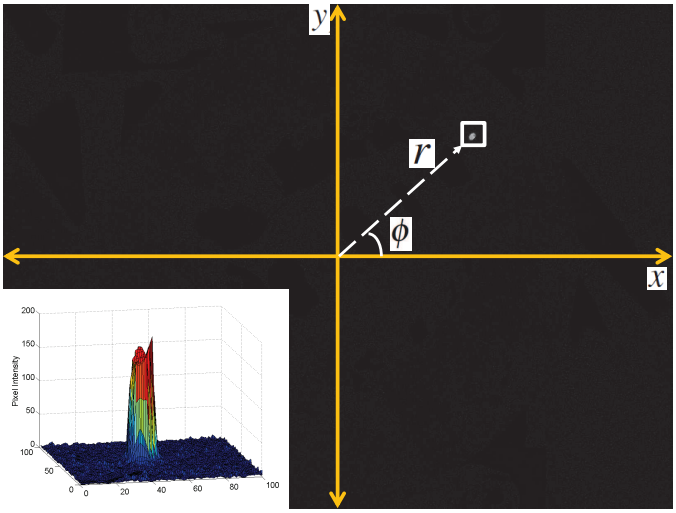

Figure 4.14: Example of experimental difference image, where the beacon image region is enclosed in a white square and the inset is a mesh plot of the beacon image region. The radius r is used to calculate the elevation angle θ, which is approximately 0° in this example. The azimuth angle ϕ is approximately 40°.

scenarios, the differencing processes used to isolate a beacon suffer interference from motion of objects in the field of view, as well as motion of the receiver itself. Some methods for addressing these challenges are median filtering and the use of colored beacons and colored filters to isolate the beacon from the environment. These techniques are discussed in detail in references such as [92]. Other works that have utilized LED beacons for extraction of location information include [79, 91, 93].

4.6.1 Dark Pixels

The system shows frame to frame variations even when observing unchanging scenes. These variations arise due to small response variations before frame differencing. The resulting noise can be observed by examining the "dark pixels" of the difference images, away from the pixel illuminated by the beacon (see Figure 4.14).

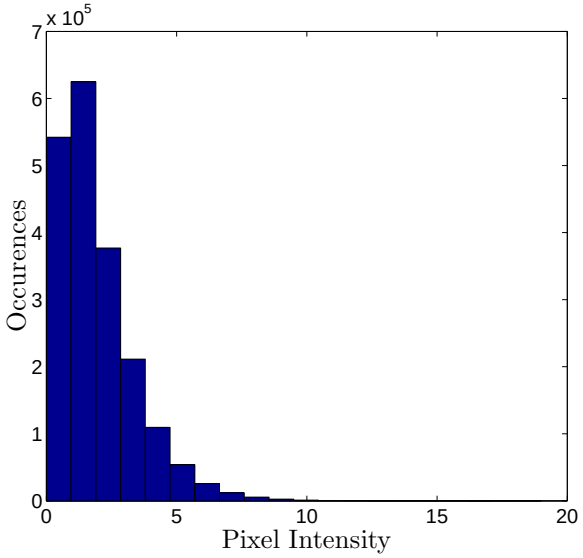

Figure 4.15: Histogram of the dark pixel intensities of the difference image in Figure 4.14. Dark pixels are those not illuminated by the beacon.

Figure 4.15 shows a typical histogram of the pixel intensities of the dark portions of a difference image. The mean of the pixel intensities in the histogram is $\mu_{\mathrm{I}} \approx 1.52$ and the sample standard deviation is $\sigma_{\mathrm{I}} \approx 1.56$. To reduce the effect of this type of noise on the angle estimation, we ignore any pixels below a threshold. The camera detector yields intensity (0 to 255) per pixel, and in data presented in this chapter, the threshold imposed is a pixel intensity of 10.

4.6.2 Angles-of-Arrival Estimation

A reasonable first step in estimating the angle of arrival is the estimation of the location (x, y) of the beacon in the image plane. There are many approaches to estimating (x, y) from the information in a difference image; we take the centroid as our location estimate. This approach has been utilized frequently as a method of estimating the location of an object in an image [94–99] and has the practical

appeal of computational simplicity. For an M-by-N-pixel window of interest, each of the pixels has an x-coordinate x_{ij} and an intensity a_{ij}. Here, $\hat{x}$ (the estimate of the beacon image's x-coordinate) is defined as

$$\hat{x} = \frac{\sum_{j=1}^{M}\sum_{i=1}^{N} a_{ij}x_{ij}}{\sum_{j=1}^{M}\sum_{i=1}^{N} a_{ij}} \tag{4.19}$$

and $\hat{y}$ is defined similarly. Here, M and N define a minimum bounding rectangle that encloses the illuminated region. Using the coordinates of the centroid in the image plane, we then use Eqs. (4.2) and (4.3) to calculate the estimates of the angles of arrival. The algorithm can be summarized as (1) capturing a frame with the LED beacon on, (2) capturing a frame with the LED beacon off, (3) image frame subtraction, (4) applying a threshold, (5) calculating the centroid for pixels within the window of interest, and (6) transforming the centroid into an angle of arrival estimate.

Due to sources of noise in the system, we observe small variations in the estimates of x and y, even when the receiver (mirror and camera) and beacon are fixed in orientation and position. This small variation may be due to a variety of physical effects, including instability in the LED brightness, sensor noise in the camera, etc. We measured these small variations as a function of range from a set of 100 difference images at each range. Here, we define range as the distance between the source at S and the focal point F_{m}. In general, the variation in centroid estimation (both x and y) is non-Gaussian. For each subset of 100 measurements

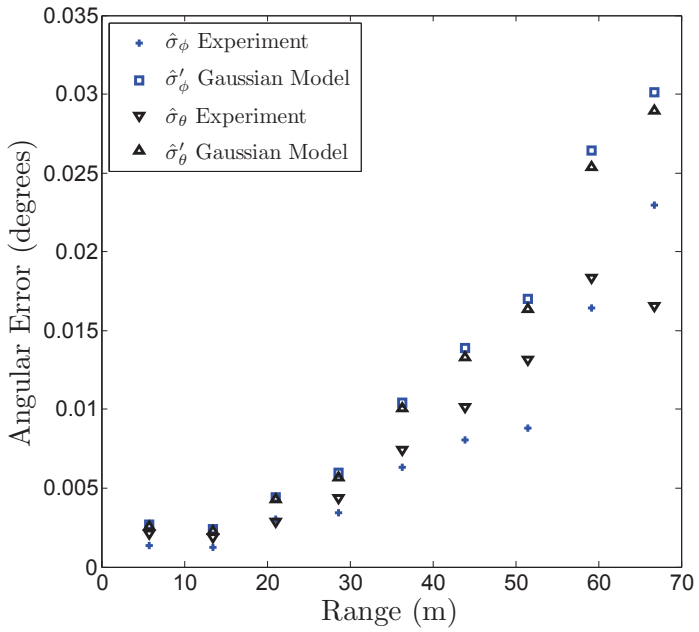

Figure 4.16: Sample standard deviations in angle-of-arrival estimates of azimuth ϕ and elevation θ as a function of range. Here, $\hat{\sigma}_\phi$ and $\hat{\sigma}_\theta$ are sample standard deviations that result directly from the estimation algorithm; $\hat{\sigma}'_\phi$ and $\hat{\sigma}'_\theta$ are standard deviations in angle estimates that result from taking the distribution of measurements in the image plane to be a circular Gaussian with variance $\sigma \equiv \sqrt{\hat{\sigma}_{\mathrm{x}}^2 + \hat{\sigma}_{\mathrm{y}}^2}$.

taken at each range, we define sample standard deviations in the centroid estimation in x and y as $\hat{\sigma}_{\mathrm{x}}$ and $\hat{\sigma}_{\mathrm{y}}$, respectively. This variation in centroid estimation results in variation in angle estimates, as the location in the image plane is related to the angles-of-arrival via Eqs. (4.2) and (4.3). We define the resulting sample standard deviations in estimation of ϕ and θ as $\hat{\sigma}_{\phi}$ and $\hat{\sigma}_{\theta}$, respectively. We plot $\hat{\sigma}_{\phi}$ and $\hat{\sigma}_{\theta}$ as a function of range in Figure 4.16. As the signal becomes weaker with range, the variation in the estimates of the angle of arrival generally increases.

To examine the fidelity of the Gaussian error model developed in Section 3 in modeling the error characterized by $\hat{\sigma}_{\mathrm{x}}$ and $\hat{\sigma}_{\mathrm{y}}$, we define $\sigma \equiv \sqrt{\hat{\sigma}_{\mathrm{x}}^2 + \hat{\sigma}_{\mathrm{y}}^2}$. If we take the variation in centroid estimation to be a circular Gaussian with a variance defined as σ^2, we can define distributions in angular estimates $f_{\Theta}(\theta)$ and $f_{\Phi}(\phi)$ using the model developed in Section 3. The variation in these distributions can be characterized by their standard deviations $\hat{\sigma}'_{\theta}$ and $\hat{\sigma}'_{\phi}$. These values of $\hat{\sigma}'_{\theta}$ and $\hat{\sigma}'_{\phi}$ are plotted as a function of range in Figure 4.16. Although the variation in centroid estimates in the image plane is typically non-Gaussian, we observe that modeling this noise as a circular Gaussian yields reasonable results as a first-order approximation of the consequent error in angular estimation.

The discrete nature of the camera sensor's sampling grid introduces errors into the system. This form of sampling error depends on the size of the pixels relative to that of the beacon image spot size, as well as the beacon image location on the sensor plane. In general, decreasing the size of the pixels (and sampling the beacon image more densely) decreases this error. However, there are potential advantages to increasing the pixel size.

Larger pixel sizes may improve performance by enhancing the system's sensitivity [100] to low light levels. This may enhance the system's ability to detect beacons that are either dim or far away. In other scenarios, the strength of the beacon signal may not be an issue but there may be a need for generating many angle-of-arrival estimations at a high rate, perhaps to track a fast-moving beacon. In such cases, increasing pixel size may reduce the number of pixels that need to be readout, potentially increasing the speed (angle-of-arrival estimations per second) of the system. For instance, this can be implemented dynamically in many cameras in a process known as binning, in which pixels are effectively merged together to create a larger pixel, allowing for a faster readout and increased frames per second. In our experimental measurements, the rate of angle-estimation was only about 10 Hz, limited by the framerate of the camera.

To explore the errors as a function of the pixel size, we approximate the model the beacon image spot as a circular Gaussian distribution:

$$g(x,y) = \exp[-\frac{(x-\mu_{gx})^2}{2\sigma_g^2} - \frac{(y-\mu_{gy})^2}{2\sigma_g^2}]. \tag{4.20}$$

Let $\hat{x}$ and $\hat{y}$ be the centroid estimate. In each of the two components, the estimation can be reduced to a centroid estimation of a one-dimensional Gaussian function. Thus we choose to consider the errors observed in the centroiding of a one-dimensional Gaussian that is sampled at points spaced distances T apart, along the x-dimension, without any loss of generality.

The centroid of $g(x)$ is located at $x = \mu_{gx}$. To examine the behavior of

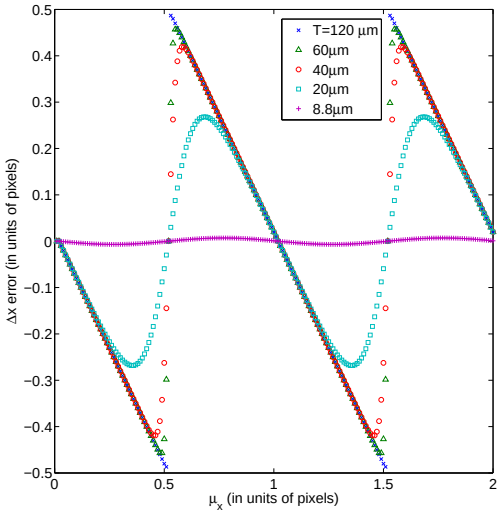

Figure 4.17: Error in centroid estimation Δx as a function of μ_{gx} along 1D sampling grid, over two pixel periods ($\mu_{gx} = 0$ to $\mu_{gx} = 2T$). The five curves correspond to three different ratios of σ_g to T, or beacon image size to pixel period. For all curves, $\sigma_g = 5\mu$m.

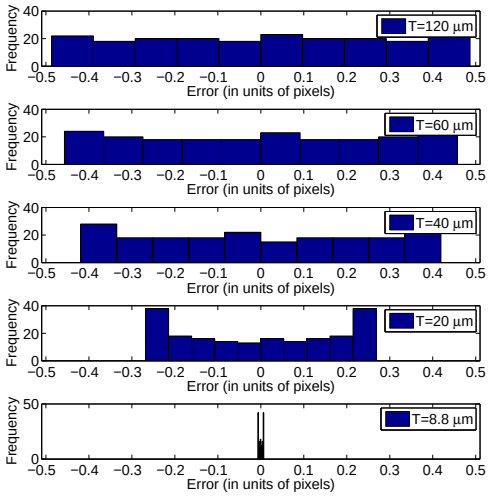

Figure 4.18: Histograms of the errors Δx seen in Figure 4.17, for each of the five curves. With decreasing pixel size T, the distribution of Δx becomes narrower and less uniform. For all curves, $\sigma_g = 5\mu$m.

the centroiding algorithm, we observe the errors while varying the location of the Gaussian intensity distribution ($\mu_g x$). The errors in estimation ($\Delta x \equiv \hat{x} - \mu_{gx}$) due to the discrete sampling are shown in Figure 4.17, which examines the error in centroid estimation as a function of μ_{gx} for five different pixel sizes T (120 μm, 60 μm, 40 μm, 20 μm, and 8.8 μm). For pixels that are large compared to the variance($\sigma_g << T$), the error approaches that of a sawtooth function. As the pixels decrease in size, the error function becomes sinusoidal and shrinks in amplitude. In all five curves, we assume that $\sigma_g = 5\mu$m, which is reasonable representation of the size of beacon images seen empirically. In practice, the size and shape of the blob varies significantly with parameters such as beacon power, range, elevation angle, and others. We note that the appropriate choice for σ_g depends strongly on focusing, LED beacon power, range and other system parameters.

To examine the error distribution, we plot histograms in Figure 4.18 of the five sets of errors shown in Figure 4.17. The total number of data points for each of the five histograms is 200. As the pixels become large compared to the beacon image, the errors become large, and the distribution approaches uniformity. As pixels become small, the distribution deviates from uniformity and becomes tail-heavy, while worst-case errors become smaller, i.e., the region of support of the error is shrinking. The reduction in errors with shrinking pixel size becomes particularly pronounced as the pixel size approaches the beacon image size. This is reflected in the large disparity in worst-case error observed between the histograms for $T = 20\mu$m and $T = 8.8\mu$m in Figure 4.18. In the experimental implementation, we use only 1/4 of the sensor's pixels (the red pixels). Thus the sampling period is actually twice the pixel cell size,

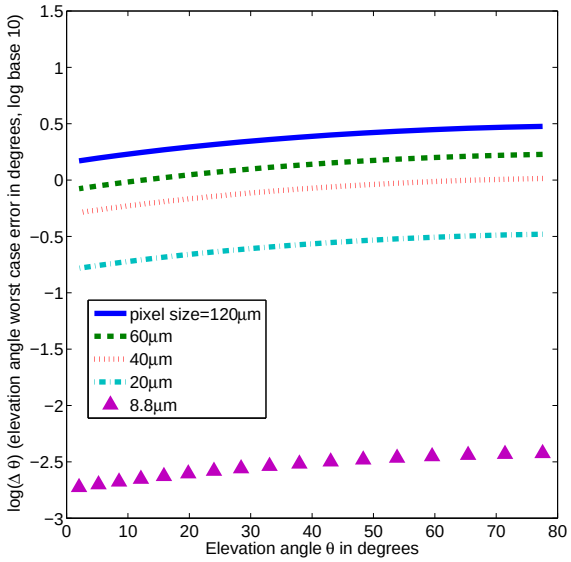

Figure 4.19: "Worst-case" errors in elevation angle (θ) estimation, for each of the five pixel sizes seen in Figure 4.17. Errors are plotted as a function of elevation angle. All curves assume system parameters consistent with the experimental prototype, except for pixel size. The 8.8 μm pixel period is consistent with experimental implementation.

which can be approximated by the $T = 8.8\mu$m case in these calculations.

The effect of these errors on estimation of θ and ϕ varies as a function of θ and ϕ, i.e., the beacon image's location on the image plane. For any given azimuth angle ϕ, estimation of ϕ and θ are more sensitive to Cartesian errors Δx and Δy for smaller values of θ, or, equivalently, for smaller values of r. And for any given elevation angle θ, the effect of Cartesian errors is greatest along certain axes in the image plane. A given error Δx induces the greatest error in estimation of θ along the x-axis, while a given error Δy induces the greatest error in estimation of θ along the y-axis. Similarly, a given error Δx has the greatest effect on estimation of ϕ along the y-axis, while a given error Δy has the greatest effect on estimation of ϕ

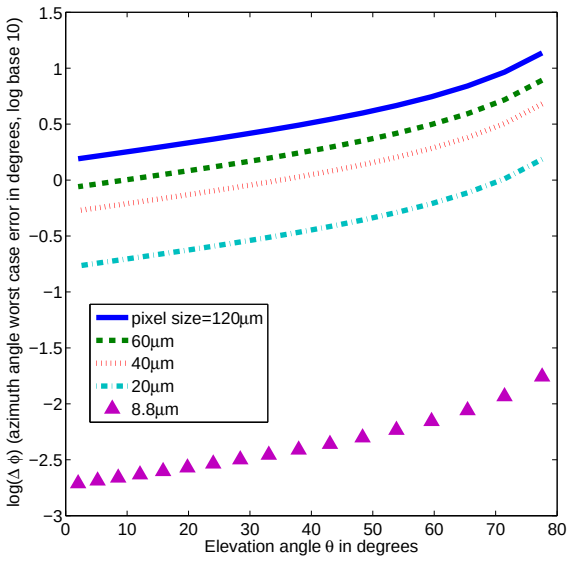

Figure 4.20: "Worst-case" errors in azimuth (ϕ) estimation, for each of the five pixel sizes seen in Figure 4.17. Errors are plotted as a function of elevation angle. All curves assume system parameters consistent with the experimental prototype, except for pixel size. The 8.8 μm pixel size is consistent with experimental implementation.

along the x-axis.

To calculate the worst possible error on angle-of-arrival estimation, we assume the largest errors seen in Figure 4.17 for each pixel size, and calculate the consequent errors in angle estimation along the axes where ϕ and θ estimation are most sensitive. Figures 4.19 and 4.20 explore these worst-case errors as a function of θ. In each of Figures 4.19 and 4.20, the five curves correspond to the five pixel sizes T.

The improvement in estimation with shrinking pixel size becomes most dramatic once the pixel size approaches the width σ of the beacon image. Decreasing the pixel size from 20 μm to 8.8 μm decreases errors in both angle estimations of roughly two orders of magnitude, while the disparity between the errors for $T = 120\mu$m and $T = 60\mu$m is much smaller. Both of these figures assume system parameters consistent with our experimental prototype, with the exception of pixel size.

At zero degrees elevation angle, both angle estimations $\hat{\theta}$ and $\hat{\phi}$ experience approximately the same level of error, for the same pixel size. At low elevation angles, the effective pixel density becomes smaller, and errors due to the finite sampling of the pixels increase. Thus, both angle estimations' error increases with decreasing elevation angle, though the effect of elevation angle on the azimuth estimation is much stronger.

Using our experimental setup, we observe these errors by rotating the gimbal over small angular ranges. In Figure 4.21, we plot the azimuth angle estimated by our system, and and compare it to the known gimbal azimuth angle as the gimbal is swept through one and a half pixel periods. Each point is an average over 100 independent estimates. The initial estimated azimuth angle at zero degrees is taken

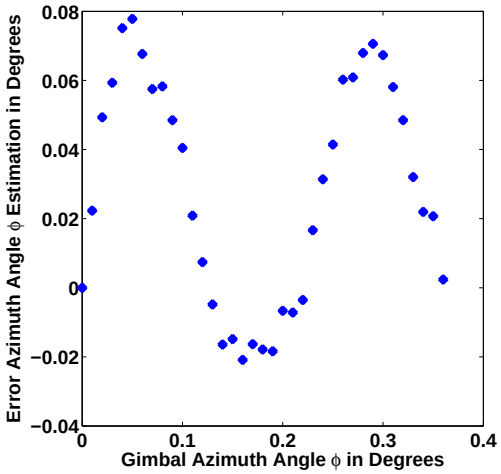

Figure 4.21: Empirical data of azimuth angle estimation, rotating the gimbal through about 1.5 pixel periods. Given the pixel density, the period of the oscillations is 0.23 degrees. Each point is an average over 100 independent estimates.

to be zero error for calibration. We see that the error shows periodic behavior, with a period of 0.23 degrees in azimuth. This period of 0.23 degrees is consistent with the pixel cell size and the location in the image plane.

In the extreme case in which pixels are much bigger than the illuminated area, the error created by granularity of pixels can be understood using numerical simulations that consider the illuminated area to be a point on the image plane. In this big-pixel regime, the system is only able to determine which pixel is illuminated by the beacon, but has no knowledge of the beacon image location within the illuminated pixel. To better understand this uncertainty in estimation of the image location within the Cartesian plane and how it maps to uncertainty in the estimation of azimuth and elevation angles, we conduct simulated random trials in which the beacon image is placed randomly within a pixel, where the pixel size and

other system parameters are consistent with our experimental implementation.

Figure 4.22 plots the error in angle estimations that results from this uncertainty of placement within an illuminated pixel. In this plot, we assume an elevation angle of zero degrees, and the center of the pixel that sits on the location of the image that corresponds to the elevation angle is considered zero error. Each data point represents the error produced by random placement of the beacon image within this pixel. More precisely, it is the mean error of 1000 simulated random placements of the beacon image within the pixel. The pixel is considered big relative to the beacon image, and thus the beacon image is considered to be a point. Naturally, this mean error increases linearly with the side length of the pixel squares, for both azimuth and elevation error. The errors between azimuth and elevation error are nearly equal.

This mean error varies with the elevation angle. We observe this in Figure 4.23, which plots this means error for both azimuth and elevation as a function of elevation angle. We assume a pixel size of 8.8 μm here. At zero degrees elevation angle, the two type of error are nearly equal, consistent with Figure 4.22. As the elevation angle decreases, the mean error increases. This increase is nearly linear for elevation angle, while the increase is nonlinear for azimuth and becomes much larger at very negative elevation angles.

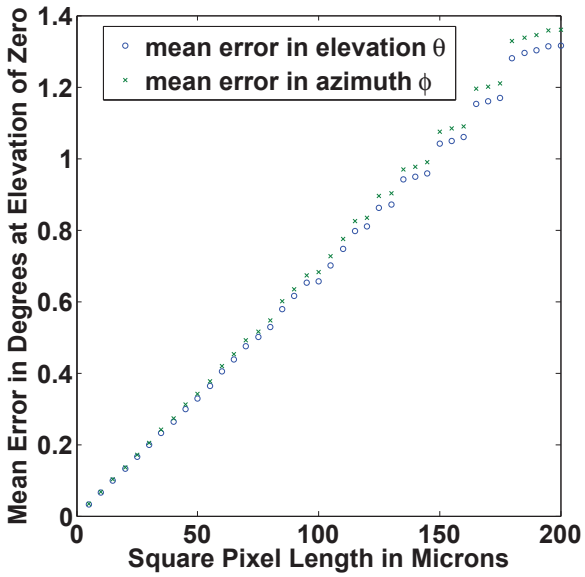

Figure 4.22: Each data point represents the error produced by random placement of the beacon image within this pixel. More precisely, it is the mean error of 1000 simulated random placements of the beacon image within the pixel. The pixel is considered big relative to the beacon image, and thus the beacon image is considered to be a point. This mean error increases linearly with the side length of the pixel squares, for both azimuth and elevation error. The errors between azimuth and elevation error are nearly equal.

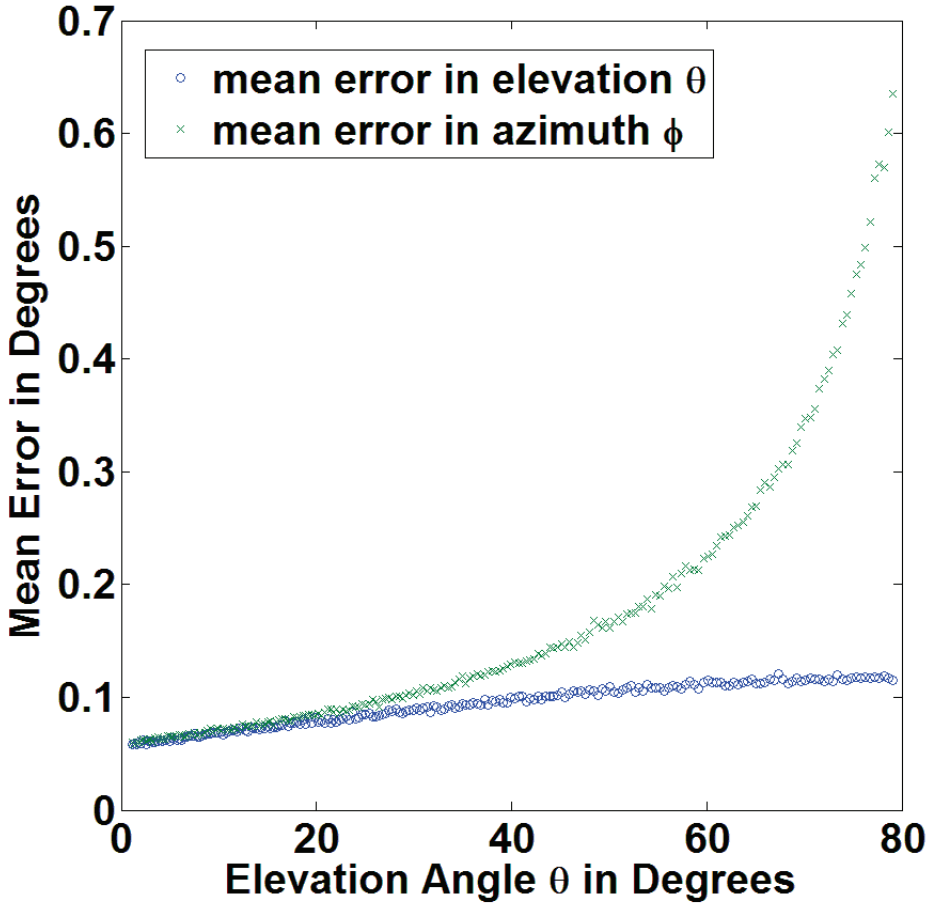

Figure 4.23: Mean error for both azimuth and elevation as a function of elevation angle. We assume a pixel size of 8.8 μm here. At zero degrees elevation angle, the two type of error are nearly equal, consistent with Figure 4.22. As the elevation angle decreases, the mean error increases. This increase is nearly linear for elevation angle, while the increase is nonlinear for azimuth and becomes much larger at very negative elevation angles.

4.6.3 Range Estimation

Given our particular implementation, a simple and straightforward method for range estimation utilizes the observed signal strength. We define the signal strength as the sum of the reported pixel values of the pixels within the centroiding window of the difference image. In general, the signal strength monotonically decreases with range, and this one-to-one mapping from signal strength to range allows for the possibility of using signal strength observations to create range estimates. The exact dependence of signal strength on range is a function of many parameters, including elevation angle and system hardware parameters (e.g., camera sensitivity and camera exposure time, beacon brightness, etc.). However, if all these parameters are known, then the dependence of signal strength on range can be specified, and range can be estimated using signal strength observations. Such signal-strength-based techniques could also be used to estimate range to individual nodes; in such an application scenario, signal strength would be estimated for each beacon, as opposed to observing only the aggregate signal power.

The precision of such a range estimation method is limited by the repeatability of signal strength observations (which is dictated by factors such as pixel noise and the stability of the beacon) and the sensitivity of signal strength to range. To assess the precision of using signal strength as a proxy for range, we recorded observations of signal strength at nine different ranges r_i, in increments of 7.6 m. At the ith range, the receiver (mirror and camera) and beacon were fixed in orientation and position, and 100 observations of signal strength were taken. The ith subset of measurements

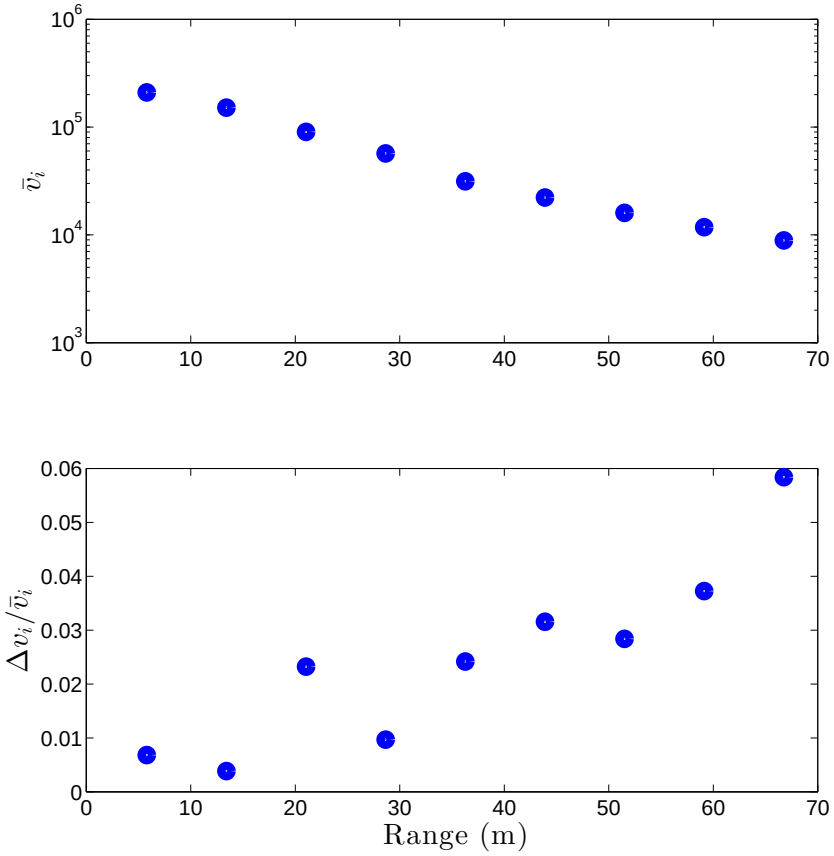

Figure 4.24: The top inset is a semilog plot of the mean signal strength $\bar{v}_i$ as a function of range. The bottom inset plots $\Delta v_i/\bar{v}_i$ as a function of range.

yields a mean $\bar{v}_i$ and sample standard deviation Δv_i. This data is shown in Figure 4.24, in which the top inset plots the mean signal strength $\bar{v}_i$ against range r_i. The sensitivity of signal strength to range, which we define as the steepness of the curve underlying the data points, generally decreases with range. The bottom portion of the figure describes the repeatability of the measurements. The ratio of sample standard deviation to measured mean signal strength ($\Delta v_i/\bar{v}_i$) grows from less than 1% at short ranges to about 5.5% at the longest range examined (67 m).

In a calibrated system, the dependence of signal strength on range is known empirically, and thus range can be estimated using subsequent measurements of signal strength. At any particular range, the precision of estimation is a function of the variability (Δv_i) in the observations of signal strength and the sensitivity of range to signal strength. To estimate the precision achievable using this estimation method, we estimate the sensitivity of signal strength at a range r_i as:

$$s_i = \left(\left| \frac{\bar{v}_i - \bar{v}_{i-1}}{r_i - r_{i-1}} \right| + \left| \frac{\bar{v}_i - \bar{v}_{i+1}}{r_i - r_{i+1}} \right| \right) /2 \tag{4.21}$$

This is an empirical approximation of the steepness of the curve underlying the points sampled at ranges r_i. Combined with the stability estimated by Δv_i, we construct an estimate of the precision in range estimation given by: $\Delta r_i \equiv \Delta v_i / s_i$. The values of Δr_i evaluated using our system are shown below in Table 1, for the middle seven of the nine ranges studied. The sensitivity s_i is undefined for the first ($i = 1$) and last ($i = 9$) ranges studied.

The table shows that this simple method for ranging can yield sub-meter

precision except at the longest range when the signal is weakest. At long ranges, the relative flatness (small s_i) of the curve increases the uncertainty Δr_i of the range estimation beyond one meter. Ranging precision on the order of one meter would be useful in many applications, including optical wireless communications. For instance, a transmitter could use this information to determine the minimum required transmission power needed to achieve a desired data rate. In general, the ranging precision achievable with this catadioptric system is dependent on the particular hardware parameters of the system, and the estimation could be improved with more sophisticated algorithms. For example, multi-frame integration could enhance SNR and potentially lead to an enhanced range estimation.

Range r_i (m)	13.4	21.0	28.7	36.3	43.9	51.5	59.1
Uncertainty Δr_i (m)	0.27	0.09	0.20	0.31	0.45	0.64	1.10

Table 4.1: Uncertainty in range estimations.

Chapter 5: Self-aligning LED-based Link Prototype

As discussed in the previous chapter, a hyperboloidal mirror together with a camera can be used as a means of localizing an LED beacon. In the context of optical wireless communications, such localization may provide the information necessary for alignment between two nodes. We constructed a prototype of a self-aligning link, for proof-of-principle demonstration.

The prototype constructed consists of two links, one beacon and one primary, that exist between two nodes, Node A and Node B. Node A consists of a beacon receiver, the catadioptric hyperboloidal-mirror-camera system discussed in the previous chapter. The catadioptric system, along with the primary link transmitter, are mounted onto a gimbal. Node B consists of a receiver for the primary link, co-located with the beacon transmitter. In this configuration, Node A is able to detect beacon light emitted from Node B, estimate the bearing (azimuth and elevation), and use control of the gimbal to align the primary link transmitter to towards Node B and its primary link receiver. In principle, this self-alignment is demonstrable with node B as well, though we do not demonstrate self-alignment with node B.

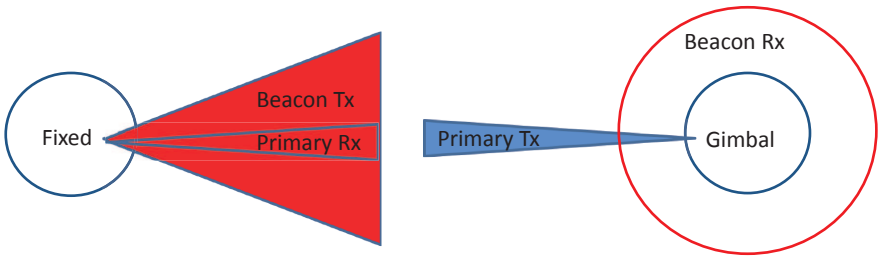

Figure 5.1: Node B consists of a beacon transmitter and primary link receiver, and is pictured on the left. Node A consists of the hyperboloidal beacon receiver, and the primary link transmitter pictured on the right. Node A is mounted on a gimbal, and able to point in the direction Node B, which is fixed in orientation and assumed to be pre-aligned.

5.1 Unsynchronized detection of the flashing LED beacon

In this system, the beacon transmitter consists of a flashing LED. As discussed in the previous chapter, such a beacon can be detected by the catadioptric system, allowing the catadioptric system to estimate the relative azimuth and elevation bearing of the beacon. There are many possible methods of implementing this. In any method, it is necessary to localize the image of the beacon within the image generated by the catadioptric system. In general, this localization could be achieved by image recognition of the beacon; this could be achieved relatively straightforward, if, for example, the beacon can be assumed to be of a color distinct from the rest of the image.

In the method for beacon localization presented in the previous chapter, the beacon is flashed at some fixed frequency. The beacon receiver (mirror-camera system) performs subtraction of consecutive images to construct a difference image, in which all features of the image besides the beacon are "subtracted out" and only

the pixels illuminated by the beacon are seen as illuminated in the difference image. As presented in the previous chapter, this method requires synchronization between the camera's sampling of images and the beacon's flashing, and this synchronization was achieved by means of a coaxial cable. However, image subtraction is a viable method even in the absence of synchronization, so long as the sampling rate of images is sufficiently fast relative to the rate of beacon flashing.

In the method demonstrated in this prototype, we perform unsynchronized frame subtraction, obviating the need for synchronization via coaxial cable. The timing of this method is illustrated in Figure 5.2. In general, the method could involve the capture of many frames; five frames are illustrated here for simplicity. In the absence of synchronization, the alignment of frames A, B, C, D, and E relative to the LED modulation is arbitrary, but sampling at a sufficient rate guarantees that at least some of the frames observe images in which the LED's state is opposite its state when frame A is captured. In the illustration, frame A is captured when the LED is on, while frames D and E are capture when the LED is off [92]. Thus, calculating the absolute differences between frame A and each of the other frames yields at least some difference images which isolate the beacon from the rest of the scene.

In practice, the camera frames are not instantaneous, and nor are LED's transitions between on and off states. These complications can weaken or obscure the beacon signal as observed in the difference images. Complicating practical operation further, any changes in the scene during the grabbing of frames A through E yield interference in the beacon localization process. This type of interference can arise

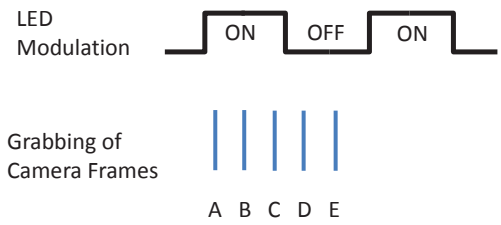

Figure 5.2: In the absence of synchronization, the alignment of frames A, B, C, D, and E relative to the LED modulation is arbitrary, but sampling at a sufficient rate guarantees that at least some of the frames observe images in which the LED's state is opposite its state when frame A is captured. In the illustration, frame A is captured when the LED is on, while frames D and E are captured when the LED is off [92]. This algorithm is used to create a difference image which localizes the beacon image in the camera sensor plane. This localization allows for estimation of azimuth and elevation angles of the beacon in the real world. This angle estimation can be used in the alignment of an optical link.

from any changes in the scene, including motion of the mirror camera system itself, or motion of objects being observed.

This interference can complicate the beacon localization process. There exist many potential methods to address this interference and reduce its effect on the beacon localization process. For example, one could sample over many frames - if the beacon is fixed relative to the camera, it will stay at a fixed location in the difference images, while most interference is less likely be so repeatable.

The beacon image can often be differentiated from interference by its shape. In general, the shape of the beacon image varies with parameters that including distance, elevation, and others. However, the beacon image is in general circular, to an approximation. Thus, circle detection is one possible means of helping to localize the beacon and distinguish it from interference. It is convenient to use circle detection packages available in software such as LabView [101]. In our prototype, the

beacon is driven at 2.5 Hz, and the camera captures frames at 25 fps. Thus, examining five camera frames at once guarantees the an absolute difference combination, i.e., $|A-B|, |A-C|, |A-D|$, or $|A-E|$, that isolates the beacon in the image. Here, $|X-Y|$ is used to denote the absolute difference image generated when one subtracts the pixel values in image X from their corresponding pixel values in image Y. This isolation of the beacon image allows for estimation of θ and ϕ, the bearings of the beacon. These estimations are used to control the gimbal upon which the mirror is mounted. The gimbal has a pointing precision of 0.002° in both azimuth and elevation.

5.2 Primary Link Hardware

In the prototype constructed, the hyperboloidal mirror is used as a means of detecting a beacon and estimating the bearing of the primary link receiver that is co-located with the beacon. Using this estimation of bearing, the primary link transmitter mounted on the gimbal in the contructed prototype points towards the primary link receiver. A general schematic of the primary link is shown in Figure 5.3.

The light emitted from the LED transmitter is focused by an aspheric lens with focal length The transmitter is pictured in Figure 5.4. The layout of the transmitter circuit boards is shown in Figure 5.5. The green LED [102] has a center wavelength of 530nm, a typical turn on voltage of 2.90 V, and a typical current of 350 mA. At that voltage, it outputs 102 lumens. The aspheric lens used to focus the LED

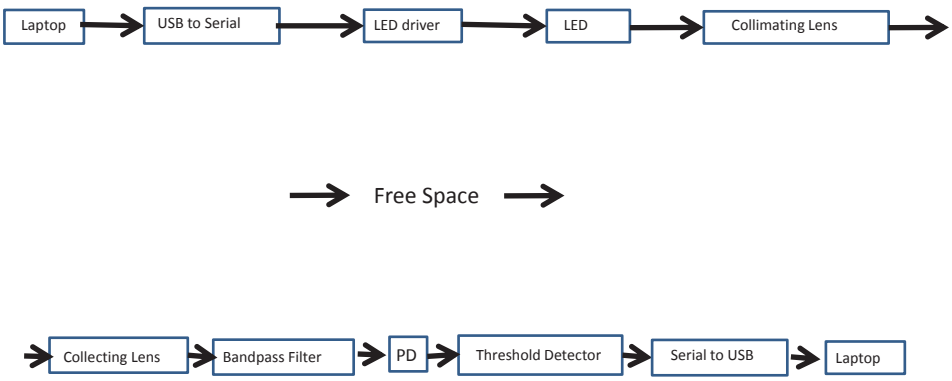

Figure 5.3: A schematic of the primary link, implemented as a serial link.

emission is 2 inches in diameter and has a focal length of 49 mm.

The information transmitted is in the format of a serial link, and the transmitted information originates in the Labview program used to control the link. The serial data is converted from the RS-232 voltage format to voltage levels between 0V and 5V using a Maxim MAX205 [103]. The circuit diagram for the MAX205 is shown in Figure 5.7. Converted into the 0V to 5V format, the data is used to control the LED driver board. The LED transmitter mounted onto the gimbal is shown in Figure 5.6.

The receiver uses a 2-inch lens with focal length of 60 mm to focus the received LED light onto a an amplified photodetector (Thorlabs PDA36A). The front end of the receiver is pictured in Figure 5.8. The detector is fitted with a bandpass optical filter (Thorlabs FB500-40) that has a full-width half maximum optical bandwidth of 40 nm, with the bandpass extending from a wavelength of about 500 nm to 540 nm. The photodiode itself has an active area of 13 mm^2. Figure 5.9 shows the strength of the photodetector's response as a function of alignment angle, when no focusing

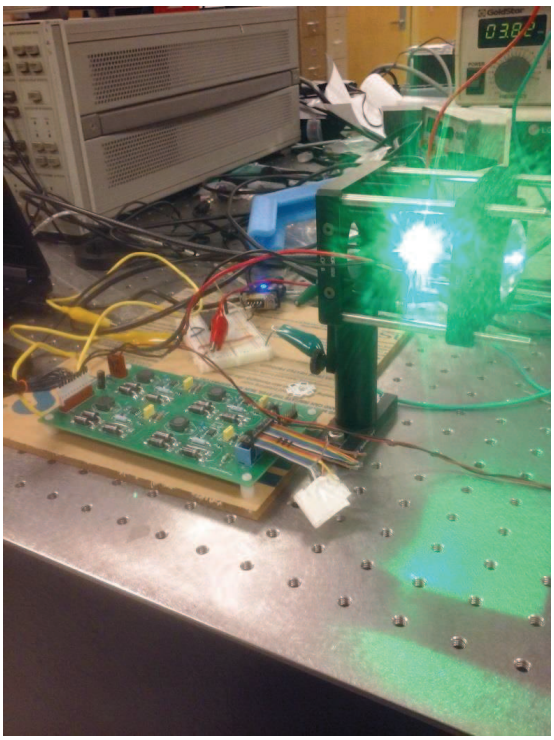

Figure 5.4: The green LED transmitter, being driven by the PCB board pictured. The PCB board was provided by colleagues at the U.S. Army Research Laboratory.

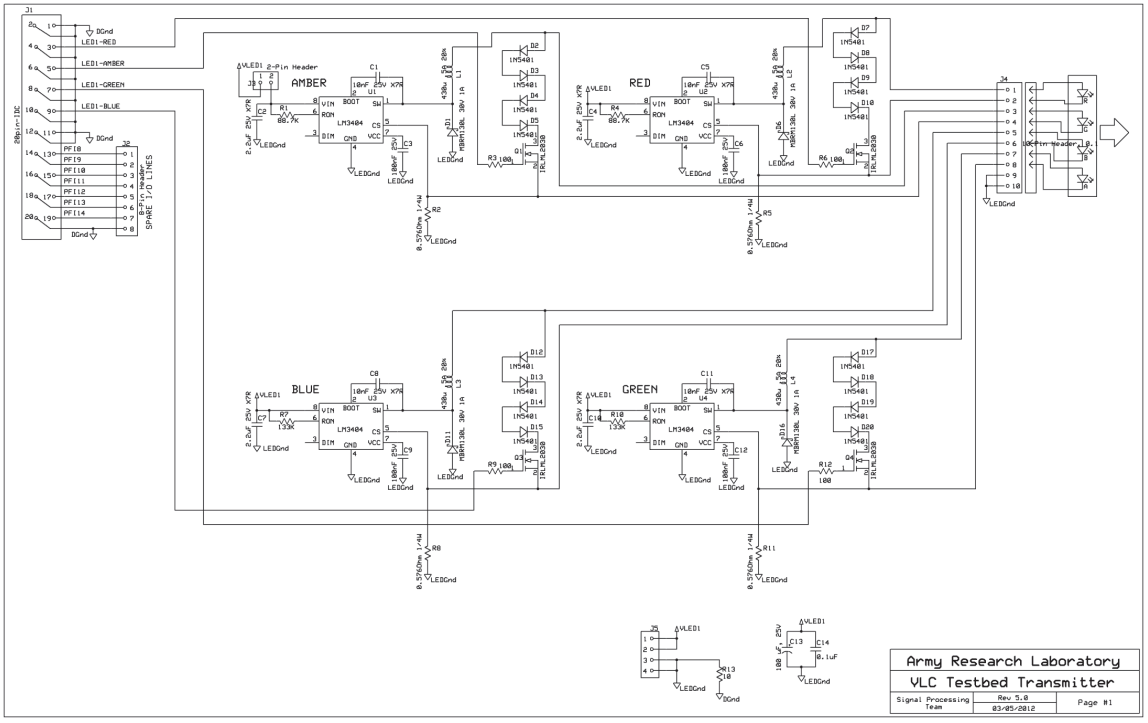

Figure 5.5: Layout of PCB board used to drive the LEDs. The PCB board was built by colleagues at the U.S. Army Research Laboratory.

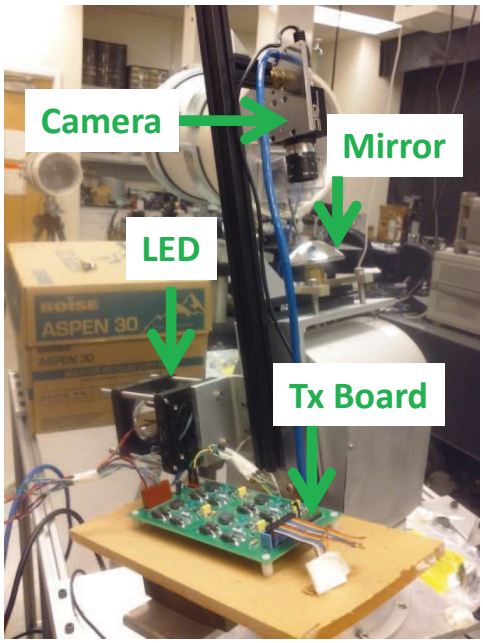

Figure 5.6: The transmitter mounted onto the gimbal, along with the mirror and camera.

lens is used. The use of a lens to focus the light achieves higher gain, but narrows the field of the view. Figure 5.10 plots the normalized power received vs the receiver alignment angle.

The output from the amplified photodetector is fed into a comparator that acts as a thresholding device. One input of the comparator is the output of the photodiode while the other is a variable voltage. The variable voltage is controlled by a potentiometer; it is necessary to adjust for variation in the signal strength as a function of range, alignment, and other factors. The voltage outputs of the comparator are restricted to 0V values. This comparator output is fed into a MAX205 chip which converts the voltage levels back into RS-232 levels. The signal can then be processed as in Labview.

The sensitivity of the system performance to transmitter alignment depends

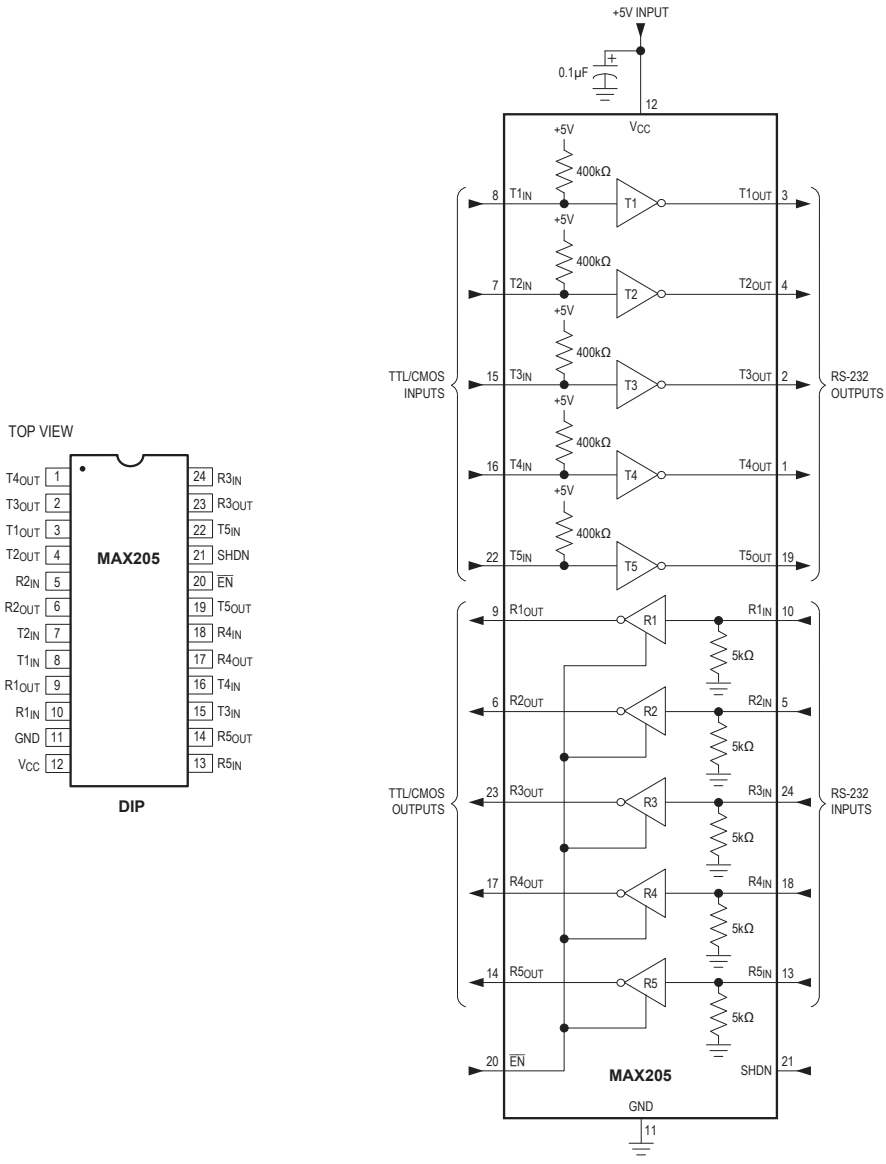

Figure 5.7: Schematic of the layout of the Maxim Max205 devices used to convert from RS-232 voltages to TTL/CMOS voltages (0V to 5V).

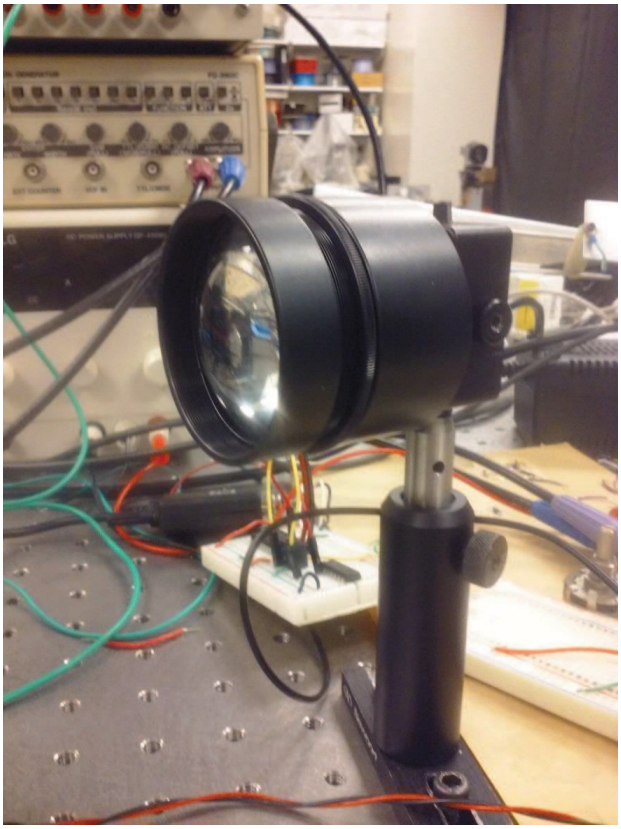

Figure 5.8: The receiver, pictured here, includes a 2" diameter lens used for focusing the light onto the photodetector. Included but not shown is an inteference-based filter used to filter out ambient light, Thorlabs FB500-40.

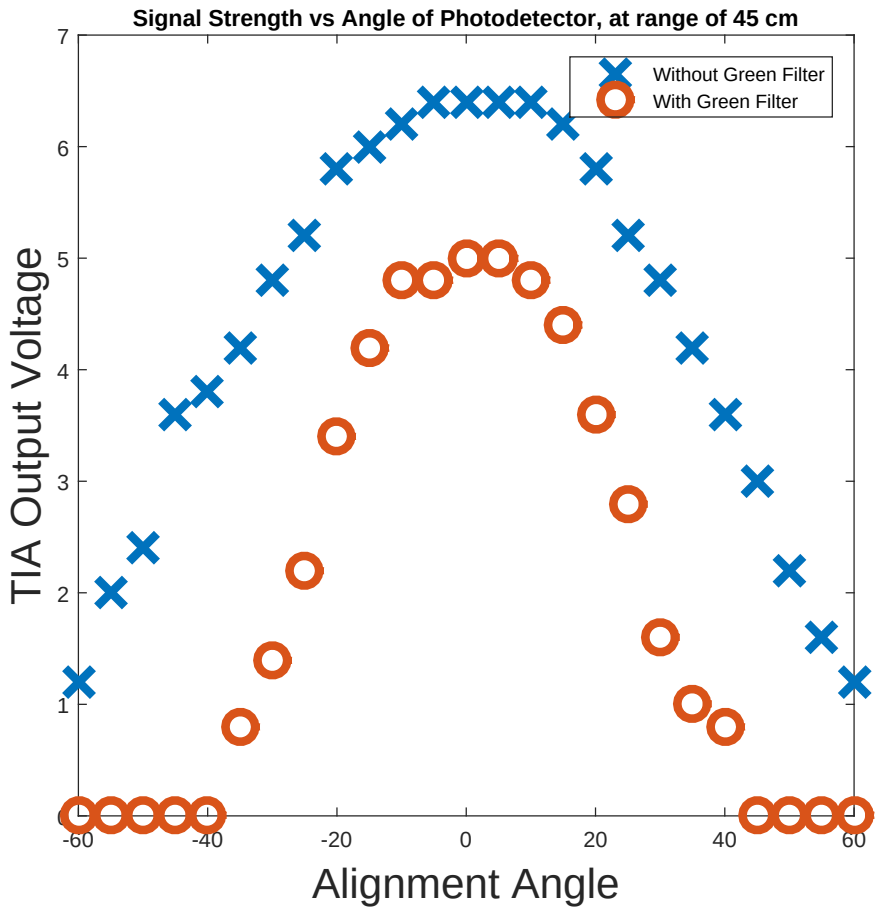

Figure 5.9: Normalized power received from the photodiode (Thorlabs PDA36A) as a function of alignment angle, without a focusing lens, with and without the green filter (Thorlabs FB500-40). A green LED is placed 45 cm away from the photodetector, and the photodetector is mounted on a rotating stage. An "alignment angle" of zero degrees corresponds to being pointed directly at the green LED. The voltages excited by the green LED are lower with the filter on, at all angles. The field of view is smaller with the filter on.

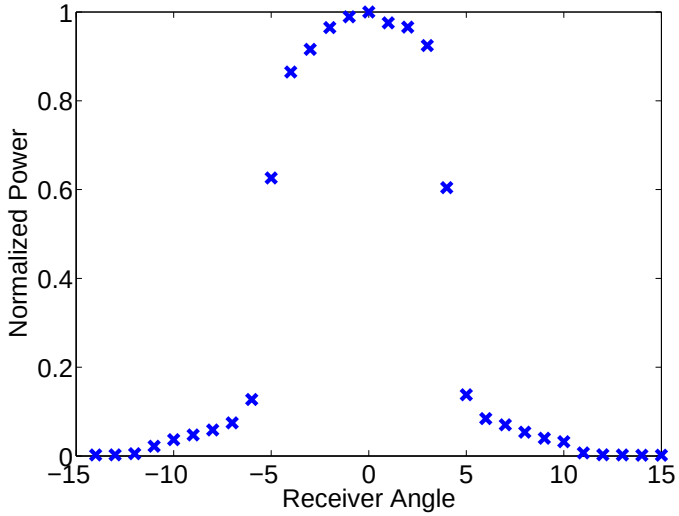

Figure 5.10: Normalized power received by the receiver as a function of the receiver alignment angle.

on the design of optical components used to shape the radiation pattern of the LED. Using an aspheric lens, the transmitted beam can be focused, as shown in Figure 5.12. In this figure, we plot power received vs. the transmitter pointing angle. The radiation pattern is approximately 2° wide, falling sharply off beyond that. Directing the LED towards a surface such as a wall shows an image of a square, consistent with the LED chip itself. At approximately 68 meters in range between the transmitter and receiver, 10,000 serial packets were sent to the receiver. Figure 5.13 plots the fraction of 10,000 packets received vs the transmitter alignment angle.

Figure 5.11: Experimental demonstration of the primary link. The green LED emission is focused by an aspheric lens, and the emitted light is received by a receiver. Here, the receiver is approximately 35m away from the transmitter.

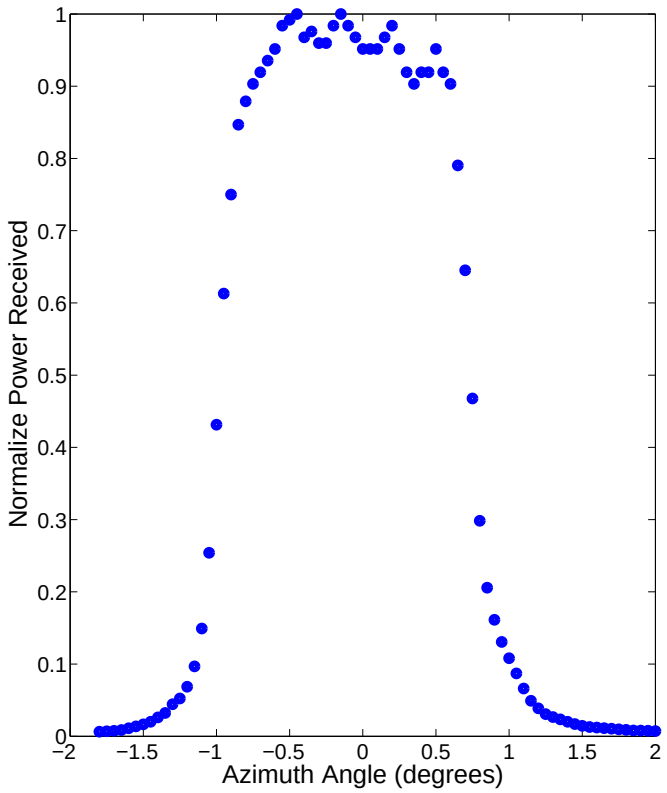

Figure 5.12: Normalized power received by the receiver, as a function of transmitter pointing angle (azimuth angle). This angular dependence is a function of the lens used to focus the LED light. With the aspheric lens ($f = 49$mm) approximately a focal length away from the LED itself, the transmitted beam is nearly collimated, with the divergence described by this figure.

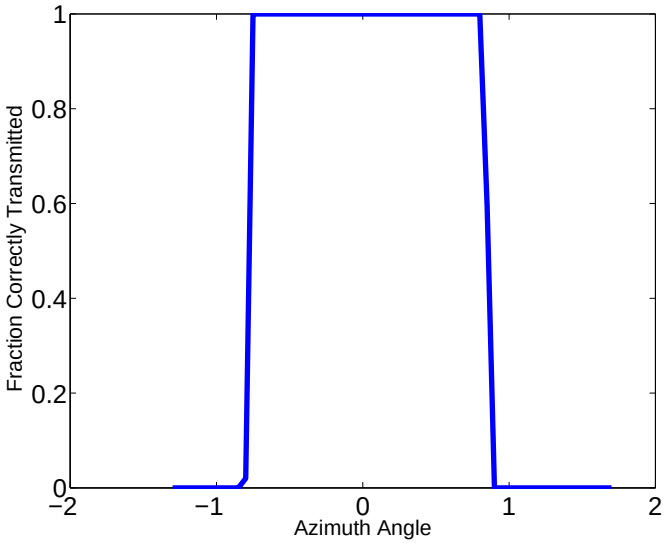

Figure 5.13: The system's sensitivity to alignment at the transmitter. At approximately 68 meters in range between the transmitter and receiver, 10,000 serial packets were sent to the receiver. The figure plots the fraction of 10,000 packets received vs the transmitter alignment angle.

Chapter 6: Conclusions

In this work, we have explored how LED-based communication can be used in point-to-point links. This work is motivated by the potential of such links to serve as a means of communication between mobile platforms such as vehicles and robots. Technology in this application space has long been dominated by RF communication, but LED-based communication may serve as an attractive supplement due to its unrestricted access to a broad range of electromagnetic spectrum, the low cost and high efficiency of LEDs, and other advantages. Wireless communications that rely exclusively on optical means may be especially attractive in setting in which RF communication is prohibited or undesirable.

Perhaps the greatest challenge in implementing optical wireless communication between mobile nodes is the challenge in alignment. In this work, we define a link model to estimate achievable rates, and use the model to show that a single LED can be used to create a low-data-rate alignment-insensitive (beacon) link that could provide the alignment support needed for a higher-data-rate (primary) link. Once establishing the feasibility of such a beacon link, we define a design framework for the consideration of dual-link systems, composed of a primary link supported by a beacon link.

Expanding on motivation for optical beacon links which can be insensitive to the alignment, we propose and analyze the use a catadioptric system as a beacon receiver. The catadioptric system studied is composed of a hyperboloidal mirror and a camera, and is used to estimate the range and bearing of a beacon. In the context of optical wireless communication between mobile platforms, the catadioptric system may be co-located with a node (A), while the beacon (an LED) may be co-located with another node (B); the catadioptric system is used as a means for node A to estimate the range and bearing of node B. This may enable node A to point an LED transmitter and/or receiver towards node B, facilitating establishment of a wireless optical link. In our implementation, the LED flashes, helping to isolate the image of the LED in the images captured by the camera. This enables the localization of the pixels illuminated by the LED within the $x-y$ plane of the camera image; knowledge of the illuminated pixels in that plane correspond to azimuth and elevation angles according to the geometry of the catadioptric system, and thus estimates of the LED beacon's bearing can be made. We develop an analytical model for the consideration of Gaussian error in the the localization of the illuminated pixels in the camera image, deriving closed-form expressions for the corresponding error in estimation of azimuth and elevation.

This system is implemented as part of a prototype of a type of dual-link system, in which the angular estimates produced by the catadioptric system are used to control a gimbal and direct an LED transmitter towards a receiver co-located with a beacon.

From each of the sections of this thesis, there exist avenues for the expansion of

research. The dual-link system proposed may motivate further research that utilizes more than two cooperative optical links, each with its own sensitivity to alignment. Systems that include multiple cooperative links may further enhance the data rates and robustness of communication between mobile platforms. Studies of networks composed of these links may be well-motivated.

The catadioptric system has been studied as a means of alignment between mobile nodes. Given this application space, a study of the potential for miniaturization of the system and miniaturization's effect on the precision of the system are well-motivated by the footprint constraints on many mobile platforms. The image processing for beacon localization that was implemented in our study is kept relatively simple; robust beacon localization in dynamic, noisy environments will require more sophisticated techniques. Such algorithms may exploit high-speed cameras, high-speed processing of many frames, analysis of beacon shapes, analysis of the nature of noise due to motion, tracking of multiple beacons simultaneously, color differentiation of beacons, and many other potential aspects of study. In addition to catadioptric systems that utilize hyperboloidal mirrors, other related optical components, such as paraboloidal mirrors and fish-eye lenses, may also be of potential interest within the context of beacon localization.

Bibliography

[1] Toshihiko Komine and Masao Nakagawa. Fundamental analysis for visible-light communication system using led lights. *Consumer Electronics, IEEE Transactions on*, 50(1):100–107, 2004.

[2] Jelena Grubor, Sebastian Randel, Klaus-Dieter Langer, and Joachim W Walewski. Broadband information broadcasting using led-based interior lighting. *Journal of Lightwave technology*, 26(24):3883–3892, 2008.

[3] Dominic O'Brien, Gareth Parry, and Paul Stavrinou. Optical hotspots speed up wireless communication. *Nature Photonics*, 1(5):245–247, 2007.

[4] Hany Elgala, Raed Mesleh, and Harald Haas. Indoor optical wireless communication: potential and state-of-the-art. *Communications Magazine, IEEE*, 49(9):56–62, 2011.

[5] DC OBrien. Optical wireless communications and potential applications in space. In *Proc. International Conference on Space Optical Systems and Applications, France*, 2012.

[6] SB Park, DK Jung, HS Shin, DJ Shin, YJ Hyun, K Lee, and YJ Oh. Information broadcasting system based on visible light signboard. *Proceedings of the Wireless and Optical Communications, Montreal, QC, Canada*, 30, 2007.

[7] K-D Langer and Jelena Grubor. Recent developments in optical wireless communications using infrared and visible light. In *Transparent Optical Networks, 2007. ICTON'07. 9th International Conference on*, volume 3, pages 146–151. IEEE, 2007.

[8] Mustafa Uysal and Hatef Nouri. Optical wireless communicationsan emerging technology. In *Transparent Optical Networks (ICTON), 2014 16th International Conference on*, pages 1–7. IEEE, 2014.

[9] Shun-Hsiang Yu, Oliver Shih, Hsin-Mu Tsai, Nawaporn Wisitpongphan, and Richard Roberts. Smart automotive lighting for vehicle safety. *Communications Magazine, IEEE*, 51(12):50–59, 2013.

[10] Navin Kumar, Domingos Terra, Nuno Lourenço, Luis Nero Alves, and Rui L Aguiar. Visible light communication for intelligent transportation in road safety applications. In *Wireless Communications and Mobile Computing Conference (IWCMC), 2011 7th International*, pages 1513–1518. IEEE, 2011.

[11] Kaiyun Cui, Gang Chen, Zhengyuan Xu, and Richard D Roberts. Traffic light to vehicle visible light communication channel characterization. *Applied optics*, 51(27):6594–6605, 2012.

[12] Ian C Rust and H Harry Asada. A dual-use visible light approach to integrated communication and localization of underwater robots with application to non-destructive nuclear reactor inspection. In *Robotics and Automation (ICRA), 2012 IEEE International Conference on*, pages 2445–2450. IEEE, 2012.

[13] Marek Doniec, Carrick Detweiler, Iuliu Vasilescu, and Daniela Rus. Using optical communication for remote underwater robot operation. In *Intelligent Robots and Systems (IROS), 2010 IEEE/RSJ International Conference on*, pages 4017–4022. IEEE, 2010.

[14] Joseph M Kahn and John R Barry. Wireless infrared communications. *Proceedings of the IEEE*, 85(2):265–298, 1997.

[15] David JT Heatley, David R Wisely, Ian Neild, and Peter Cochrane. Optical wireless: The story so far. *Communications Magazine, IEEE*, 36(12):72–74, 1998.

[16] Deva K Borah, Anthony C Boucouvalas, Christopher C Davis, Steve Hranilovic, and Konstantinos Yiannopoulos. A review of communication-oriented optical wireless systems. *EURASIP Journal on Wireless Communications and Networking*, 2012(1):1–28, 2012.

[17] Mike Wolf and Dieter Kreß. Short-range wireless infrared transmission: the link budget compared to rf. *IEEE wireless communications*, 10(2):8–14, 2003.

[18] Raymond M Sova, Joseph E Sluz, David W Young, Juan C Juarez, Anurag Dwivedi, Nickolas M Demidovich III, JE Graves, Malcolm Northcott, Jeff Douglass, John Phillips, et al. 80 gb/s free-space optical communication demonstration between an aerostat and a ground terminal. In *SPIE Optics+ Photonics*, pages 630414–630414. International Society for Optics and Photonics, 2006.

[19] Juan C Juarez, Anurag Dwivedi, Steven D Jones, Vijitha Weerackody, Robert Nichols, et al. Free-space optical communications for next-generation military networks. *Communications Magazine, IEEE*, 44(11):46–51, 2006.

[20] Ashwin Ashok, Marco Gruteser, Narayan Mandayam, Jayant Silva, Michael Varga, and Kristin Dana. Challenge: Mobile optical networks through visual mimo. In *Proceedings of the sixteenth annual international conference on Mobile computing and networking*, pages 105–112. ACM, 2010.

[21] Satoshi Hagihira, Masaki Takashina, Takahiko Mori, Nobuyuki Taenaka, Takashi Mashimo, and Ikuto Yoshiya. Infrared transmission of electronic information via lan in the operating room. *Journal of clinical monitoring and computing*, 16(3):171–175, 2000.

[22] S Sheikh Muhammad, T Plank, Erich Leitgeb, A Friedl, K Zettl, Tomaž Javornik, and N Schmitt. Challenges in establishing free space optical communications between flying vehicles. In *Communication Systems, Networks and Digital Signal Processing, 2008. CNSDSP 2008. 6th International Symposium on*, pages 82–86. IEEE, 2008.

[23] Hennes Henniger and Otakar Wilfert. An introduction to free-space optical communications. *Radioengineering*, 19(2):203–212, 2010.

[24] Santanu Das, Hennes Henniger, Bernhard Epple, Christopher I Moore, William Rabinovich, Raymond Sova, and David Young. Requirements and challenges for tactical free-space lasercomm. In *Military Communications Conference, 2008. MILCOM 2008. IEEE*, pages 1–10. IEEE, 2008.

[25] Fritz R Gfeller and Urs Bapst. Wireless in-house data communication via diffuse infrared radiation. *Proceedings of the IEEE*, 67(11):1474–1486, 1979.

[26] Siddha Pimputkar, James S Speck, Steven P DenBaars, and Shuji Nakamura. Prospects for led lighting. *Nature Photonics*, 3(4):180–182, 2009.

[27] Dominic O'Brien and Marcos Katz. Optical wireless communications within fourth-generation wireless systems [invited]. *Journal of optical networking*, 4(6):312–322, 2005.

[28] Tarik Borogovac, Michael Rahaim, and Jeffrey B Carruthers. Spotlighting for visible light communications and illumination. In *GLOBECOM Workshops (GC Wkshps), 2010 IEEE*, pages 1077–1081. IEEE, 2010.

[29] Volker Jungnickel, Andreas Forck, Thomas Haustein, Udo Krüger, Volker Pohl, and Clemens Von Helmolt. Electronic tracking for wireless infrared communications. *Wireless Communications, IEEE Transactions on*, 2(5):989–999, 2003.

[30] J-W Shi, J-K Sheu, C-H Chen, G-R Lin, and W-C Lai. High-speed gan-based green light-emitting diodes with partially n-doped active layers and current-confined apertures. *Electron Device Letters, IEEE*, 29(2):158–160, 2008.

[31] Jonathan JD McKendry, Richard P Green, AE Kelly, Zheng Gong, Benoit Guilhabert, David Massoubre, Erdan Gu, and Martin D Dawson. High-speed visible light communications using individual pixels in a micro light-emitting diode array. *Photonics Technology Letters, IEEE*, 22(18):1346–1348, 2010.

[32] AE Kelly, JJD McKendry, S Zhang, D Massoubre, BR Rae, RP Green, RK Henderson, and MD Dawson. High-speed gan micro-led arrays for data communications. In *Transparent Optical Networks (ICTON), 2012 14th International Conference on*, pages 1–5. IEEE, 2012.

[33] Shuailong Zhang, Scott Watson, Jonathan JD McKendry, David Massoubre, Andrew Cogman, Erdan Gu, Robert K Henderson, Anthony E Kelly, and Martin D Dawson. 1.5 gbit/s multi-channel visible light communications using cmos-controlled gan-based leds. *Journal of Lightwave Technology*, 31(8):1211–1216, 2013.

[34] Dominic C O'Brien, Lang Zeng, Hoa Le-Minh, Grahame Faulkner, Joachim W Walewski, and Sebastian Randel. Visible light communications: Challenges and possibilities. In *Personal, Indoor and Mobile Radio Communications, 2008. PIMRC 2008. IEEE 19th International Symposium on*, pages 1–5. IEEE, 2008.

[35] Hoa Le Minh, Dominic O'Brien, Grahame Faulkner, Lubin Zeng, Kyungwoo Lee, Daekwang Jung, YunJe Oh, and Eun Tae Won. 100-mb/s nrz visible light communications using a postequalized white led. *Photonics Technology Letters, IEEE*, 21(15):1063–1065, 2009.

[36] Hoa Le Minh, Dominic O'Brien, Grahame Faulkner, Lubin Zeng, Kyungwoo Lee, Daekwang Jung, and YunJe Oh. 80 mbit/s visible light communications using pre-equalized white led. In *2008 34th European Conference on Optical Communication*, 2008.

[37] Jiun-Yu Sung, Chi-Wai Chow, and Chien-Hung Yeh. Is blue optical filter necessary in high speed phosphor-based white light led visible light communications? *Optics express*, 22(17):20646–20651, 2014.

[38] Honglei Li, Xiongbin Chen, Junqing Guo, and Hongda Chen. A 550 mbit/s real-time visible light communication system based on phosphorescent white light led for practical high-speed low-complexity application. *Optics express*, 22(22):27203–27213, 2014.

[39] Xingxing Huang, Zhixin Wang, Jianyang Shi, Yiguang Wang, and Nan Chi. 1.6 gbit/s phosphorescent white led based vlc transmission using a cascaded pre-equalization circuit and a differential outputs pin receiver. *Optics express*, 23(17):22034–22042, 2015.

[40] Jelena Grubor, Sian Chong Jeffrey Lee, Klaus-Dieter Langer, Ton Koonen, and Joachim W Walewski. Wireless high-speed data transmission with phosphorescent white-light leds. *ECOC 2007*, 2007.

[41] Hoa Le Minh, Dominic O'Brien, Grahame Faulkner, Lubin Zeng, Kyungwoo Lee, Daekwang Jung, and YunJe Oh. High-speed visible light communications

using multiple-resonant equalization. *Photonics Technology Letters, IEEE*, 20(14):1243–1245, 2008.

[42] Honglei Li, Xiongbin Chen, Beiju Huang, Danying Tang, and Hongda Chen. High bandwidth visible light communications based on a post-equalization circuit. *Photonics Technology Letters, IEEE*, 26(2):119–122, 2014.

[43] AM Khalid, G Cossu, R Corsini, P Choudhury, and E Ciaramella. 1-gb/s transmission over a phosphorescent white led by using rate-adaptive discrete multitone modulation. *Photonics Journal, IEEE*, 4(5):1465–1473, 2012.

[44] Jelena Vučić, Christoph Kottke, Stefan Nerreter, Klaus-Dieter Langer, and Joachim W Walewski. 513 mbit/s visible light communications link based on dmt-modulation of a white led. *Journal of Lightwave Technology*, 28(24):3512–3518, 2010.

[45] Hany Elgala, Raed Mesleh, Harald Haas, and Bogdan Pricope. Ofdm visible light wireless communication based on white leds. In *Vehicular Technology Conference, 2007. VTC2007-Spring. IEEE 65th*, pages 2185–2189. IEEE, 2007.

[46] Ozgur Ergul, Ergin Dinc, and Ozgur B Akan. Communicate to illuminate: State-of-the-art and research challenges for visible light communications. *Physical Communication*, 2015.

[47] Mehmet Bilgi and Murat Yuksel. Multi-element free-space-optical spherical structures with intermittent connectivity patterns. In *INFOCOM Workshops 2008, IEEE*, pages 1–4. IEEE, 2008.

[48] Larry B Stotts, Larry C Andrews, Paul C Cherry, James J Foshee, Paul J Kolodzy, William K McIntire, Malcolm Northcott, Ronald L Phillips, H Alan Pike, Brian Stadler, et al. Hybrid optical rf airborne communications. *Proceedings of the IEEE*, 97(6):1109–1127, 2009.

[49] Vladimir V Nikulin and Rahul Khandekar. Performance of laser communication uplinks and downlinks in the presence of pointing errors and atmospheric distortions. In *Lasers and Applications in Science and Engineering*, pages 37–45. International Society for Optics and Photonics, 2005.

[50] Bernhard Epple. Using a gps-aided inertial system for coarse-pointing of free-space optical communication terminals. In *SPIE Optics+ Photonics*, pages 630418–630418. International Society for Optics and Photonics, 2006.

[51] John Rzasa, Stuart D Milner, and Christopher C Davis. Design and implementation of pan-tilt fso transceiver gimbals for real-time compensation of platform disturbances using a secondary control network. In *SPIE Optical Engineering+ Applications*, pages 81620E–81620E. International Society for Optics and Photonics, 2011.

[52] Stuart D Milner and Christopher C Davis. Hybrid free space optical/rf networks for tactical operations. In *Military Communications Conference, 2004. MILCOM 2004. 2004 IEEE*, volume 1, pages 409–415. IEEE, 2004.

[53] Hossein Izadpanah, Tamer Elbatt, Vikas Kukshya, Frank Dolezal, and Bo K Ryu. High-availability free space optical and rf hybrid wireless networks. *Wireless Communications, IEEE*, 10(2):45–53, 2003.

[54] Yi Tang and Maite Brandt-Pearce. Link allocation, routing and scheduling of fso augmented rf wireless mesh networks. In *Communications (ICC), 2012 IEEE International Conference on*, pages 3139–3143. IEEE, 2012.

[55] Imran Shafique Ansari, M-S Alouini, and Ferkan Yilmaz. On the performance of hybrid rf and rf/fso fixed gain dual-hop transmission systems. In *Electronics, Communications and Photonics Conference (SIECPC), 2013 Saudi International*, pages 1–6. IEEE, 2013.

[56] Helal Chowdhury and Marcos Katz. Data download on move in indoor hybrid (radio-optical) wlan-vlc hotspot coverages. In *Vehicular Technology Conference (VTC Spring), 2013 IEEE 77th*, pages 1–5. IEEE, 2013.

[57] Wenzhe Zhang, Steve Hranilovic, and Ce Shi. Soft-switching hybrid fso/rf links using short-length raptor codes: design and implementation. *Selected Areas in Communications, IEEE Journal on*, 27(9):1698–1708, 2009.

[58] Mehmet Bilgi, Murat Yuksel, and Nezih Pala. 3-d optical wireless localization. In *GLOBECOM Workshops (GC Wkshps), 2010 IEEE*, pages 1062–1066. IEEE, 2010.

[59] Murat Yuksel, Jayasri Akella, Shivkumar Kalyanaraman, and Partha Dutta. Free-space-optical mobile ad hoc networks: Auto-configurable building blocks. *Wireless Networks*, 15(3):295–312, 2009.

[60] Karen B Sarachik. Characterising an indoor environment with a mobile robot and uncalibrated stereo. In *Robotics and Automation, 1989. Proceedings., 1989 IEEE International Conference on*, pages 984–989. IEEE, 1989.

[61] Hiroshi Ishiguro, Masashi Yamamoto, and Saburo Tsuji. Omni-directional stereo for making global map. In *Computer Vision, 1990. Proceedings, Third International Conference on*, pages 540–547. IEEE, 1990.

[62] Thomas C Shen, Robert J Drost, Christopher C Davis, and Brian M Sadler. Design of dual-link (wide-and narrow-beam) led communication systems. *Optics express*, 22(9):11107–11118, 2014.

[63] Roberto Ramirez-Iniguez, Sevia M Idrus, and Ziran Sun. *Optical wireless communications: IR for wireless connectivity*. CRC press, 2008.

[64] Xiaohui Ning, Roland Winston, Joseph OGallagher, et al. Dielectric totally internally reflecting concentrators. *Applied Optics*, 26(2):300–305, 1987.

[65] C Chow, C Yeh, Y Liu, and P Huang. Mitigation of optical background noise in light-emitting diode (led) optical wireless communication systems. 2013.

[66] Adriano JC Moreira, Rui T Valadas, and AM de Oliveira Duarte. Optical interference produced by artificial light. *Wireless Networks*, 3(2):131–140, 1997.

[67] John R Barry. *Wireless infrared communications*, volume 280. Springer, 1994.

[68] Joseph M Kahn, John R Barry, Malik D Audeh, Jeffrey B Carruthers, William J Krause, and Gene W Marsh. Non-directed infrared links for high-capacity wireless lans. *Personal Communications, IEEE*, 1(2):12, 1994.

[69] Dominic C OBrien, Marcos Katz, P Wang, K Kalliojarvi, S Arnon, M Matsumoto, RJ Green, and S Jivkova. Short-range optical wireless communications. In *Wireless world research forum*, pages 1–22, 2005.

[70] Thorlabs. `http://www.thorlabs.com`. Accessed: 2015-11-08.

[71] Keang-Po Ho and Joseph M Kahn. Compound parabolic concentrators for narrowband wireless infrared receivers. *Optical Engineering*, 34(5):1385–1395, 1995.

[72] Edmundoptics. `http://www.edmundoptics.com`. Accessed: 2015-11-08.

[73] John Rzasa, Mehmet Can Ertem, and Christopher C Davis. Pointing, acquisition, and tracking considerations for mobile directional wireless communications systems. In *SPIE Optical Engineering+ Applications*, pages 88740C–88740C. International Society for Optics and Photonics, 2013.

[74] Hobby King. `http://www.http://www.hobbyking.com/.com`. Accessed: 2016-05-29.

[75] Kazumasa Yamazawa, Yasushi Yagi, and Masahiko Yachida. Omnidirectional imaging with hyperboloidal projection. In *Intelligent Robots and Systems' 93, IROS'93. Proceedings of the 1993 IEEE/RSJ International Conference on*, volume 2, pages 1029–1034. IEEE, 1993.

[76] Thomas C Shen, Robert J Drost, John Rzasa, Brian M Sadler, and Christopher C Davis. Panoramic alignment system for optical wireless communication systems. In *SPIE LASE*, pages 93540M–93540M. International Society for Optics and Photonics, 2015.

[77] Tzung-Hsien Ho, Stuart D Milner, and Christopher C Davis. Fully optical real-time pointing, acquisition, and tracking system for free space optical link. In *Lasers and Applications in Science and Engineering*, pages 81–92. International Society for Optics and Photonics, 2005.

[78] Seongsu Lee and Sung-Yoon Jung. Location awareness using angle-of-arrival based circular-pd-array for visible light communication. In *Communications (APCC), 2012 18th Asia-Pacific Conference on*, pages 480–485. IEEE, 2012.

[79] Dongfang Zheng, Kaiyun Cui, Bo Bai, Gang Chen, and Jay A Farrell. Indoor localization based on leds. In *Control Applications (CCA), 2011 IEEE International Conference on*, pages 573–578. IEEE, 2011.

[80] Simon Baker and Shree K Nayar. A theory of single-viewpoint catadioptric image formation. *International Journal of Computer Vision*, 35(2):175–196, 1999.

[81] Mark Fiala and Anup Basu. Robot navigation using panoramic tracking. *Pattern Recognition*, 37(11):2195–2215, 2004.

[82] Yasushi Yagi, Watam Nishii, Kazumasa Yamazawa, and Masahiko Yachida. Rolling motion estimation for mobile robot by using omnidirectional image sensor hyperomnivision. In *Pattern Recognition, 1996., Proceedings of the 13th International Conference on*, volume 1, pages 946–950. IEEE, 1996.

[83] Jongcheol Kim and Yasuo Suga. An omnidirectional vision-based moving obstacle detection in mobile robot. *International Journal of Control Automation and Systems*, 5(6):663, 2007.

[84] Larry Matthies and Steven A Shafer. Error modeling in stereo navigation. *Robotics and Automation, IEEE Journal of*, 3(3):239–248, 1987.

[85] Robb J Muirhead. *Aspects of multivariate statistical theory*, volume 197. John Wiley & Sons, 2009.

[86] David V Hinkley. On the ratio of two correlated normal random variables. *Biometrika*, 56(3):635–639, 1969.

[87] Prathapasinghe Dharmawansa, Nandana Rajatheva, and Chinthananda Tellambura. Envelope and phase distribution of two correlated gaussian variables. *Communications, IEEE Transactions on*, 57(4):915–921, 2009.

[88] Neovision. `http://www.neovision.cz/prods/panoramic/h3s.html`. Accessed: 2014-10-15.

[89] Allied Vision Technologies. `http://www.alliedvisiontec.com/`. Accessed: 2014-10-15.

[90] LEDsupply. `http://www.ledsupply.com`. Accessed: 2014-10-15.

[91] Yi-Yuan Chen, Kuen-Ming Lan, Hung-I Pai, Jen-Hui Chuang, and Chii-Yah Yuan. Robust light objects recognition based on computer vision. In *Pervasive Systems, Algorithms, and Networks (ISPAN), 2009 10th International Symposium on*, pages 508–514. IEEE, 2009.

[92] Grantham KH Pang and Hugh HS Liu. Led location beacon system based on processing of digital images. *Intelligent Transportation Systems, IEEE Transactions on*, 2(3):135–150, 2001.

[93] Dongfang Zheng, Gang Chen, and Jay A Farrell. Navigation using linear photo detector arrays. In *Control Applications (CCA), 2013 IEEE International Conference on*, pages 533–538. IEEE, 2013.

[94] Mark P Wernet and A Pline. Particle displacement tracking technique and cramer-rao lower bound error in centroid estimates from ccd imagery. *Experiments in Fluids*, 15(4-5):295–307, 1993.

[95] Norman Bobroff. Position measurement with a resolution and noise-limited instrument. *Review of Scientific Instruments*, 57(6):1152–1157, 1986.

[96] Jeffrey S Morgan, DC Slater, John G Timothy, and EB Jenkins. Centroid position measurements and subpixel sensitivity variations with the mama detector. *Applied optics*, 28(6):1178–1192, 1989.

[97] Richard H Stanton, James W Alexander, Edwin W Dennison, Thomas A Glavich, and Larry F Hovland. Optical tracking using charge-coupled devices. *Optical Engineering*, 26(9):269930–269930, 1987.

[98] Brian F Alexander and Kim Chew Ng. Elimination of systematic error in subpixel accuracy centroid estimation [also letter 34 (11) 3347-3348 (nov1995)]. *Optical Engineering*, 30(9):1320–1331, 1991.

[99] Shinhak Lee. Pointing accuracy improvement using model-based noise reduction method. In *High-Power Lasers and Applications*, pages 65–71. International Society for Optics and Photonics, 2002.

[100] Joyce Farrell, Feng Xiao, and Sam Kavusi. Resolution and light sensitivity tradeoff with pixel size. In *Electronic Imaging 2006*, pages 60690N–60690N. International Society for Optics and Photonics, 2006.

[101] Labview. `http://zone.ni.com/reference/en-XX/help/370281P-01/imaqvision/imaq_fi` Accessed: 2016-03-18.

[102] LEDsupply Rebel. `http://www.ledsupply.com/leds/luxeon-rebel-color-leds`. Accessed: 2016-03-26.

[103] Maxim. `https://www.maximintegrated.com/en/products/interface/transceivers/MAX` Accessed: 2016-03-26.